Title
Simulation on Rational Design for High-Performance Electrochemical Energy Storage

Author
Xu, Pengcheng

Publication Date
2020

Peer reviewed|Thesis/dissertation

UNIVERSITY OF CALIFORNIA

Los Angeles

Simulation on Rational Design for High-Performance Electrochemical Energy Storage

A dissertation submitted in partial satisfaction of the requirements for the degree Doctor of Philosophy in Chemical Engineering

by

Pengcheng Xu

2020

ABSTRACT OF THE DISSERTATION

Simulation on Rational Design

for High-Performance Electrochemical Energy Storage

by

Pengcheng Xu

Doctor of Philosophy in Chemical Engineering

University of California, Los Angeles, 2020

Professor Yunfeng Lu, Chair

Professor Lihua Jin, Co-Chair

As an essential element of sustainable energy technologies, electrochemical energy storage makes a significant contribution to the development of many industry fields such as consumer electronics and electric vehicles. Meanwhile, the complicated and evolving application markets raise new challenges to electrochemical energy storage systems in all-rounded performance matrices including energy density, operating conditions, durability and so on. There is a great amount of relevant research in various scales and directions, e.g., material development, electrochemical analysis and reliability testing. Modeling and simulation, together with rational material/system design, explores the internal processes for performance matrices of electrochemical systems, characterizes key improvement achieved by the implementation of

design, and predicts future values/tendencies of significant variables based on learned patterns for system monitoring. This dissertation could be outlined with the following three parts:

1. Explaining transient responses of proton exchange membrane fuel cells (with tungsten oxide addition to anode). An equivalent circuit model is employed to characterize dynamic responses of PEMFCs under transient operations and the improved power performance achieved by a system design of integrating a WO_3 layer with anodes. To explain what is going on within the fuel cell system and the contribution of the system design, a mathematical model simulating gas transport within the gas diffusion layer attributes voltage undershoot under transient operations to unbalance between the demand of gas at the catalyst layer and the supply at gas flow channel (through the gas diffusion layer). Moreover, it is also observed that the addition of WO_3 layers increases the capacity of the double layer, buffers the change of reaction current density, mitigates the transient gas demand-supply unbalance, and thus improves power performance under transient operations.

2. Explaining rate/cycling performances of lithium-ion batteries (with metal-organic frameworks addition to electrolyte). Lithium ion transference number plays an important role in research on high-rate/cycling performances of lithium-ion batteries. Firstly, to show how lithium ion transference number might be improved via rational design of MOF additions, heterogeneous geometries (pattern/density/location) to the separator/electrolytes are discussed. Secondly, to explore how lithium ion transference number affects rate performances of lithium ion batteries, a mathematical model is studied for half-cells to indicate the links among lithium ion transference number, electrolyte salt concentration gradient, concentration polarization and utilizable capacity. Thirdly, to explore how lithium ion transference number affects cycling performances of lithium ion batteries, mechanisms of solid-electrolyte interphase layer formation is introduced

to the mathematical model for a full-cell, which discusses the overpotential of parasitic SEI reactions and loss of cyclable lithium under stable and dynamic cycling tests.

3. Predicting the remaining useful lives of lithium-ion batteries under cycling charge/discharge operations. Efficient and accurate remaining useful life prediction is a key factor for reliable and safe usage of lithium-ion batteries. A long short-term memory recurrent neural network model, by extracting features of discharge capacity variation under specific voltages due to capacity degradation, is trained to learn from sequential data of discharge capacities at various cycles and voltages and to work as a cycle life predictor for battery cells cycled under different operating conditions. Using experimental data of first 60 - 80 cycles, the model can achieve promising prediction accuracy on test sets of about 80 samples.

Overall, this dissertation applies models for proton exchange membrane fuel cell and lithium-ion battery with different techniques to simulate internal processes occurring in a component/the entire system, and explains the reason why adopted design strategies mitigate certain types of performance bottlenecks or utilizes big data to learning from time series and make predictions on remaining useful lives. With these works, some inspirations might be provided for understanding methods to enhance transient and/or high-rate performances of electrochemical energy storage systems.

The dissertation of Pengcheng Xu is approved.

Vasilios Manousiouthakis

Yoram Cohen

Lihua Jin, Committee Co-Chair

Yunfeng Lu, Committee Chair

University of California, Los Angeles

2020

TO MY FAMILY

Table of Contents

LIST OF FIGURES

LIST OF TABLES

ACKNOWLEDGEMENTS

Of this five-year journey to purse a doctoral degree, I am greatly indebted to many people for their kind help and supports.

Firstly, I would like to express my sincere appreciation to my advisor, Professor Yunfeng Lu. Without his instruction and encouragement, it would not be possible for me to finish this dissertation. I have learnt a lot from his supervision, from the way to think about research projects to the way to communicate with people. It usually works to start from building blocks within a big picture, deal with complicated scenarios in later stages and leave alone tedious issues. It is significant to learn and develop tools for the requirements of research projects, while it is even more significant to search for physical meanings from abstract results instead of getting lost in endless optimization of models. In terms of communication with people, the lesson I learn from Professor Lu is how to effectively deliver understandable information to people. It is always difficult for me to communicate with people, as I do not understand efficient methods to motivate and persuade people. From contacts with Professor Lu, I gradually realize that working together with practical communication means is achievable and productive, which reduces unnecessary costs and enhance collective outputs. Thanks to Professor Lu's guidance, it could be viewed as a treasure for lifetime from career development to life philosophy.

I would like to express my deep gratitude to my co-advisor, Professor Lihua Jin. Professor Jin is very patient and kind. I still remember she taught me how to find and read literature fast and comprehensively at the very beginning. She inspired me to focus on what's going on behind a concept, a problem and a solution, which provides insights for further explorations. She is also open-minded and encourages me to combine dry lab simulations with wet lab experiments. In

this way, it is promising to obtain not only intuitive understanding but also theoretical explanations, helping the formation of well-rounded system of knowledge. Many thanks for Professor Jin's instruction on how to think and work with an all-rounded approach for profound outcome.

I would like to thank my doctoral committee members, Professor Vasilios Manousiouthakis and Professor Yoram Cohen. I have taken the course of Mass Transfer with Professor Cohen and the course of Engineering Mathematics with Professor Manousiouthakis. Much fundamental knowledge helped establishing and analyzing models in this dissertation. Furthermore, their strict training made me realize the importance of a systematic way to explore an academic problem: stating the question clearly and unambiguously, proposing reasonable assumptions, comparing different practical approaches, looking for solutions economically and efficiently and drawing conclusions as soundly and completely as possible. This training greatly helps shaping the habits of critical training. I sincerely appreciate it.

I would like to thank Dr Zaiyuan Le. He is one of the most warm-hearted and considerate people I have ever met. He is always kind to people around him and willing to offer helps to them. He not only teaches me many laboratory techniques but also shares many lifetime thoughts with me. Without his kind support, I would not be able to survive these struggling years.

I would like to thank Dr Gen Chen. He helped me a lot in both study and life. In addition to his excellent laboratory techniques and professional writing, I appreciate his optimistic attitude to uneasiness in life. When unhappiness occurs, do not let it border you, but try to bypass or overcome it, then you will ultimately find the inner peace.

I would like to thank Dr Li Shen. He offered warm encouragements to me when I faced difficulties with research. I enjoy and learn a lot from discussions with him. He is careful in

model assumptions and stresses the physical meaning of simulation results, which also influences me to pay attentions to the linkages between real systems and simulation models.

I would like to thank Dr Xinru Li. Her painstaking attitude to overcome tough fundamental courses and exams impresses me a lot. In addition, like an artist, she has a good taste on photography and cooking. I am inspired by her to discover and feel the touch and beautifulness and in daily lives.

I would like to thank Dr Haobin Wu, Dr Jing Liu, Dr Lu Zhang, Dr Haiping Wu, Dr Di Wu, Dr Jie Ren, Dr Gurong Shen, Dr Xianyang Li, Dr Zhuang Liu, Dr Xing Lu, Dr Ran Tao, Dr Yuzhen Chen. Many thanks for your instruction and inspirations. It is wonderful experience to discuss with you, which not only pave the way to explore research projects, but also nourish mind framework for thinking about open-ended problems. Also, it is great to take physical exercises together. Hiking, weighting, running and badminton are all enjoyable programs.

I would like to thank my lab-mates Dr Chen Zhang, Dr Wenyue Shi, Dr Dejia Kong, Dr Shengxiang Ma, Dr Fan Li, Dr Jesse Baucom, Dr Yuzhen Chen, Weiguo Chen, Jinhui Xu, Bowen An, Qingyang Yin, Masato Koizumi and Alexis Fortini. I still remember the first time when met in the new student welcome seminar and we took courses and worked on projects together. How time flies! Many thanks for your time and support. Wish we have become better ourselves.

I would like to thank my friends, Yue Li, Haiyue Li, Zheying Huang, Yan Cao, Dr Yiwen Meng, Dr Xue Xu, Dr Pei Zhou, Dr Bin Li, Dr Xu Wang, Dr Yaping Wang, Andrew Lin, Rosa Chang, Dr Peter Ma, Steven Nie, Patrica Xiao, Yewen Wang, Song Jiang, Otto Chang, Guanqun Yang, Haiqi Xiao and Yuqing Wang. It is a fortune to work/study/live together with you. There are tons of moments to remember. Wish you all the best in the future.

Mom and dad, thanks for your unconditional and consistent support. I know I am always not a child who never makes parents worried. I am sorry for the pains during all these years. I believe I will grow up ultimately. And we will ultimately find a way to achieve a balance between all of us. I love you. Wish you happiness and healthiness.

VITA

2012 – 2016 B.E.

School of Aeronautic Science and Engineering

Beihang University, China

2016 – 2020 Graduate Student Researcher, PhD

Department of Chemical and Biomolecular Engineering

University of California, Los Angeles, USA

Chapter 1 Background and Introduction

1.1 Motivation of Electrochemical Energy Storage

In the development of civilization, harvest and utilization of energies is one of the major topics. Since the second industry revolution, electricity has become the most significant source of energy of human society. Fossil fuels, as a major category of electricity generation, faces problems such as limited resources and harmfulness to the environment. [1] Thus, people are searching for renewable and eco-friendly alternatives. According to statistics, about 17% of generated electricity supply came from renewable sources such as hydropower and wind in the US in 2019. [2]

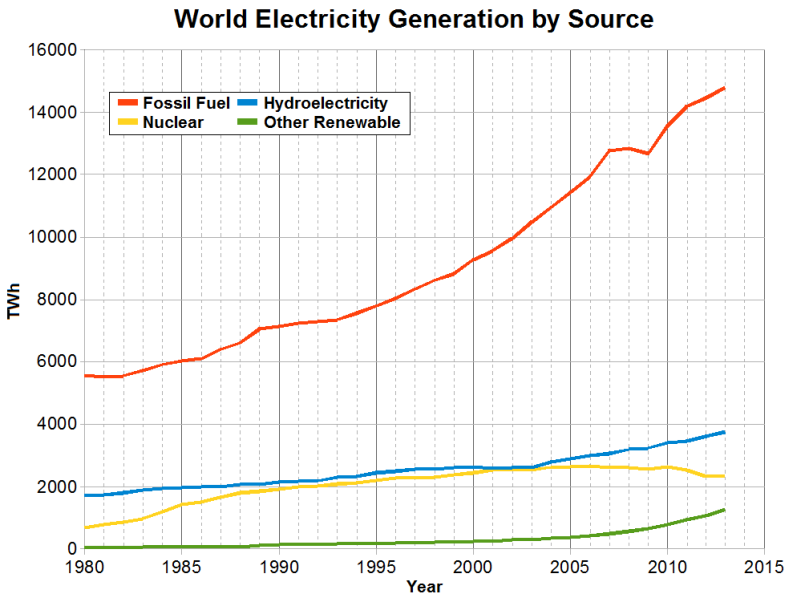

Figure 1-1 Electricity generation by source in the world. [3]

To help resolve the challenge for sustainable development, electrochemical energy storage systems can be a promising candidate. In recent decades, electrochemical energy storage systems

have attracted more and more interest in research and applications. [4] They are widely used in consumer electronics, electric vehicles and powerplant industries due to their advantages in availability and efficiency in addition to sustainability. However, electrochemical devices with high power and energy density and longevity is still a big challenge.

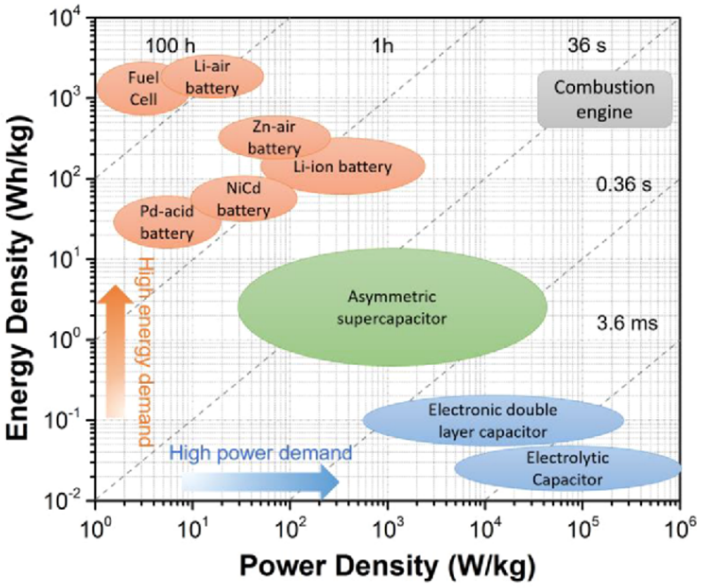

Figure 1-2 Ragone plot comparing the performance of different electrochemical energy storage systems. [4]

Electrochemical energy storage systems have been widely applied or considered as promising candidates for many fields of modern industry.

For example, lithium-ion batteries are widely used in consumer electronics [5], power tools [6] and electric vehicles [7]. Fuel cells have applications in portable power systems [8] and electric vehicles [9]. Supercapacitors are used in grid power buffer [10] and voltage stabilizer [11].

Many efforts have been made to address or mitigate challenges raised in industrial applications such as high power density, smooth transient response and enhanced cycling longevity and safety under complicated operations [12]. One typical strategy is to design the energy storage system with novel materials and structures. There are promising progresses [13][14] in this direction.

Another significant approach is to design and apply more intelligent management systems [15] for regulation and monitoring. Modeling simulation [16] could help people characterize significant performances, unveil the internal mechanisms of performance improvements and thus predict optimizations for device design and operation. Both experimental [17][18][19] and model-based [20][21][22] methods produce practical estimators for state of charge/state of health/remaining useful life of a system.

1.2 Overview of Electrochemical Energy Storage Systems

1.2.1 Rechargeable batteries

1.2.1.1 History and Applications

A rechargeable battery is a type of battery which can be recharged many times. Applications include portable consumer electronics, vehicle starters, small vehicles and battery storage power stations.

There are many typical types of rechargeable batteries: lead-acid batteries, nickel-cadmium batteries, nickel-iron batteries, lithium-ion batteries and lithium-ion polymer batteries. Also, experimental types include lithium-sulfur batteries, molten salt batteries and sodium-ion batteries Relevant research focuses on improving the lives and capacity of current systems and developing novel materials and systems.

1.2.1.2 Operation Principles

1.2.1.2.1 **Lead-acid batteries**

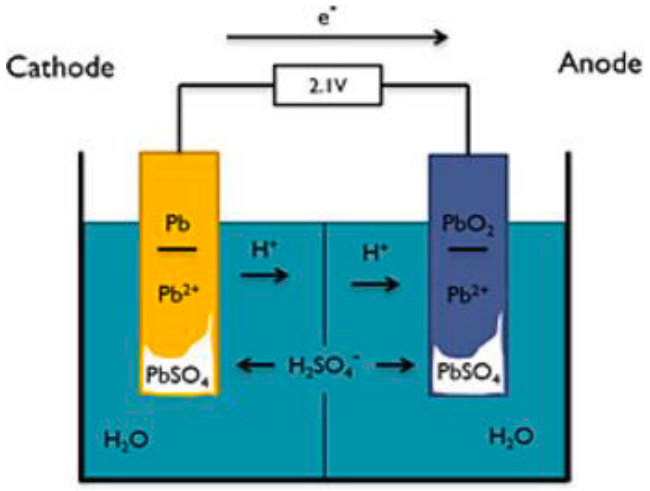

Figure 1-3 Scheme of a lead-acid battery. [28]

Lead-acid battery [23] is the oldest type of secondary battery (rechargeable battery). Despite of its low energy-to weight ratio and energy-to-weight ratio, it is widely used all around the world as backup power supplies and high-availability settings due to its low cost, capability to provide high current and thus relatively high power-to-weight ratio. The main applications of lead-acid batteries include vehicle start-up, lighting and ignition batteries.

It is usually constituted of plates (for electrodes), electrolyte solution, separator and absorbed glass mat (AGM). To form a stack, equal amounts of positive plates and negative plates are interleaved with insertion of separators. To form elements, the tabs of positive plates are welded together and that of negative plates are also welded together. After placed in the electric tank, the neighboring units are connected in *series* by welding the negative plate of one element and positive plate of the other.

In plates, the active material for electrochemical reaction is lead (Pb) at the negative plate (for anode) and lead dioxide (PbO_2) at the positive plate (for cathode). The plates are built up with

grids of lead alloys with high overpotential for hydrogen evolution reaction, which could inhibit the water electrolysis during charging processes.

The electrolyte solution is mainly dilute aqueous solution of sulfuric acid (H_2SO_4). It is worth mentioning that silica gelling agent are usually added into the electrolyte to from "gelled electrolyte", which could reduce water evaporation and withstand more extreme operation temperature.

The main use of separator is to prevent physical contact of positive plate and negative plate in a cell (short-circuit). However, it could increase the internal resistance (in the form of ohmic polarization). To be effective, separators are supposed to be of high ionic conductivity, high electronic resistance, high compatibility with electrolyte, stability under acid and so on. Commonly used separators include cellulose, polyethylene plastic and glass fiber mat.

The introduction of AGM could prevent the vertical movement of ions in the electrolyte solution, allow a compressed design of the battery by making electrolyte as a part of separator and so on.

Briefly speaking, the primary electrochemical reactions within a lead-acid battery is

Cathode reaction:

$$PbO_2(s) + HSO_4^-(aq) + 3H^+(aq) + 2e^- \rightarrow PbSO4(s) + 2H_2O(l)$$

anode reaction:

$$Pb(s) + HSO_4^-(aq) \rightarrow PbSO_4(s) + H^+(aq) + 2e^-$$

overall reaction:

$$Pb(s) + PbO_2(s) + 2H_2SO_4(aq) \rightarrow 2PbSO_4(s) + 2H_2O(l)$$

From Nernst equation, the thermodynamic potential (electromotive force, emf) of lead-acid battery is

$$E = E^0 + \frac{RT}{2F}\ln\left(\frac{a_{H_2SO_4}}{a_{H_2O}}\right)$$

For the cathode,

$$\varphi_{+} = \varphi_{+}^{0} + \frac{RT}{2F}\ln\left(\frac{a_{\mathrm{HSO_4^-}}a_{\mathrm{H^+}}^3}{a_{\mathrm{H_2O}}^2}\right)$$

For the anode,

$$\varphi_{-} = \varphi_{-}^{0} - \frac{RT}{2F}\ln\left(\frac{a_{\mathrm{HSO_4^-}}}{a_{\mathrm{H^+}}^3}\right)$$

1.2.1.2.2 **Lithium-ion batteries**

Lithium-ion batteries (LIBs) are among most popular secondary batteries in many fields including consumer electronics, power tools and electric vehicles. They have appealing advantages such as high energy density, high power density, fast charge/discharge, low self-discharge and no memory effects. However, their applications also suffer from disadvantages including unsustainability to deep charge/discharge, thermal runaway, fire hazard, need of multiple protection mechanisms.

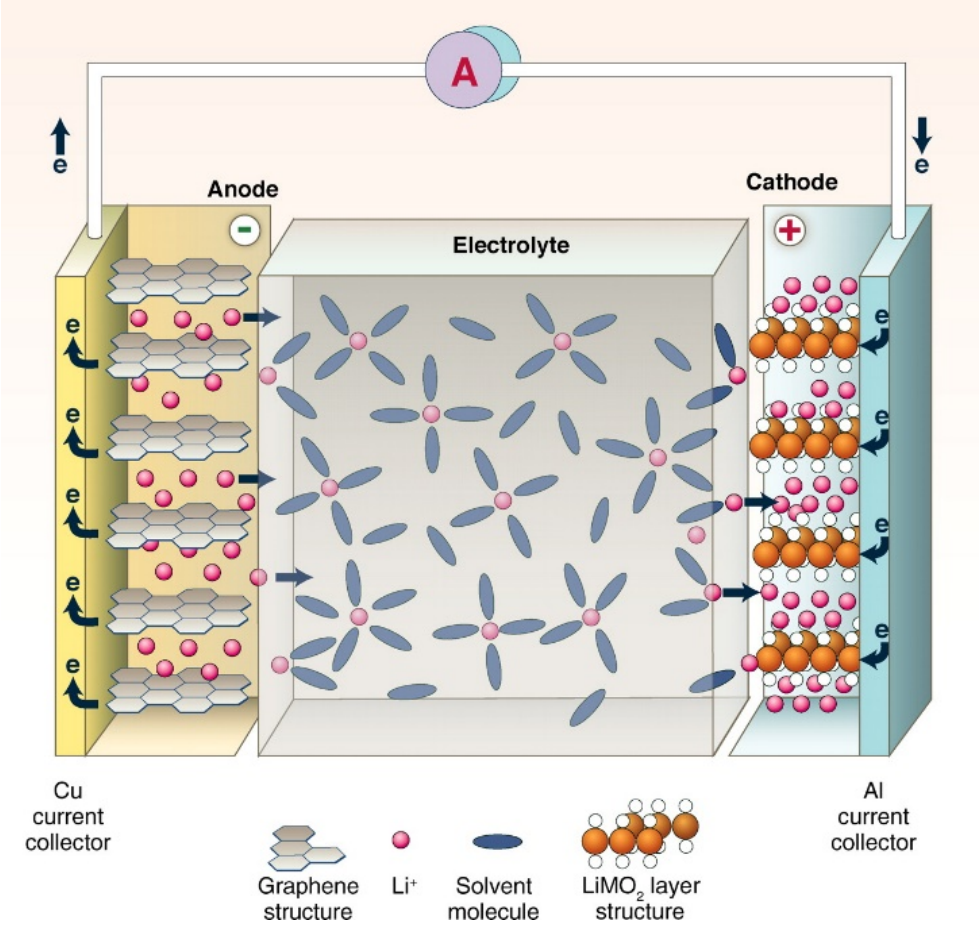

Figure 1-4 Scheme of a lithium-ion battery. [30]

A typical lithium-ion battery consists of two electrodes, separator, electrolyte and current collectors. During discharge processes, lithium ions move from the negative electrode to the positive electrode through an electrolyte; during charge processes, lithium ions move back to the negative electrode from the positive electrode.

Electrolytes, which serves as a pathway for transport of lithium ions between electrodes occurs, include liquid electrolytes and solid electrolytes. Liquid electrolytes in lithium-ion batteries consist of lithium salts (e.g., $LiPF_6$, $LiBF_4$) in an organic solvent (e.g., ethylene carbonate (EC), dimethyl carbonate (DMC)). Solid electrolytes, with no risk of leak, has become an interest of research in recent years. There are two main types of such electrolytes: ceramic and glassy.

Positive electrode (cathode) materials include cobalt-based material (built from $LiCoO_2$), manganese-based material (built from $LiMn_2O_4$), and lithium iron phosphate ($LiFePO_4$), out of considerations on capacity, safety, stability and cost.

Negative electrode (anode) materials contain graphite, lithium titanate ($Li_4Ti_5O_{12}$), silicon and so on. Major matrices for material selection include conductivity, volume expansion, energy density and stability.

There is an important concept relevant to degradation of batteries: solid electrolyte interphase layer (SEI). During charge processes, organic solvents decompose on the negative electrodes (e.g., graphite, silicon). With proper electrolytes, the solvent decomposes on the first charging cycle and a solid layer (solid electrolyte interphase layer) is formed. This layer is insulated to electrons, while conductive to ions. This interphase layer inhibits electrolyte decomposition in the following charging cycles. As a popular choice of organic solvents, EC and DMC provides the capability to form stable SEI layers.

1.2.2 Fuel Cells

A fuel cell is composed of an electrochemical reaction system and an auxiliary system. The fuel and oxidant gases comprise the negative and positive electrodes, respectively. **[25]** In a fuel cell, gases are transported within channels to reach electrolytes. Electrolytes can be either liquid or solid. If an electrolyte operates at low temperature, then a noble metal catalyst is usually needed to activate electrochemical reactions.

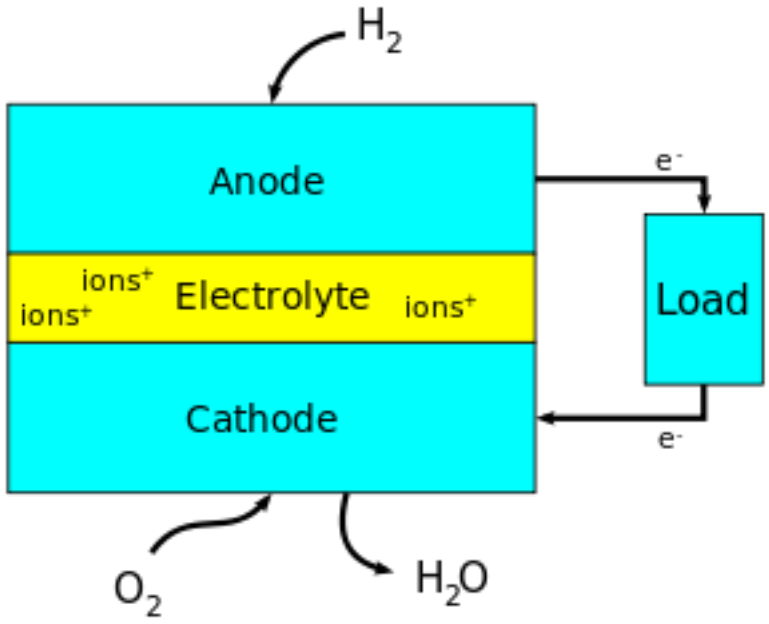

Figure 1-5 A block diagram of a fuel cell. **[24]**

Design features of a fuel cell include:

- the fuel (e.g., hydrogen);

- the electrolyte (liquid or solid);

- the catalyst for the positive electrode (e.g., nickel);

- the catalyst for the negative electrode (e.g., platinum);

- gas diffusion layers.

Unlike typical batteries, fuel cells do not have metals as electrodes but have ones made of gases (with catalyst). Additionally, in the way of reactant storages, fuel cells have all reactants provided from external sources.

A fuel cell has the following advantages:

- it runs with hydrogen without environmental pollution;

- it offers higher thermodynamic efficiency than heat engines;

- it needs fewer energy transformation than those for heat engines;

- it can be applied for vehicles running at low temperatures.

However, it also suffers the following disadvantages:

- hydrogen, the fuel of the system, is usually not easy to produce and store;

- there is requirement on the purity of the fuel;

- water within the cell should not freeze or dry out;

- it needs a complicated control and support system.

1.2.2.1 History and Applications

Applications of fuel cells include powerplants, portable power systems, buses, cars and so on. There are many types of fuel cells. Based on operation temperature, high-temperature fuel cells include molten carbonate fuel cells, solid oxide fuel cells; low-temperature fuel cells include proton exchange membrane fuel cell, alkaline fuel cell and phosphoric acid fuel cells.

1.2.2.2 Operation Principles

1.2.2.2.1 **Solid Oxide Fuel Cells**

A solid oxide fuel cell (SOFC) uses a solid oxide material as its electrolyte to conduct oxygen ions from the positive cathode to the anode.

This type of cell runs at high temperature (500 – 1000 °C). In contrast to low-temperature fuel cells, it does not require noble metal catalyst. It does not suffer from CO catalyst poisoning, but it is vulnerable to sulfur poisoning.

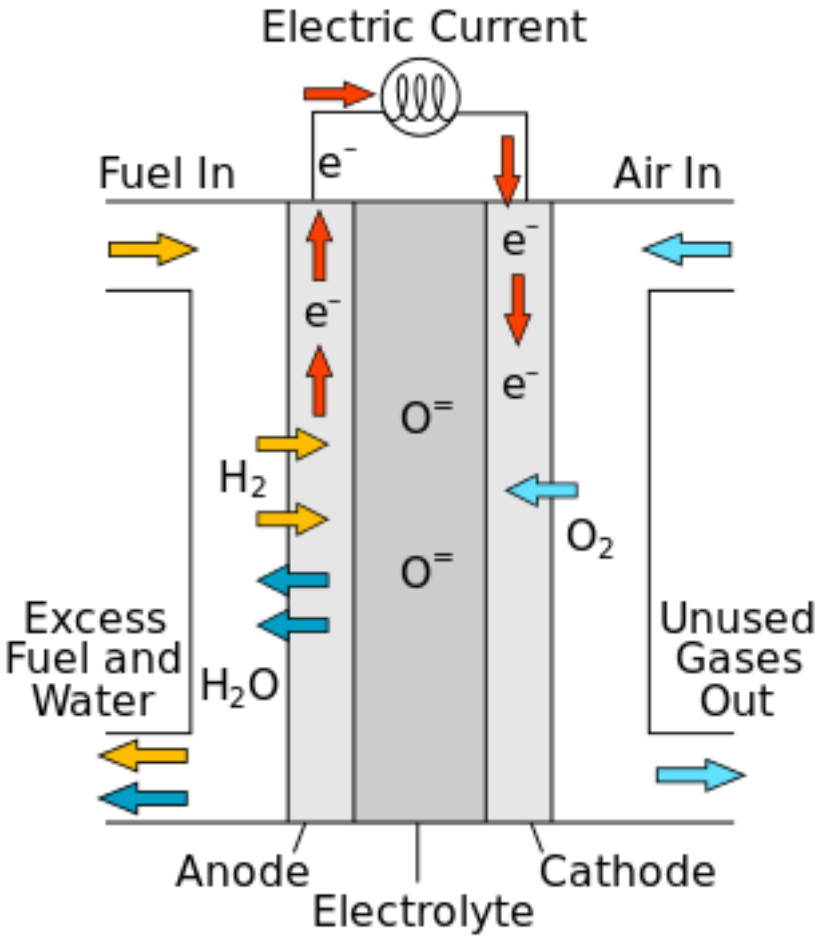

Figure 1-6 Scheme of a solid oxide fuel cell. **[26]**

As for fuel selection, in addition to pure hydrogen, gasoline, jet fuel and biofuels can be used to fuel the cell. It is adoptable to be configured with multiple geometries from planar geometry to tubular geometry.

The following is a scheme of a solid oxide fuel cell. The chemical reactions for the SOFC system can be expressed as

Anode reaction:

$$2H_2 + 2O^{2-} \rightarrow 2H_2O + 4e^-$$

Cathode reaction:

$$O_2 + 4e^- \rightarrow 2O^{2-}$$

And the overall reaction:

$$2H_2 + O_2 \rightarrow 2H_2O$$

The directions of research of SOFCs include lower-temperature SOFCs for reducing costs relevant to materials, insulation and start-up; improving fuel flexibility for improved efficiency under lower operating temperatures; reducing start-up time for mobile applications; 3D printing for simplifying the manufacturing processes.

1.2.2.2.2 **Proton Exchange Membrane Fuel Cells**

Proton exchange membrane fuel cells (PEMFCs) are promising candidates for the emerging electric automobile markets among different types of peering fuel cells, thanks to its high-power density, low operation temperature, fast start-up capability, eco-friendliness. The invention of this type of fuel cell helps addressed issues faced by the family such as extreme operating conditions, expensive materials and limited application scenarios due to large size.

The major application of PEM fuel cells is in the field of transportation because of excellent power density and dynamic characteristics **[27]** They are usually installed on buses installed of cars out of concerns about the available space to hold the entire energy system. Currently, hybrid-power vehicles are more popular than full fuel cell ones. Moreover, there is potential for application in stationary powerplants.

Figure 1-7 shows a scheme of PEMFC and voltage drop across different regions of the cell.

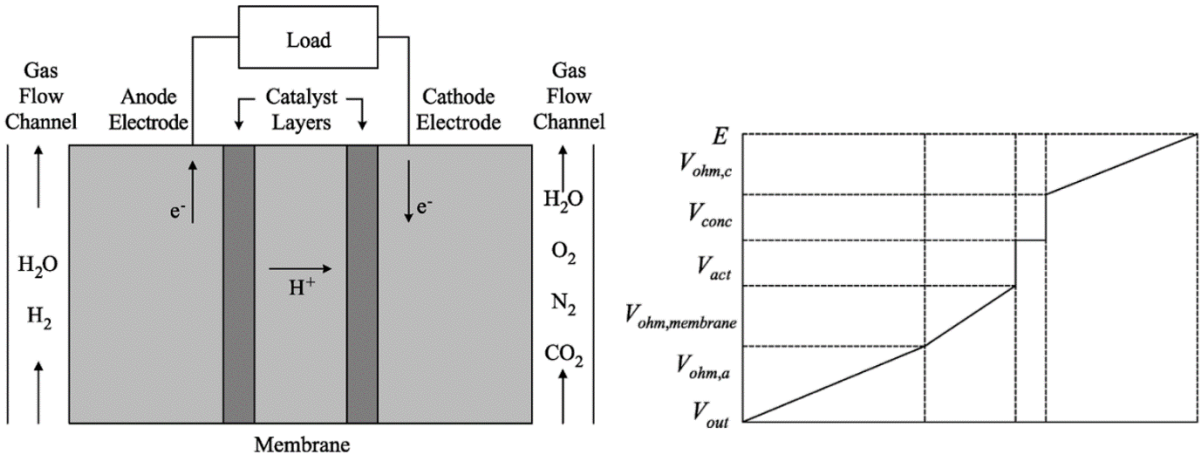

Figure 1-7 scheme of the PEMFC and potential drop across the cell. [28]

The electrochemical reaction system, as the core component, is the place for converting from chemical energy to electric energy. A typical composition of a fuel cell using hydrogen (H_2) as fuel and oxygen (O_2) as oxidant includes two electrodes (anode and cathode), electrolyte, separator and gas intake system. The electrode could be decomposed into two parts: gas diffusion layer (GDL) and catalyst layer. The gas from gas flow channel diffuses through the GDL and reaches the catalyst layer, and then reacts with ions and electrons at the catalyst layer. The auxiliary system has subsystems including fuel storage and supply system, pressure adjustment system (ensuring normal gas transport and electrochemical reaction) and heat exchange system (preheating oxidant and fuel before they enter the reaction system which are all necessary for normal operation of the fuel cell.

The primary electrochemical reactions (with the help of catalyst) is

Cathode reaction:

$$\frac{1}{2}O_2 + 2H^+ + 2e^- \rightarrow H_2O$$

Anode reaction:

$$H_2 \rightarrow 2H^+ + 2e^-$$

And the overall reaction:

$$H_2 + \frac{1}{2}O_2 \rightarrow H_2O$$

Note that the overall reaction is the same as the combustion of hydrogen in oxygen. From Nernst equation, the thermodynamic potential (electromotive force) of PEM fuel cells is

$$E = E^0 + \frac{RT}{2F}\ln\left(\frac{a_{H_2}a_{O_2}^{1/2}}{a_{H_2O}}\right)$$

For the cathode,

$$\varphi_+ = \varphi_+^0 + \frac{RT}{2F}\ln\left(\frac{a_{H^+}a_{O_2}^{1/2}}{a_{H_2O}}\right)$$

For the anode,

$$\varphi_- = \varphi_-^0 - \frac{RT}{2F}\ln\left(\frac{a_{H^+}}{a_{H_2}}\right)$$

1.2.3 Electrochemical Capacitors

Compared to batteries, electrochemical capacitors usually show higher power density but lower energy density.

There are two mechanisms for energy storage in an electrochemical capacitor: electrostatic double-layer capacitance **[31]** and electrochemical pseudocapacitance **[32]**.

For electrostatic double-layer capacitance, active carbon is usually applied as electrode material. Under the application of external voltage, there forms two layers of ions at the electrode. One in the surface lattice of the solid phase of the electrode, while the other is ions in the electrolyte solution attracted by the electrode. Stern's model on electrostatic double-layer capacitance combines Helmholtz's model and Gouy-Chapman's model, some ions adsorbed at the electrode form a compact layer as Helmholtz suggests and the other forms an outer diffuse layer

(including the slipping plane between solid-liquid phase) as Gouy-Chapman's model presents. It could be used to estimate parameters such as capacitance of compact layer and effective thickness and explain how the differential capacitance increases as the solution concentration increases by affecting the effective thickness, though some coarse assumptions result in limitations on it.

For electrochemical pseudocapacitance [33][34], metal oxides or conducting polymers are typical choices for electrode material. Pseudocapacitance is accompanied by a faradic electron charge-transfer between electrode and electrolyte. There is no change on chemical bonds but just charge-transfer. Pseudo capacitors with fast redox reactions enables faster discharging and charging processes than conventional processes.

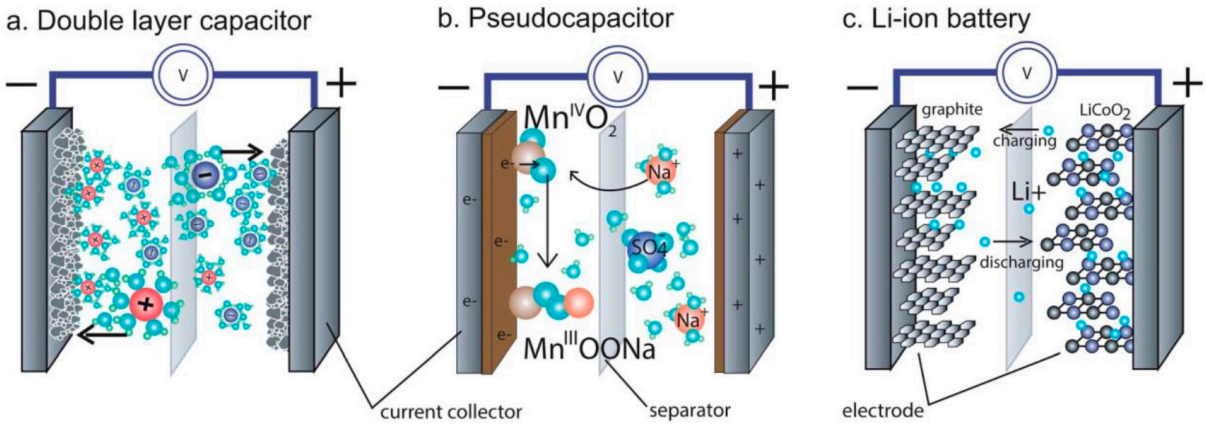

Figure 1-8 Schemes of double-layer capacitor, pseudocapacitor and lithium-ion battery. [33][34]

Then, briefly introduce a promised substance for constructing effective capacitors, tungsten oxide. [35] Its stoichiometric form (WO_3) is semiconducting while its nonstoichiometric form (WO_x, $2 < x < 3$) is electronically conductive. The reversible Proton insertion/extraction reactions

$$WO_3 + xH^+ + xe^- \leftrightarrow H_xWO_3$$

could convert tungsten oxide into electronically conductive tungsten bronze (H_xWO_3, $0 < x < 1$). For $x = 1$, the theoretical capacity is as high as 115 mAh/g.

Chen and coworkers **[35]** reported a hierarchical nanostructured hydrous hexagonal WO3 (h-WO_3) which is capable to conduct both protons and electrons. The biomimetic proton channel is used for proton-transfer while to embedding electron-conducting matrix facilitates fast electron-transfer. This mixed conductivity gives raise to high capacitance and fast discharging/charging capability.

1.3 Thermodynamics and Kinetics

1.3.1 Overview of thermodynamics

An electrochemical cell **[23]** is a unit that could generate electric energy from redox chemical reactions (e.g., lead-acid battery) or facilitate chemical reactions by input of electric energy (e.g., electrolytic cell). It is usually consisted of electrodes (anode and cathode) immersed in electrolyte and separated by separators. When the cell converts chemical energies into electric energies (discharging process), oxidation reactions occur at the anode and electrons are produced, while reduction reactions occur at the cathode and electrons are consumed. The electrons produced at the anode are collected, transported through external circuits to the cathode and being consumed there. In contrast to the external current, ions (cations and anions) are transported in the electrolyte solutions to form the internal current.

Specifically, anions move to the anode while cations move to the cathode. In all, the external current of electrons provides electric energy to connected devices such as bulbs or motors, which is on the price of the chemical energy of the cell. On the other hand, if the cell converts electric energies back into chemical energies (charging process), all the above-mentioned processes still occur, but in inverse direction. And the overall effect is more chemical energy is stored inside the

cell and the electric potential difference between the cathode and the anode is raised up, which are on the price of the input electric current (or electric energy).

To be specific, let us take Daniel cell [23] as an example, which utilizes the redox reaction

$$\mathrm{Zn(s) + Cu^{2+}(aq) \rightarrow Zn^{2+}(aq) + Cu(s)}$$

to convert chemical energy into electric energy.

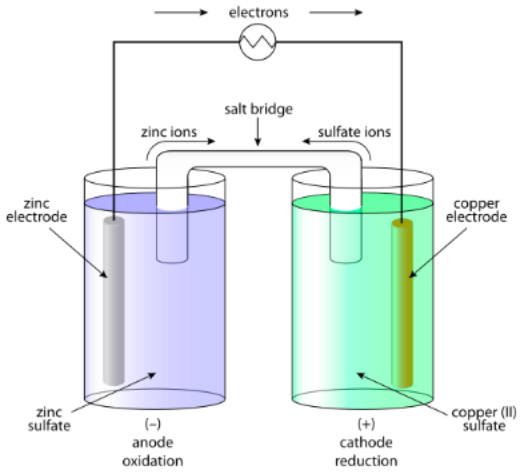

Figure 1-9 Scheme of a Daniel cell. [23]

The solid material for anode is zinc (Zn) bar while that for cathode is copper (Cu) bar. Both of them are connected by an electric wire. The zinc bar is immersed in aqueous solution of zinc sulfate, while the copper bar in aqueous solution of copper sulfate. And the two electrolyte solutions are connected by a salt bridge, which, acting like a separator, allows the passage of ions but detaches two solids. When the cell works, two half-reactions occur at both electrodes. For the anode,

$$\mathrm{Zn(s) \rightarrow Zn^{2+}(aq) + 2e^{-}}$$

where the oxidation reaction occurs and electrons are produced. For the cathode,

$$\mathrm{Cu^{2+}(aq) + 2e^{-} \rightarrow Cu(s)}$$

where the reduction reaction occurs and electrons are consumed.

From thermodynamics, the change of Gibbs free energy of this system is

$$\Delta G = \Delta G^0 + RT\ln\left(\frac{[\mathrm{Zn}^{2+}]}{[\mathrm{Cu}^{2+}]}\right)$$

With the relation between electrochemical potential and change of Gibbs free energy

$$\Delta G = -nFE$$

there is

$$E = E^0 - \frac{RT}{nF}\ln\left(\frac{[\mathrm{Zn}^{2+}]}{[\mathrm{Cu}^{2+}]}\right)$$

We could see that the thermodynamic potential E is determined by the standard thermodynamic potential E^0 and affected by temperature T and concentrations (or more exactly, activities) of reactants. However, due to unbalance between electron demand and supply at the electrodes, which is called electrode polarization **[23]**, there is always some deviation between the actual output voltage and the thermodynamic potential of an electrochemical cell. In other words, not all the chemical potential drained form redox reactions at the electrodes could be converted into electric energies (for discharging processes).

1.3.2 Kinetics and transport

Basically, there are 3 types of electrode polarizations named by their origins: activation polarization, ohmic polarization and concentration polarization.

a) Ohmic polarization. This polarization is originated from obstruction on the electron transport in the solid phase and that on the ion (cation and anion) transport in the electrolyte phase. To improve the electronic conductivity of solid material and ionic conductivity of electrolyte solution could reduce this type of polarization (overpotential).

The ohmic potential could be expressed as

$$|V_{\text{ohmic}}| = IR_{\text{ohmic}}$$

where I is load current density, R_{ohmic} is the cell equivalent ohmic resistance.

b) Concentration polarization.

Due to transport limit, the concentrations of reactants/products at the bulk c_{inf} solution and that at the electrode (interface) c_{s} are not the same. Assume that the transport of species is the rate controlling step, then the equilibrium of the electrochemical reactions could be treated as not broken. Thus, Nernst equation is still applicable, but the concentration (activities) of the species should be changed from values in the bulk to that at the electrode surface.

The concentration overpotential could be expressed as

$$|V_{\text{conc}}| = -\frac{RT}{nF}\ln\left(1 - \frac{I}{Ai_{\text{d}}}\right)$$

where n is the number of electrons involved in the (half) reaction, i_{d} is the limiting diffusion current density.

c) Activation polarization. At thermodynamic equilibrium, the voltage of the cell is the thermodynamic potential and the overall current passing through the cell is 0, i.e., the cathodic reaction and the anodic reaction at each electrode has the same rate. For the macroscopic reactions to occur, rate difference in the two reaction directions should be built up. According to the relation between electric potential and the change of Gibbs free energy of chemical reaction, deviation of the actual potential and thermodynamic potential results in changes of change of Gibbs free energy of both the anodic reaction and the cathodic reaction, it should be noted that these changes are of different signs. Then there are increase in the rate of one of the anodic and cathodic reactions and decrease in that of the other one, so equilibrium is broken and macroscopic reaction in the “favored” direction could be observed: anodic reaction (oxidation) at the anode and cathodic reaction (reduction) at the cathode. This deviation in potential

(overpotential), as the cost of non-zero electric current, is called activation polarization.

The activation overpotential could be expressed as

$$|V_{\text{act}}| = -\frac{RT}{\alpha F}\ln(i_0) + \frac{RT}{\alpha F}\ln\left(\frac{I}{A}\right)$$

where α is transfer coefficient of the electrochemical reaction, i_0 is exchange current density, A is the area of the electrode.

Figure 1-10 demonstrates how the output voltage of a cell changes with the load current density, and the dominant type of polarization during different stages of loading.

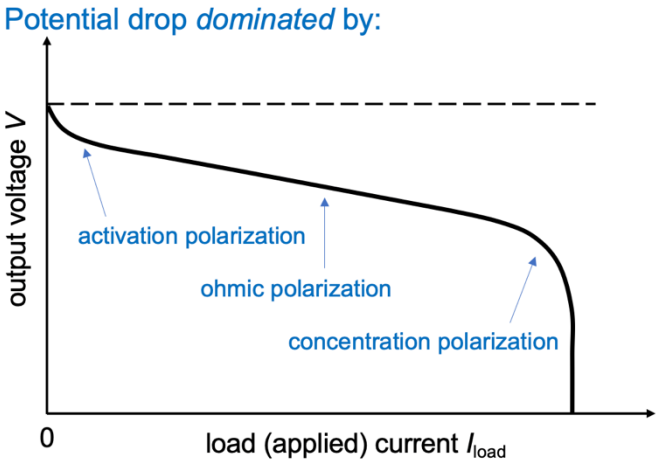

Figure 1-10 Output voltage vs load current for an electrochemical energy storage system. [23]

As a brief discussion, when the loading is small, the polarization is dominated by activation polarization; as the loading increases, the dominant polarization becomes ohmic polarization; when the loading is large, concentration polarization takes the control of internal electrochemical processes.

1.4 Challenges for High Performance Systems

1.4.1 Rate performance

In commonly used electrolytes, lithium ion transference number, defined as the ratio of lithium ion conductivity to the overall ionic conductivity, is usually less than 0.5. As a result, there will be a concentration gradient of electrolyte salt across the electrochemical cell during charging/discharging processes, resulting in a high concentration polarization. This polarization leads to fast change of cell output voltages, especially in high-rate charging/discharging. Moreover, it is also relevant to the parasitic reaction for SEI layer formation, which reduces the amount of cyclable lithium and the overall durability of the whole cell.

1.4.2 Transient response

A proton exchange membrane fuel cell is often operated under transient conditions. The sudden change in load current density usually leads undershoot of output voltage and starvation of fuel [40] which results in problematic decreased power output and shortened overall lifetime.

1.4.3 Longevity

During the lifespan of a lead-acid battery, if the applied rate is high, there will be formation of compact lead sulfate layer on electrodes, which reduces the life of the system.

1.5 Reported Strategies for Performance Improvements

1.5.1 Rate performance

An intuitive strategy is to immobilize anion in electrolytes. For example, grafting anionic segments on parent inorganic particles **[36]**, although a side effect of low ionic conductivity limits wide-range practical applications of this strategy.

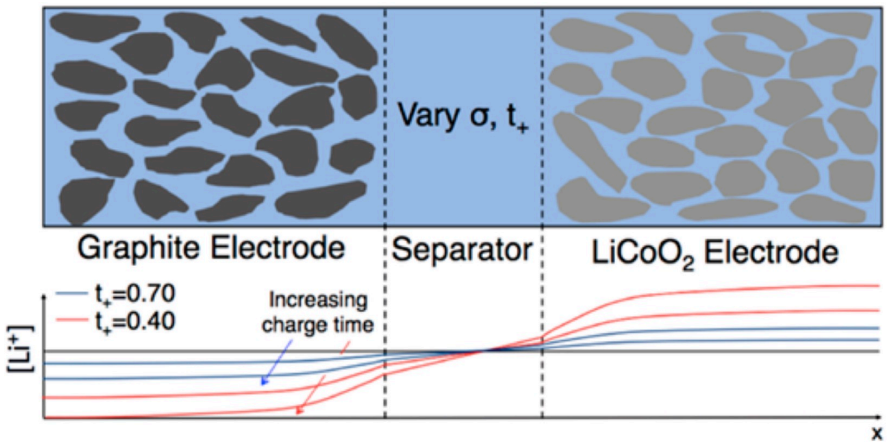

Figure 1-11 Simulated electrolyte salt concentration distribution in a lithium-ion battery during charging with varying values of ionic conductivity and lithium ion transference number. **[37]**

Also, perfluorinated solvent electrolytes **[38]** and nonaqueous polyelectrolyte solutions **[39]** might also be promising solutions **[37]**.

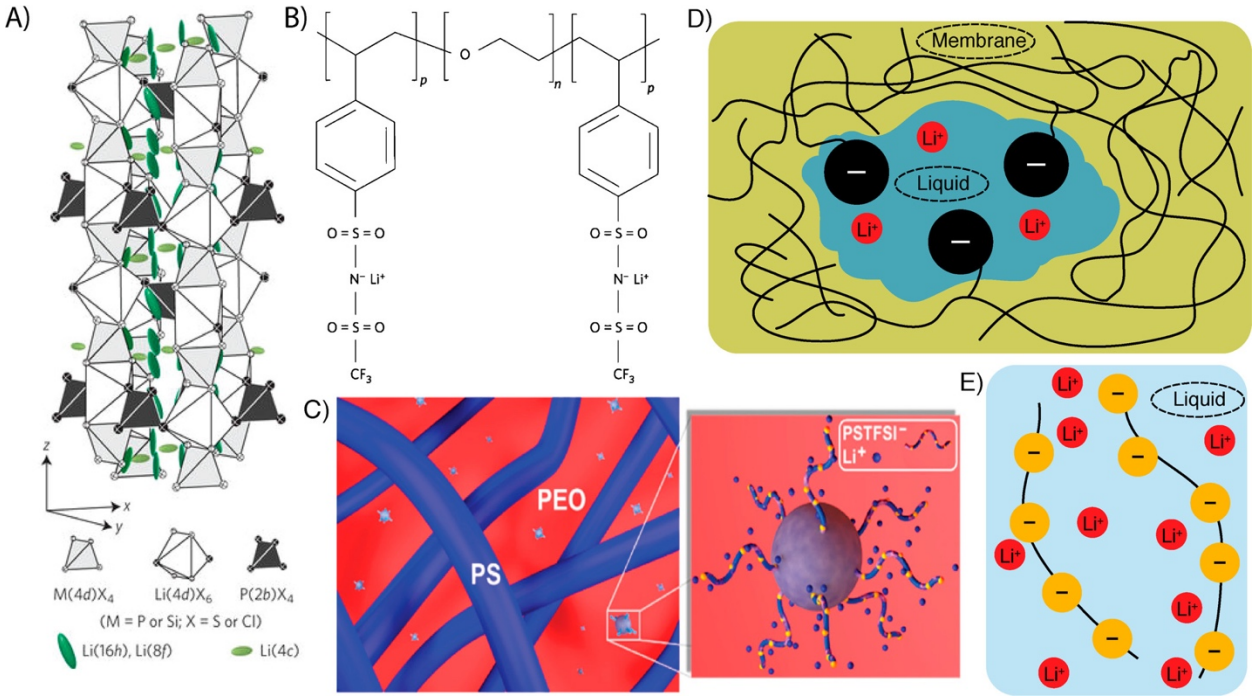

Figure 1-12 Schemes of some high transference number electrolytes. **[37]**

1.5.2 Transient response

To mitigate this problem, researchers have come up with many ways of solutions: improved corrosion resistance **[41]**, water oxidation electrocatalyst in the anode**[42]**, and extra control systems **[43]**. However, solutions with better cost-effect ratio are still under exploration. Moreover, design in flow field plates **[44]** can also help lower the pressure drop of gas and thus stabilize transient responses of a cell.

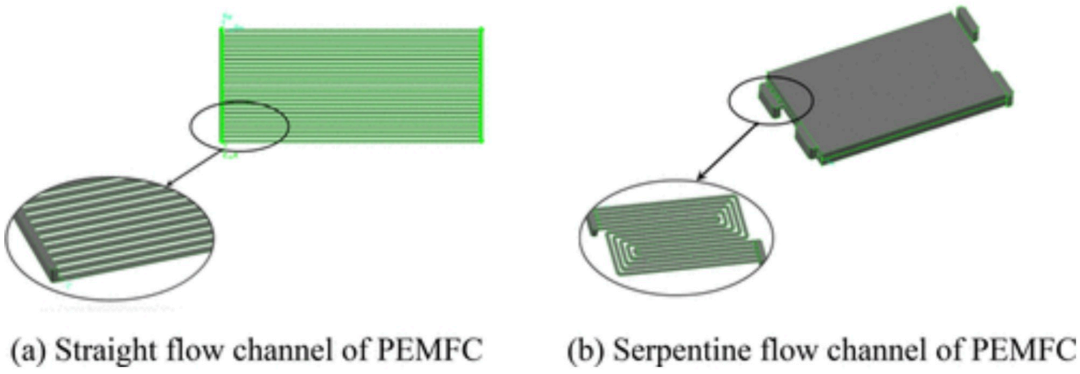

Figure 1-13 Models of gas flow channels. **[44]**

1.5.3 Longevity

Ultrabattery **[45]**, a hybrid device combining supercapacitor with lead-acid battery, by integrating a separator to the electrodes, could limit of formation of the compact lead sulfate layer and thus extend the life of the device.

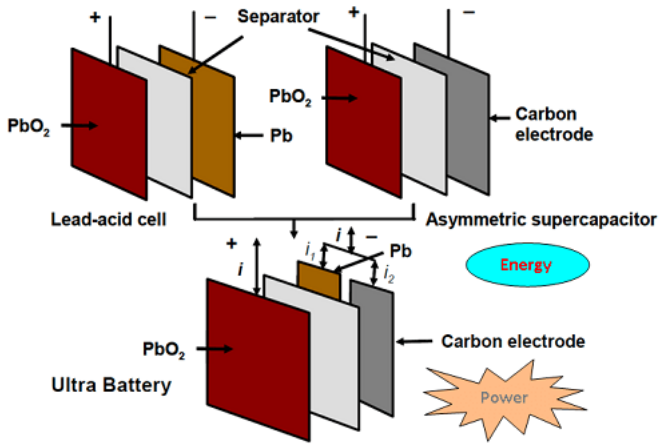

Figure 1-14 Scheme of a ultrabattery. **[46]**

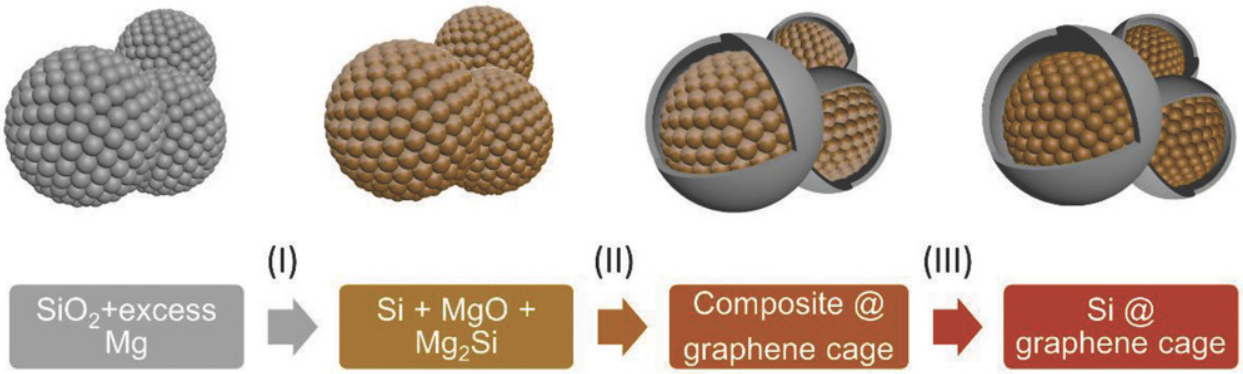

Figure 1-15 Scheme of synthetic routes for Silicon at graphene cage composite. **[47]**

For lithium-ion batteries, silicon is considered as a candidate for anode materials due to abundancy in the nature and high theoretical capacity. However, its large volume expansion during charge processes leads to rapid fading in capacity, limiting its wide application. Nie and coworkers **[47]** reported a novel structural design of hollow graphene-encapsulated Si particles. It constrains the volume expansion of silicon material and thus preserve long-term cycling capacity.

1.6 Model Simulations

Electrochemical devices with high energy density and power density and long recycling life is one of the major goals for research in the field of energy storage and conversion. However, we could see that it is difficult for an electrochemical device to be that perfect. In respect to energy and power density, fuel cell is of high energy density but low power density, lead-acid battery is lack of energy and power density due to relatively large weight, and supercapacitor has high power density but low energy density.

In addition, electrochemical devices face more challenges under some extreme operation conditions. As we know, transport is one of the major application fields of lead-acid batteries and

PEM fuel cells. During the cranking or accelerating period, there is high demand on the output power of the power source. However, under sudden load increase, fuel cell would exhibit undershoot on the output voltage which restricts the output power [48], while lead-acid battery might suffer from the formation of compact lead sulfate layer that shortens the recycling life [49].An intuitive strategy to address these problems is to combine electrochemical capacitors with batteries/ fuel cells. However, there are new requirements being raised (e.g., the compatibility of operational voltage window of the electrode material of two devices). Thanks to numerous explorations, some progresses have been made. For example, it has been discovered by experiments that the addition of WO_3 at the anode of PEM fuel cells could mitigate the undershoot of cell output voltage under sudden load increase. On the other hand, ultrabattery [49], a hybrid device combining supercapacitor with lead-acid battery, could limit of formation of the compact lead sulfate layer and thus extend the life of the device.

Furthermore, people are curious about what is going on for these changes. With knowledge about relations among processes such as mass transport, electrochemical reaction, heat transport within the device, we could have better guide to optimize the design and construction of these devices. Besides doing experiments, modeling **[46]** is an indispensable tool for studying static and dynamic behaviors and develop better control strategies. The models might be coarsely divided into two categories: equivalent circuit and mathematical model.

To build up an equivalent circuit model, it is typical to describe the voltage source and electrode polarization by combinations of circuit elements and then combine them together as an integrated system. Also, thermodynamic properties could be mimicked by appropriate electric circuit through analogies between thermodynamic and electrical quantities.

Table 1-1 Comparisons on several electrochemical cells (devices). [46]

Electrochemical device	Pros	Cons
PEM fuel cell	high energy density; no toxic material	low power density; high cost (platinum catalyst)
Supercapacitor	high power density	low energy density; severe self-discharge
Lead-acid battery	low initial cost; reliable; tolerance to overcharge	short cycle life; low energy and power density; toxic material
Lithium-ion battery	Low cost; Reliable; No toxic material	ageing; protection required

For mathematical models, it could be an *i*-denensional (i = 0, 1, 2, 3) model according to the number of spatial independent variables. The system is generally divided into several subsystems, where conservation equations, constitutive equations and definite conditions (connecting subsystems spatially) are formulated. To solve the governing equation group, numerical methods such as finite element method and finite volume method are usually used.

1.6.1 Equivalent circuits

Wang and coworkers [28] developed a dynamic model for fell cell stack using electrical circuits implemented in MATLAB/SIMULINK and PSPICE. Not just based on empirical equations, it

takes into account the double-layer charging effect and thermodynamic properties of the fuel cell stack. Their model shows good agreement with experimental data for both steady states and transient states.

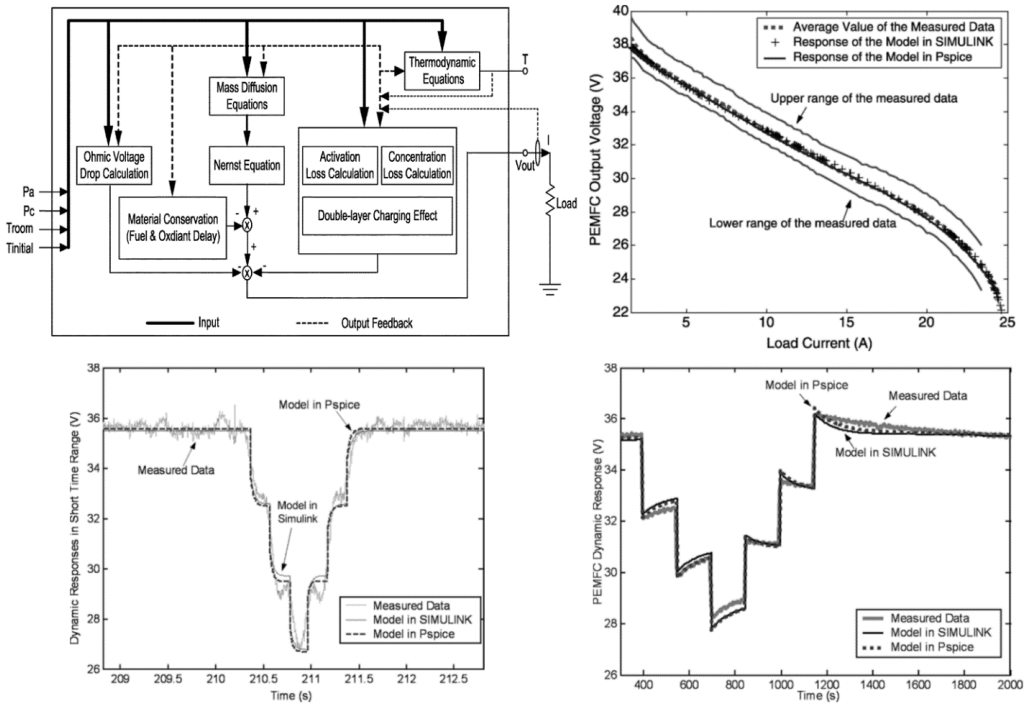

Figure 1-16 Structure of equivalent circuit (ul) and model-experimental comparison under steady (ur) and transient states (d). [28]

1.6.2 Mathematical models

For mathematical modeling, Adzakpa and coworkers [52] developed a mathematical model explaining the transient behaviors of PEMFC by exploring the gas diffusion in the gas diffusion layer (GDL) based on Stefan – Maxwell equation. An analysis on pseudo-2D gas transport in the cathode GDL shows the combination effect of load current change and following inlet air pressure change on the electrode potential, which partially explains the undershoot of output voltage under sudden load current density increase. In addition, using mathematical models with

similar structure, Ceraolo and coworkers [53]explains the voltage overshoots with the variation of proton concentration at the catalyst layer.

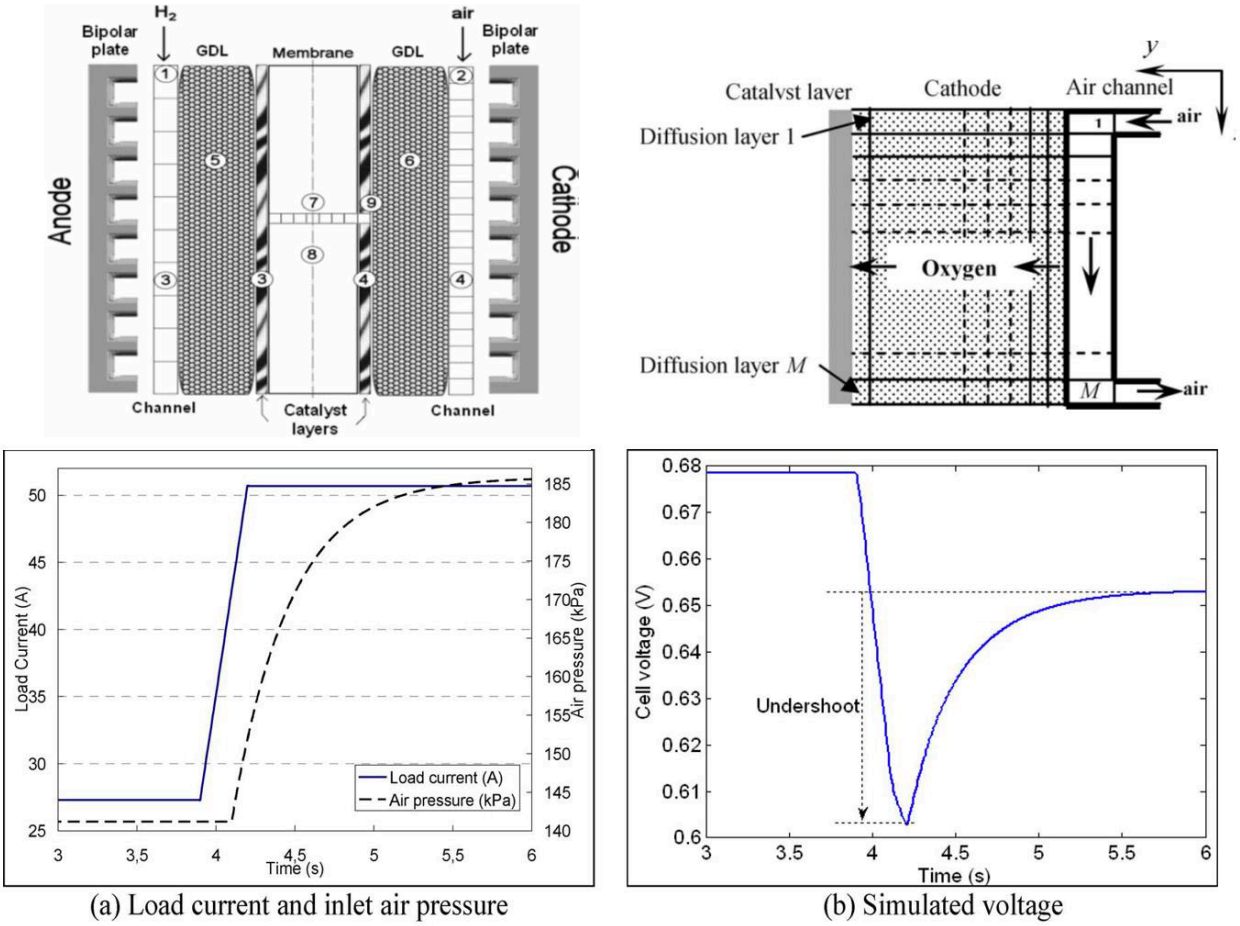

(a) Load current and inlet air pressure

(b) Simulated voltage

Figure 1-17 Scheme of PEMFC (ul), mesh for pseudo 2D gas diffusion layer(ur) and input(ll) and output(lr) of dynamic response. [52]

Jackey from The Mathworks, Inc. [54] developed a simple and effective model for lead-acid battery using equivalent circuits. After parameter tuning, this model is a powerful tool for cell component selection. Basically, it has interconnected blocks including battery equivalent circuit (voltage loss due to electrode polarization), charge and capacity block (calculating remaining available capacity and thus updating thermodynamic potential of the cell) and thermal model (calculating temperature from heat transfer and thus updating relative physical quantities). It is

worth noting that the real-time updating of remaining available capacity and thermodynamic potential contributes significantly to the accuracy of the model.

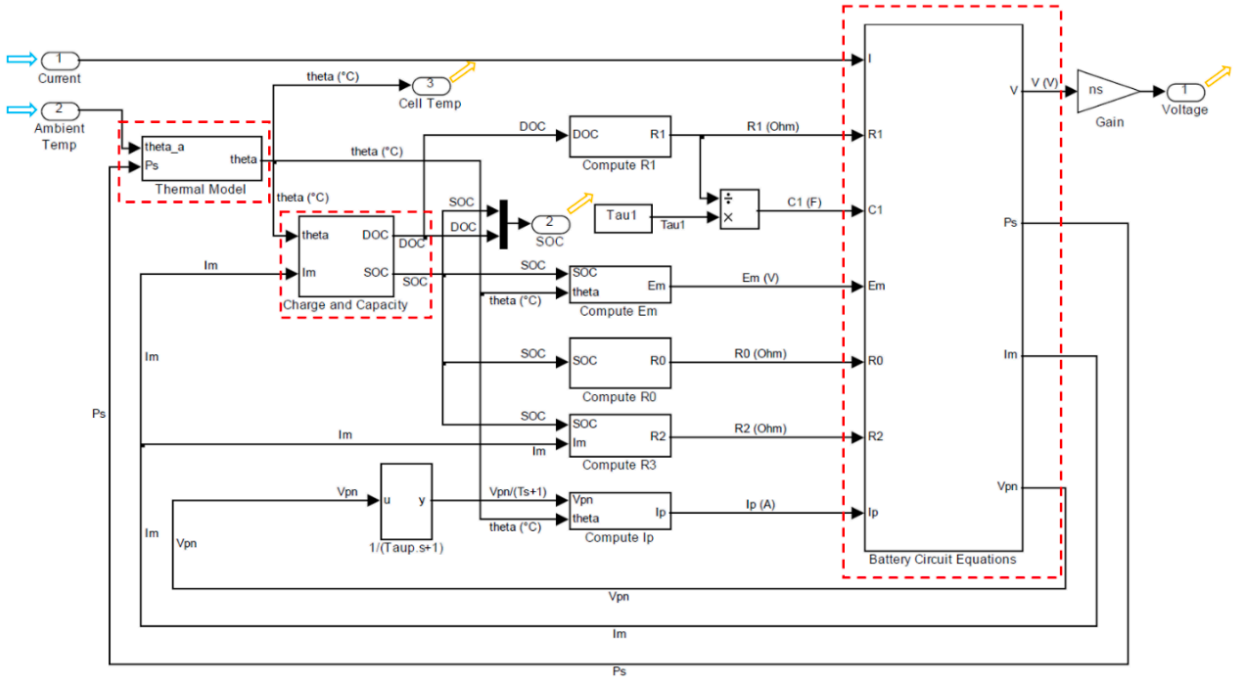

Figure 1-18 Model structure in SIMULINK platform (red box: blocks; blue arrow: input; yellow arrow: output). [54]

1.7 Goal of the Dissertation

In this dissertation, the focus is the design and simulation for addressing bottlenecking performance challenges of popular and promising energy storage systems. To be specific,

- dynamic response under load change of proton exchange membrane fuel cells,

- high rate discharging behavior of lithium-ion batteries,

- remaining useful lives under cycling of lithium-ion batteries.

With the addition of tungsten oxide, a promised candidate of supercapacitor, improved dynamic performances are observed for PEM fuel cells. With the addition of MOF particles in electrolyte, higher rate performance and cycling lives of lithium-ion batteries are exhibited. Thus, model-

based methods including equivalent circuits and mathematical models are applied to search for the possible characterization and explanation. Moreover, when large battery data set and sufficient computational resources are available, data-driven methods such as artificial neural networks are also applied to learn and predict latent patterns for battery remaining useful lives.

1.8 References

[1] Höök, Mikael, and Xu Tang. "Depletion of fossil fuels and anthropogenic climate change—A review." *Energy policy* 52 (2013): 797-809.

[2] Electricity explained. https://www.eia.gov/energyexplained/electricity/electricity-in-the-us.php.

[3] Electricity generation in the world in the year of 2015. http://www.eia.doe.gov/emeu/international/electricitygeneration.html.

[4] Shao, Yuanlong, et al. "Design and mechanisms of asymmetric supercapacitors." *Chemical reviews* 118.18 (2018): 9233-9280.

[5] Xie, Jing, and Yi-Chun Lu. "A retrospective on lithium-ion batteries." *Nature Communications* 11.1 (2020): 1-4.

[6] AbuaqilahMasoud, Khalid, and RowidaAyoubAbdelkader Amina Ahmed Saeed. "Ion Lithium battery." (2019).

[7] Myung, Seung-Taek, et al. "Nickel-rich layered cathode materials for automotive lithium-ion batteries: achievements and perspectives." *ACS Energy Letters* 2.1 (2017): 196-223.

[8] Agnolucci, Paolo. "Economics and market prospects of portable fuel cells." *International Journal of Hydrogen Energy* 32.17 (2007): 4319-4328.

[9] Corbo, Pasquale, Fortunato Migliardini, and Ottorino Veneri. *Hydrogen fuel cells for road vehicles*. Springer Science & Business Media, 2011.

[10] Farhadi, Mustafa, and Osama Mohammed. "Adaptive energy management in redundant hybrid DC microgrid for pulse load mitigation." *IEEE Transactions on Smart Grid* 6.1 (2014): 54-62.

[11] Espinar, Bella, and Didier Mayer. "The role of energy storage for mini-grid stabilization." (2011).

[12] Choi, Nam-Soon, et al. "Challenges facing lithium batteries and electrical double-layer capacitors." *Angewandte Chemie International Edition* 51.40 (2012): 9994-10024.

[13] Cooper, A., et al. "The UltraBattery—A new battery design for a new beginning in hybrid electric vehicle energy storage." *Journal of Power Sources* 188.2 (2009): 642-649

[14] Lukic, Srdjan M., et al. "Power management of an ultracapacitor/battery hybrid energy storage system in an HEV." *2006 IEEE Vehicle Power and Propulsion Conference*. IEEE, 2006.

[15] Xiong, Rui, Linlin Li, and Jinpeng Tian. "Towards a smarter battery management system: A critical review on battery state of health monitoring methods." *Journal of Power Sources* 405 (2018): 18-29.

[16] Bavarian, Mona, et al. "Mathematical modeling, steady-state and dynamic behavior, and control of fuel cells: A review." *Industrial & engineering chemistry research* 49.17 (2010): 7922-7950.

[17] Dubarry, Matthieu, and Bor Yann Liaw. "Identify capacity fading mechanism in a commercial LiFePO4 cell." *Journal of Power Sources* 194.1 (2009): 541-549.

[18] Maher, Kenza, and Rachid Yazami. "A study of lithium ion batteries cycle aging by thermodynamics techniques." *Journal of Power Sources* 247 (2014): 527-533.

[19] Wognsen, Erik Ramsgaard, et al. "A score function for optimizing the cycle-life of battery-powered embedded systems." *International Conference on Formal Modeling and Analysis of Timed Systems*. Springer, Cham, 2015.

[20] Zou, Yuan, et al. "Combined state of charge and state of health estimation over lithium-ion battery cell cycle lifespan for electric vehicles." *Journal of Power Sources* 273 (2015): 793-803.

[21] Qiuting, Wang, Jiang Yinzhu, and Lu Yunhao. "State of health estimation for lithium-ion battery based on D-UKF." *International Journal of Hybrid Information Technology* 8.7 (2015): 55-70.

[22] Xiong, Rui, et al. "A double-scale, particle-filtering, energy state prediction algorithm for lithium-ion batteries." *IEEE Transactions on Industrial Electronics* 65.2 (2017): 1526-1538.

[23] Li, D. (1999). *Principle of Electrochemistry*. Beihang University Press.

[24] Daniell cell. (2017, September 4). In *Wikipedia, The Free Encyclopedia*. Retrieved 04:09, October 27, 2017, from https://en.wikipedia.org/w/index.php?title=Daniell_cell&oldid=798889166.

[25] Fuel cell. https://en.wikipedia.org/wiki/Fuel_cell.

[26] Fuel Cell Technology. https://www.energy.gov/sites/prod/files/2014/03/f12/fcm04r0.pdf.

[27] Solid oxide fuel cell. https://en.wikipedia.org/wiki/Solid_oxide_fuel_cell.

[28] Wang, Yun, et al. "A review of polymer electrolyte membrane fuel cells: Technology, applications, and needs on fundamental research." *Applied energy* 88.4 (2011): 981-1007.

[29] Wang, Caisheng, M. Hashem Nehrir, and Steven R. Shaw. "Dynamic models and model validation for PEM fuel cells using electrical circuits." *IEEE transactions on energy conversion* 20.2 (2005): 442-451.

[30] Huang, Pei-Hsing, Jenn-Kun Kuo, and Chun-Yen Huang. "A new application of the UltraBattery to hybrid fuel cell vehicles." *International Journal of Energy Research* 40.2 (2016): 146-159.

[31] Dunn, Bruce, Haresh Kamath, and Jean-Marie Tarascon. "Electrical energy storage for the grid: a battery of choices." *Science* 334.6058 (2011): 928-935.

[32] Srinivasan, Supramaniam. "Electrode/electrolyte interfaces: Structure and kinetics of charge transfer." *Fuel Cells*. Springer, Boston, MA, 2006. 27-92.

[33] Halper, Marin S., and James C. Ellenbogen. "Supercapacitors: A brief overview." *The MITRE Corporation, McLean, Virginia, USA* (2006): 1-34.

[34] Le, Zaiyuan, et al. "Pseudocapacitive sodium storage in mesoporous single-crystal-like TiO2–graphene nanocomposite enables high-performance sodium-ion capacitors." *ACS nano* 11.3 (2017): 2952-2960.

[35] Jost, Kristy, Genevieve Dion, and Yury Gogotsi. "Textile energy storage in perspective." *Journal of Materials Chemistry A* 2.28 (2014): 10776-10787.

[36] Chen, Zheng, et al. "Hierarchical nanostructured WO3 with biomimetic proton channels and mixed ionic-electronic conductivity for electrochemical energy storage." *Nano letters* 15.10 (2015): 6802-6808.

[37] Tu, Zhengyuan, et al. "Designing artificial solid-electrolyte interphases for single-ion and high-efficiency transport in batteries." *Joule* 1.2 (2017): 394-406.

[38] Diederichsen, Kyle M., Eric J. McShane, and Bryan D. McCloskey. "Promising routes to a high Li+ transference number electrolyte for lithium ion batteries." *ACS Energy Letters* 2.11 (2017): 2563-2575.

[39] Oh, Hyukkeun, et al. "Poly (arylene ether)-based single-ion conductors for lithium-ion batteries." *Chemistry of Materials* 28.1 (2016): 188-196.

[40] Smiatek, Jens, Andreas Wohlfarth, and Christian Holm. "The solvation and ion condensation properties for sulfonated polyelectrolytes in different solvents—a computational study." *New Journal of Physics* 16.2 (2014): 025001.

[41] Cho, Junhyun, Han-Sang Kim, and Kyoungdoug Min. "Transient response of a unit proton-exchange membrane fuel cell under various operating conditions." *Journal of Power Sources* 185.1 (2008): 118-128.

[42] Zhang, T., Wang, P., Chen, H. & Pei, P. A review of automotive proton exchange membrane fuel cell degradation under start-stop operating condition. Appl. Energ. 223, 249–262 (2018).

[43] Dubau, L. et al. A review of PEM fuel cell durability: materials degradation, local heterogeneities of aging and possible mitigation strategies. WIRES Energy Environ. 3, 540–560 (2014).

[44] Oszcipok, M., Riemann, D., Kronenwett, U., Kreideweis, M. & Zedda, M. Statistic analysis of operational influences on the cold start behaviour of PEM fuel cells. J. Power Sources 145, 407–415 (2005).

[45] Liu, Y. F., et al. "Lowering the Pressure Drop and Cost of a Proton Exchange Membrane Fuel Cell by Flow Field Plate Design." *Energy & Fuels* 34.7 (2020): 8857-8863.

[46] Lam, L. T., et al. "Failure mode of valve-regulated lead-acid batteries under high-rate partial-state-of-charge operation." *Journal of Power Sources* 133.1 (2004): 126-134.

[47] Gou, J. (2012). *Modeling and analysis of lead-acid batteries with hybrid lead and carbon negative electrodes*. The Pennsylvania State University.

[48] Nie, Ping, et al. "Graphene caging silicon particles for high-performance lithium-ion batteries." *Small* 14.25 (2018): 1800635.

[49] Pei, Pucheng, and Huicui Chen. "Main factors affecting the lifetime of Proton Exchange Membrane fuel cells in vehicle applications: A review." *Applied Energy* 125 (2014): 60-75.

[50] Lam, L. T., Louey, R., Haigh, N. P., Lim, O. V., Vella, D. G., Phyland, C. G., & Kano, T. (2007). VRLA Ultrabattery for high-rate partial-state-of-charge operation. *Journal of Power Sources*, *174*(1), 16-29.

[51] Gou, J. (2012). *Modeling and analysis of lead-acid batteries with hybrid lead and carbon negative electrodes*. The Pennsylvania State University.

[52] Wang, C., Nehrir, M. H., & Shaw, S. R. (2005). Dynamic models and model validation for PEM fuel cells using electrical circuits. *IEEE transactions on energy conversion*, *20*(2), 442-451.

[53] Adzakpa, K. P., Agbossou, K., Dube, Y., Dostie, M., Fournier, M., & Poulin, A. (2008). PEM fuel cells modeling and analysis through current and voltage transient behaviors. *IEEE Transactions on Energy Conversion*, *23*(2), 581-591.

[54] Ceraolo, M., Miulli, C., & Pozio, A. (2003). Modelling static and dynamic behaviour of proton exchange membrane fuel cells on the basis of electro-chemical description. *Journal of power sources*, *113*(1), 131-144.

[55] Jackey, Robyn A. "A simple, effective lead-acid battery modeling process for electrical system component selection." *SAE Transactions* (2007): 219-227.

Chapter 2 Dynamic Response of PEM Fuel Cells with WO_3

2.1 Introduction

Figure 2-1 shows the design of a hybrid proton exchange membrane fuel cell with a tungsten oxide layer added to the anode.

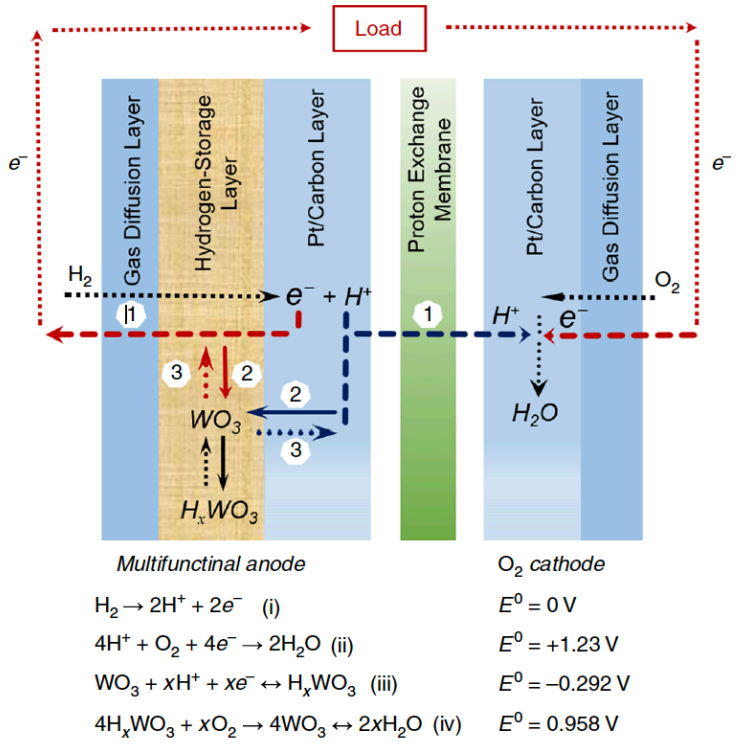

Figure 2-1 Design scheme of a hybrid PEMFC with WO_3. [1]

Figure 2-2 shows the comparison on steady and transient states between PEMFC with and without WO_3 addition. For steady state of fuel cell, we focus on the polarization curve. It could be roughly divided into 2 regions with different slopes: activation polarization dominating region

and ohmic polarization dominating region. Interestingly, there is no obvious steep drop of voltage following the ohmic polarization dominating region, which might indicate that concentration polarization (diffusion limitation) under steady state could be ignored. Moreover, from the comparison of hybrid cell and control cell, the addition of WO_3 could reduce ohmic polarization.

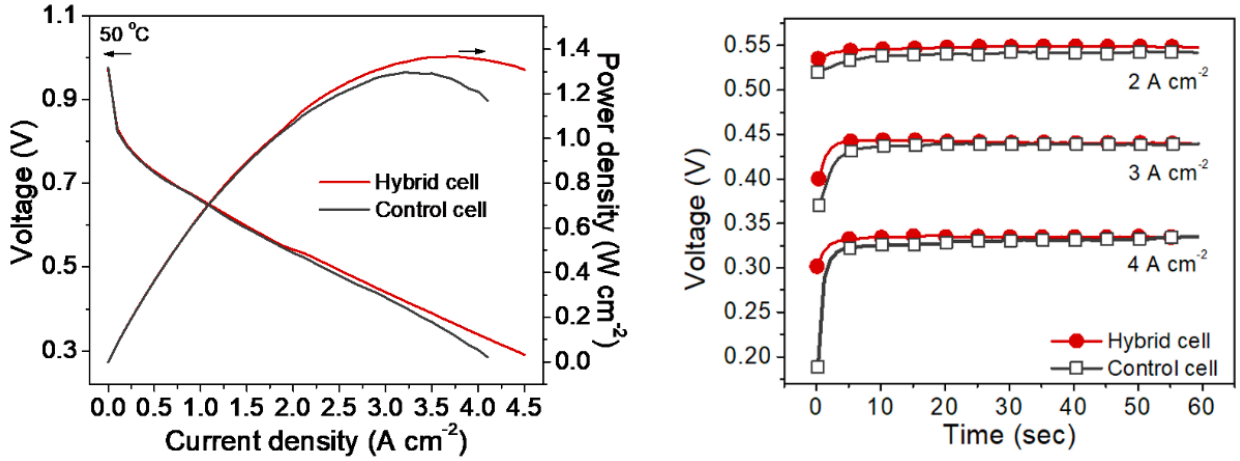

Figure 2-2 Comparison on steady (l) and transient states (r) between PEMFC with and without WO_3 addition.

For dynamic response of fuel cell, there are at least 3 relative issues: i) double-layer charging effects, ii) delays of fuel and oxidant flow, and iii) thermodynamic characteristics of the cells. [2] However, for the double-layer charging effect, the time constant is small (less than 1 s) due to the small value of equivalent resistance accounting for the activation and concentration loss. On the other hand, the time range of the thermodynamic response seems long (about a few minutes). Since the time scale of the dynamic response of interest is about 10 s, we mainly focus on fuel and oxidant flow delays, which belongs to concentration polarization (diffusion limitation). Specifically, for the load change test, as the current density steps up, the voltage initially drops below its steady value and then recovers to the steady value (rate of increasing is $\mathrm{d}E/\mathrm{d}t \cong A \cdot \exp(-t/\tau)$, where A and τ are constants). It might be understood in this way: as the applied

current density increases suddenly, the demand of hydrogen and oxygen for electrochemical reactions also increases suddenly. However, the supply of hydrogen and oxygen could increase gradually only. Thus, the accumulation of negative charge at the cathode and positive charge at the anode increases suddenly, followed by the gradual mitigating. What is being reflected on the voltage of fuel cell is the sudden drop followed by gradual resilience.

Furthermore, in the fuel cell with addition of WO3 at the anode, the reversible reaction

$$\mathrm{WO_3} + x\mathrm{H^+} + x\mathrm{e^-} \leftrightarrow \mathrm{H}_x\mathrm{WO_3}$$

would favor the backward direction (generating WO_3). Then the H^+ generated by this reaction would be diffused through the PEM to the cathode and increase the potential of cathode which is suffering from too much electron accumulation. (We just ignore the effect at the anode since the dynamic polarization at the anode is much smaller compared to that at the cathode.) Thus, the intensity of dynamic response due to delays of fuel and oxidant flow could be mitigated.

As an analogy, a parallel connection of a resistor and an inductor shares similar behaviors. The inductance (self-inductance) is a property of a closed circuit that it generates a counter-electromotive force to resist the change of current density. If the current density through this parallel connection steps up, there will be a step drop on voltage at the beginning followed by resilience (rate of increasing is also "negative exponential", $A \cdot \exp(-t/\tau)$). Thus, similar dynamic response tendency is shared by the fuel cell and parallel connection of a resistor and an inductor.

Therefore, in the equivalent circuit model, we introduce a parallel connection of inductor and resistor to reflect the dynamic effect of delays of oxidant and fuel flow. Wang and coworkers [1] have established an equivalent circuit model for fuel cell. It is worth mentioning that equation (22) and (23) in their model, which are applied to include the dynamic response of fuel cell due

to delays of oxidant and fuel flow, could be transformed into a parallel connection of inductor and resistor in the equivalent circuit. It should be noted that there might be no obvious inductance for real physical processes in the cells, but we just utilize the analogy between delays of oxidant and fuel flow and the concept of inductance to build up the equivalent circuit model.

2.2 Results and Discussion

2.2.1 Equivalent circuit with (*LR*) unit for dynamic response

Basically, in the equivalent model, i) voltage source U_0 stands for the internal voltage, and R_{ohmic} stands for ohmic loss in the proton exchange membrane, ii) parallel connection of resistor R_{e} and capacitor C_{e} stands for the electrode (resistor for activation and concentration loss, and capacitor for double-layer charging effect), and iii) parallel connection of resistance R_L and inductor L is used for reflecting the dynamic delays of oxidant and fuel flow.

With the addition of Tungsten Oxide (WO_3) in the anode, i) the intensity (undershoot) of dynamic response is reduced, and ii) the stable voltage also slightly increases. Correspondingly, in the equivalent circuit, i) the addition of another parallel connection of resistor R_{w} and inductor L_{w} paralleling with the original ($R_L L$) connection could mitigate the delays of oxidant and fuel flow, and ii) the resistor R_{w2} and capacitor C_{w2} paralleling with ($R_{\text{e}}C_{\text{e}}$) could decrease equivalent internal resistance and thus increases the stable voltage of the cell. Equivalently, we could just tune the values of R_L, L and R_{e} to reflect the effect of WO_3.

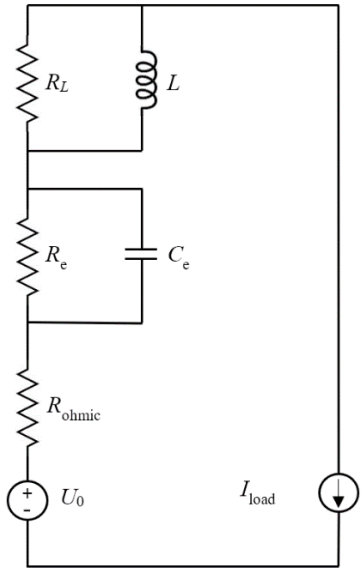

Figure 2-3 Equivalent circuit for PEMFC.

From model-experimental comparison, experimental data could be used to estimate values of parameters in the equivalent circuit model. It is noted that the physical quantities are functions of both temperature and load current density. For simplicity, it is assumed that with the range of exploration, most of parameters are linear functions of temperature/load current density.

1. Thermodynamic voltage minus activation loss, U_0 - V_{ohmic}, and overall equivalent resistance R_e for electrodes.

They could be estimated from the stable values of voltage under different test conditions,

$$U_{\text{stable}} = U_0 - V_{\text{ohmic}} - I \cdot R_e$$

2. Parallel connection of resistance R_L and inductance L (also R_w and L_w).

For the dynamic responses of the cell, the undershoot of voltage is,

$$U_{\text{undershoot}} \cong \Delta I \cdot R_L$$

approximately (neglecting double-layer charging effects). And the time constant is

$$\tau = L/R_L$$

which is about 1/5 of the time for the cell to reach stable voltage after step increase of current density.

3. Equivalent parameters for anode and cathode R_e and C_e (also R_{w2}, C_{w2}).

From the initial part of dynamic response (less than 1s, mutual combination of both double-layer charging effect and delays of oxidant and fuel flow), time constant for the double-layer charging effect, RC, could be estimated to be about 0.05 s~0.30 s.

For simple estimation, we assume that most parameters are linear functions of temperature and current density.

However, for equivalent resistance of dynamic response R_L, we apply the method of least squares to fit a quadratic function of current density and linear function of temperature.

Generally, as temperature increases, internal voltage increases while both equivalent resistance and capacitance decrease. At relative low temperature, the equivalent resistance is observably dependent on the current density.

For the delays of oxidant and fuel flow under step load change, L decreases as temperature increases while R_L increases as temperature/current density increases, whose overall effect includes non-linear increasing of voltage undershoots as load current densities increases and decreasing of resilience time as temperature increases. The changes of L_W and R_W have similar tendencies but with smaller intensities. The following figures and table exhibit the tentative simulation results. It should be noted that the possible problem of *overfitting* might exist.

Table 2-1 Estimated expressions of parameters of PEMFC.

Parameter	Estimated expression (unit: load current density I in A/cm^2, temperature T in °C)	
Temperature	@ 30°C	@ 50°C
U_0 -I· R_{ohmic} (V)	0.735	0.750
R_L ($\Omega \cdot cm^2$)	-5.37×10^{-5} $-7.6\times10^{-3}\times I$ $+2.8\times10^{-3}\times I^2$ $+4\times10^{-4}\times T$ (control) $5\times10^{-4}+0.001\times I+5\times10^{-5}\times T$ (hybrid)	
L ($H \cdot cm^2$)	0.180 (control) 0.051 (hybrid)	0.050 (control) 0.014 (hybrid)
R_e ($\Omega \cdot cm^2$)	$0.114+0.001\times I$ (control) $0.112+0.001\times I$ (hybrid)	0.107 (control) 0.106 (hybrid)
C_e (F/cm^2)	1.2	0.2

Table 2-2 Equivalent resistance of dynamic response R_L (Omega cm^2) (red: with WO3 addition).

	@ 30°C	@ 50°C
2 A/cm^2	0.008	0.016
	0.004 ↓	0.005 ↓
3 A/cm^2	0.014	0.022
	0.005 ↓	0.006 ↓
4 A/cm^2	0.026	0.034
	0.006 ↓	0.007 ↓

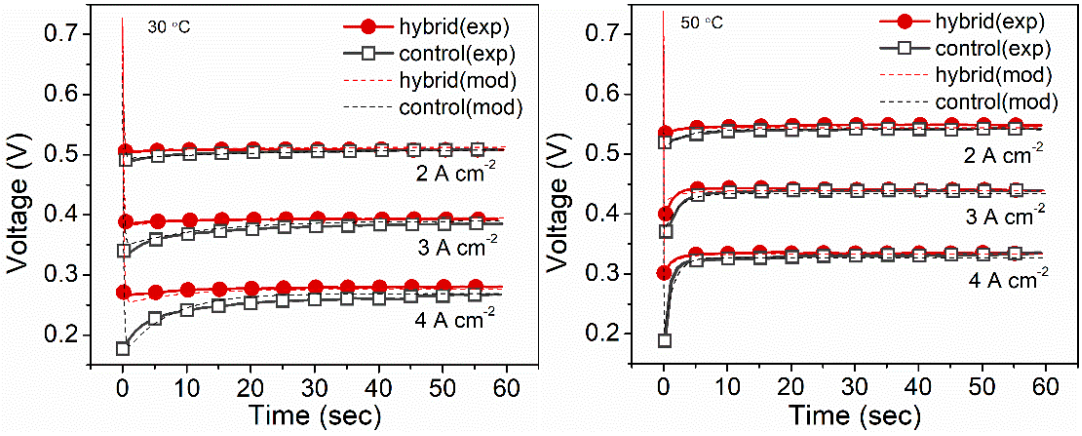

Figure 2-4 Model-experimental comparison for dynamic response of PEMFC under load change.

2.2.2 Delay of mass transport in gas diffusion layer

The focus of this section is gas transport [3] in the gas diffusion layer [4] which might provide an explanation for the phenomena of voltage undershoot during load step change.

Figure 2-5 shows a scheme of a gas diffusion layer (GDL) sandwiched by a catalyst later and a gas flow channel. From the viewpoint of gas transport, the gas flow channel is a source providing the fuel cell with gas fuel/oxidant, the catalyst layer is a sink consuming gas, and the gas diffusion layer serves as a pathway for the gas to be transported from the source to the sink.

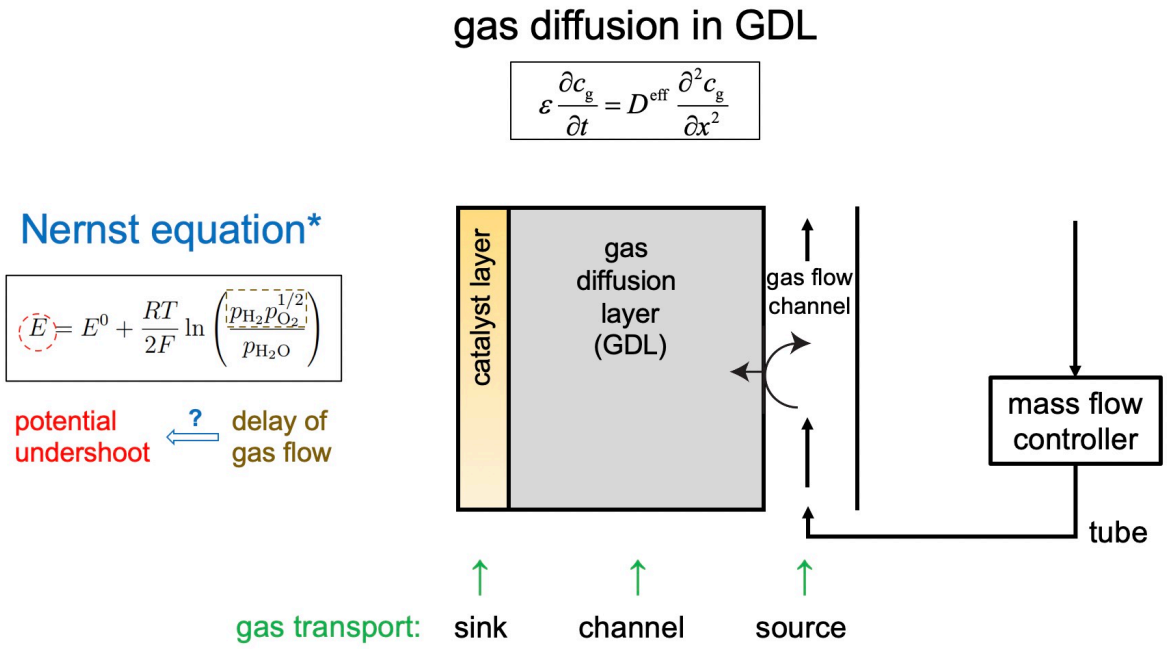

Figure 2-5 Scheme of a gas diffusion layer sandwiched by a catalyst later and a gas flow channel for gas transport.

The high-level reasoning is that, when a sudden change in the applied load/current density occurs, there are associated changes in the current density of electrochemical reactions at the catalyst layer and the inlet flux of gas (delayed by the transport in external supplies) at the gas flow channel. The change in the reaction current density, buffed by the double layer at the interface between the catalyst layer and GDL, adjusts the demand on the gas (at the interface

between the catalyst layer and GDL); the change in the inlet flux of gas, delayed by the external devices, adjusts the supply on the gas (for the entire cell). Moreover, the gas transport through the gas diffusion layer (from the gas flow channel to the catalyst layer) also delays the change in the supply on the gas (at the interface between the catalyst layer and GDL). At a closer look on the catalyst layer-GDL interface, due to different time constants for above-mentioned processes relevant to gas, there is a transient change in the gas concentration/pressure in addition to a more stable change. For example, with a step increase in load current density, there are increases in both the reaction current density and the gas inlet flux. Ultimately, at a stable state, the gas concentration will be increased, with matched demand and supply. Before reaching the stable state, the change of reaction current density is usually faster than the change of gas inlet flux plus the gas transport through GDL, indicating that the increase of the demand changes faster than that of the supply. During this transient time period of gas demand-supply mismatch, as the demand is higher than the supply, there is a decrease on the local concentration/pressure of the gas for "compensation" at the interface between the catalyst layer and GDL. Consider the Nernst equation [5]

$$E = E^0 + \frac{RT}{2F}\ln\left(\frac{p_{\mathrm{H_2}} p_{\mathrm{O_2}}^{1/2}}{p_{\mathrm{H_2O}}}\right)$$

The cell potential (electromotive force) is relevant to the pressure of gases. During the transient period, at the catalyst layer-GDL interface, the decrease of gas pressure results in the decrease of the cell potential. Moreover, the output voltage [6] of the cell can be expressed as

$$V = E - V_{\mathrm{Ohm}} - V_{\mathrm{Act}} - V_{\mathrm{Conc}}$$

In the literature [9], the activation overpotential is constant. In addition, the concentration overpotential is usually negligible. Thus, the change of the cell output voltage is subject to the

change of the cell potential and the ohmic overpotential. Generally, an increase in the applied current density leads to an increase of the ohmic overpotential and a decrease of the cell output voltage. together with the change of the cell potential, the cell output voltage exhibits a undershoot transiently and then recovers to a stable value. The stable value is lower than the initial value, while the trough of the undershoot is even lower than the stable value.

The next question to answer is, how the addition of the hydrogen-storage layer of tungsten oxide helps mitigate the undershoot under load changes. To be simple, with the additive layer between the catalyst layer and GDL, the equivalent capacity of the double layer is improved, resulting in a stronger “reservoir” of reactant gases. In this way, under sudden change of load current density, by adjusting the change of the double layer current density, it helps delay the change of the reaction current density and mitigate the temporal gap between the demand and the supply on gas. Thus, the change of local gas concentration/pressure becomes reduced. So do the cell potential and output voltage.

The major transport phenomenon occurs in the gas diffusion layer, as indicated by name, is diffusion, while convection and migration are ignored. For simplicity, just assume 1-deminsion transport (although 2-dimension seems more convincing as gas transport along the orientation of the gas flow channel and the direction from the gas flow channel to the catalyst layer are different): the gas is diffused from the gas flow channel-GDL interface to the catalyst layer-GDL interface (spatial coordinate x starts at the gas flow channel-GDL interface). The governing equation for the gas transport within this layer can be expressed as [7]

$$\varepsilon \frac{\partial c}{\partial t} = D^{\text{eff}} \frac{\partial^2 c}{\partial x^2}$$

The gas flow channel provides the fuel cell with gases as reactants. In the interface with the gas diffusion layer, the boundary condition is

$$-D^{\text{eff}}\frac{\partial c}{\partial x} = N_{\text{inlet}}$$

Typically, the inlet flux is proportional to the applied load/current density at any time. However, there will be a delay in the adjustment of inlet fluxes when there is a sudden change on the load. An explanation is that the gas flow channel is connected to a mass flow controller via a tube. When the load is changed, the mass flow controller also changes the gas flux with very small delay. Due to an unignorable length of the tube, the change needs some time to take affects in the gas flow channel.

The catalyst layer consumes gases for electrochemical reactions. The associated boundary condition for the interface between the catalyst layer and the gas diffusion layer is

$$-D^{\text{eff}}\frac{\partial c}{\partial x} = \frac{i_{\text{reaction}}}{nF}$$

There are two coexisting components: one is a double layer [8] and the other is the electrochemical reaction. They could be viewed as a capacitor and a resistor in an equivalent circuit model, respectively. As they are configured in parallel connection, they share the load current density together as two branches. Given a sudden change in load current density, there is no sudden change in the reaction current density, as the voltage of the double layer capacitor (the same to that of the reaction resistor) cannot change suddenly.

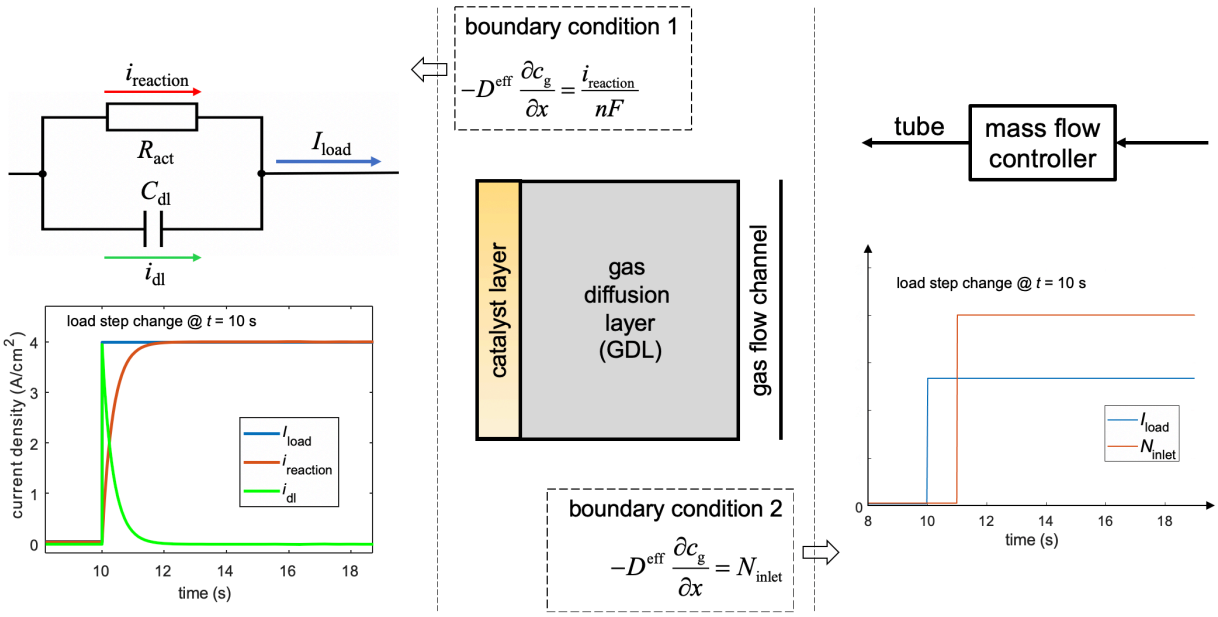

Figure 2-6 Boundary conditions for gas transport in the gas diffusion layer. [10]

MATLAB function pdepe is utilized to obtain a numerical solution for the problem. The input values of the parameters are shown in Table 2-3:

Table 2-3 Input values of model parameters for gas transport in gas diffusion layer. [10]

Parameter	Symbol and unit	Input value
Initial gas concentration at the inlet of GDL	$c_{\text{l.0}}$ (mol/m^3)	6×10^{1}
Reference temperature	T_{ref} (K)	303
Reference diffusion coefficient of gas in GDL	D_{ref} (m^2/s)	8×10^{-7}
Thickness of the gas diffusion layer	L (m)	2.5×10^{-4}
porosity	ε	0.8
tortuosity	τ	3.4
Time for gas passing through the tube	t_{tube} (s)	0.16
Time constant for gas transport from convection into diffusion	τ_{c2d} (s)	1.5
Time constant of double-layer effect	τ_{dl} (s)	0.25

As for boundary conditions on the gas flow channel side, there is a step change of inlet flux of gases as well as a step change of applied current density. Notice that the change of inlet gas flux is delayed by about 1 second due to the setting of operations.

It is assumed gas transport is rate-controlling step, and thus far slower than electrochemical reaction (electron transfer step).

However, the electrochemical reaction is not at quasi-equilibrium state (could be seen from existence of activation loss).

For the case $T = 30$ °C and $I = 4$ A/cm^2, Figure 2-7 displays numerical results of gas concentration distribution in GDL. After the load step increase, there are immediate drops of gas concentrations in different locations of the gas diffusion layer, which should be relevant unbalanced gas demand and supply at the catalyst layer-GDL interface. Eventually, gas concentration reaches stable values at different locations and also form a stable concentration gradient for gas diffusion.

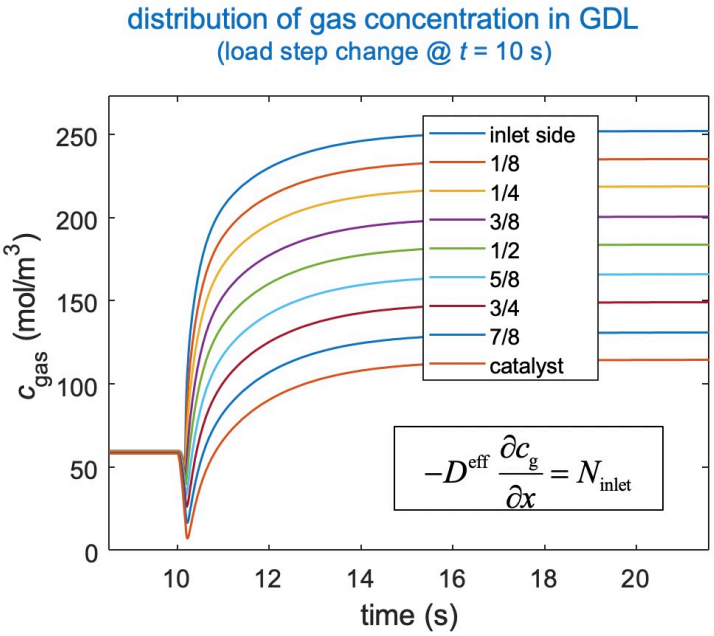

Figure 2-7 Numerical results of gas concentration distribution in GDL ($T = 30$ °C and $I = 4$ A/cm^2).

Moreover, Figure 2-8 shows the influences of temperature and changed load current density on gas diffusion induced dynamic response of electric potential. Also, Figure 2-9 shows the influences of temperature and changed load current density on gas diffusion induced dynamic response of the output voltage of the cell.

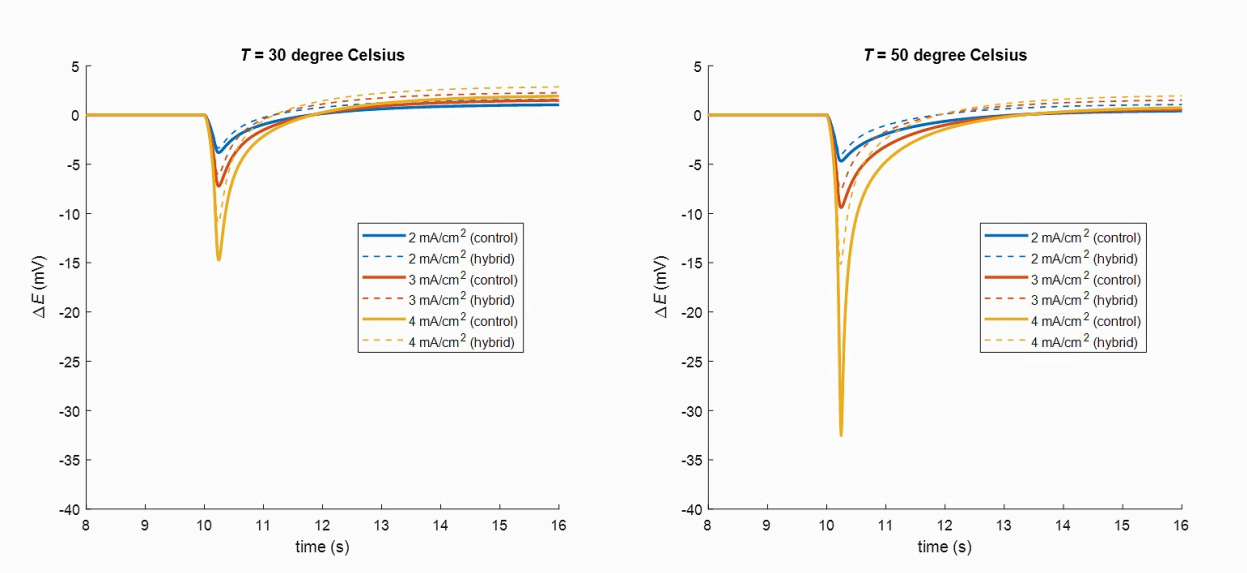

Figure 2-8 Influence of temperature and load change on dynamic response of cell potential.

At 30 °C, the dynamic response of electrode potential is less intensive than that at 50 °C. And under smaller range of load change, there is smaller undershoot in potential than that larger change on load current density. These preliminary results are consistent with experimental data, though the values are deviated to some extends.

With the addition of WO_3, the equivalent capacitance at the electrode interface (of the anode) should be changed, will it affect the gas diffusion in GDL and then the electrode potential? Figure 2-10 shows the comparison between the dynamic response of the gas diffusion of the fuel cell with various values of time constant of double-layer effect τ_{dl} (or double-layer capacitance C_{dl}). We could see that the change of time constant of double-layer effect could affect dynamic response of electrode potential.

As discussed before, the interface of GDL with gas flow channel could be viewed as a source of gas and that with catalyst layer as sink of gas. Under steady states, there is a balance between of gas "supply" of the source and "demand" of the sink. When sudden change of load current density occurs, the source manages to increase the supply while the sink increases the demand. Since the sink has higher rate of response than the source (although they will finally reach a new balance), or demand is larger than supply, the gas molecules accumulated at the surface of catalyst layer is consumed by the sink to meet the demand of the sink and results in the decrease in the concentration of gas at the catalyst layer and thus the decrease in the potential of the

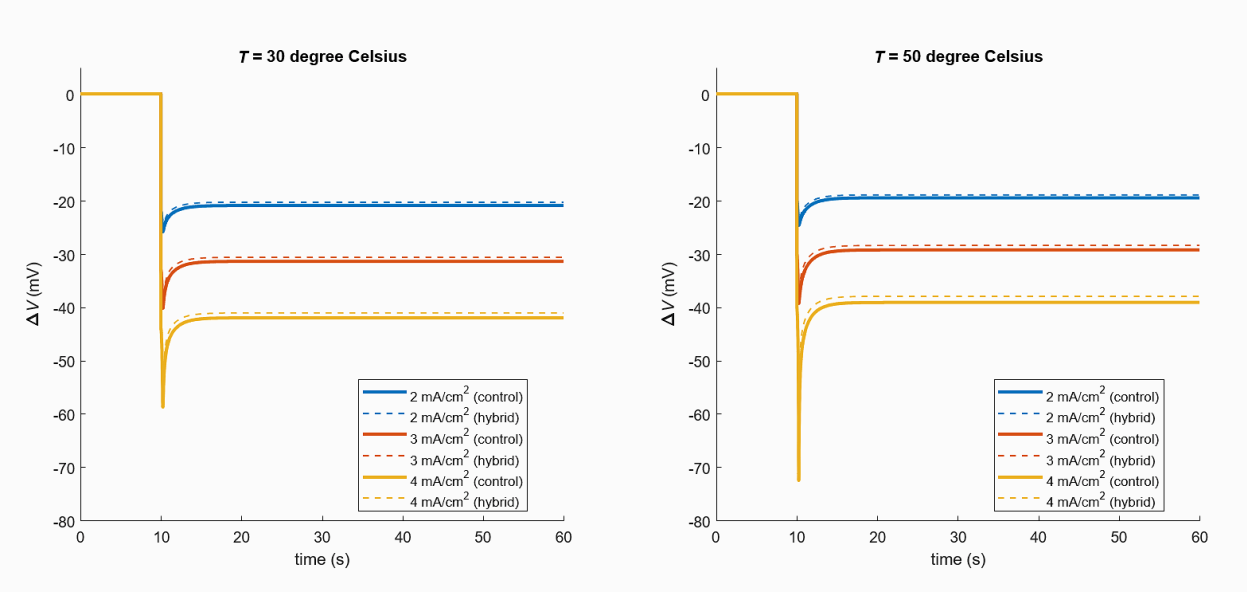

Figure 2-9 Influence of temperature and load change on dynamic response of cell output voltage.

electrode. With introduction of WO_3, the double-layer capacitance is improved. In other words, the rate of sink response is slowed down. Thus, the unbalance between the supply and demand of the gas right after the load change is mitigated. And consumption of accumulated gas molecules at the catalyst layer surface and electrode potential drop are both reduced.

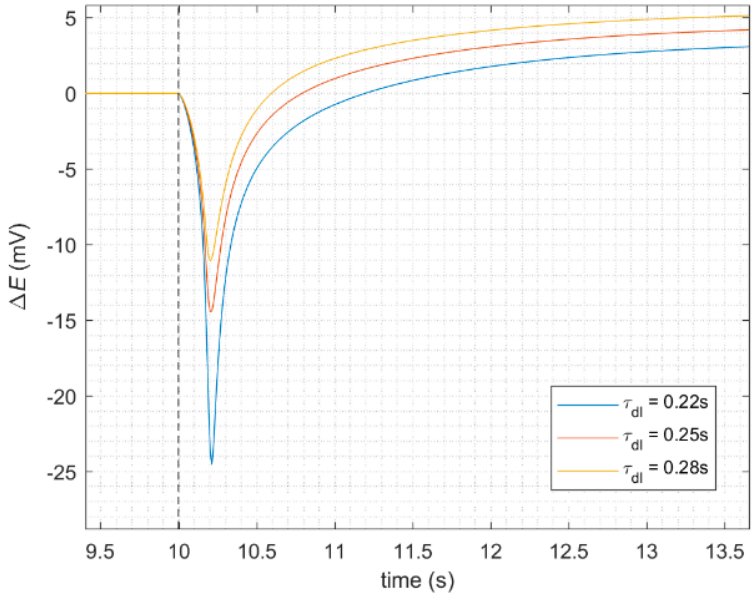

Figure 2-10 Influence of double-layer capacitance on dynamic response of gas transport in GDL.

Note that there is no perfect match between the data of the observed experiments and simulation model. System identification [11] might be a way to search model parameters that fit observed data excellently. However, there is still a risk of overfitting as there are many parameters compared to available observed data.

2.2.3 Delay of mass transport in proton exchange membrane: WO_3 as H^+ reservoir

During normal operations of a fuel cell, protons are generated at the anode and consumed at the cathode. And the intermediate proton exchange membrane takes the role of proton transport. Thus, the anode is a source, the cathode is a sink, and the membrane is a channel for proton transport.

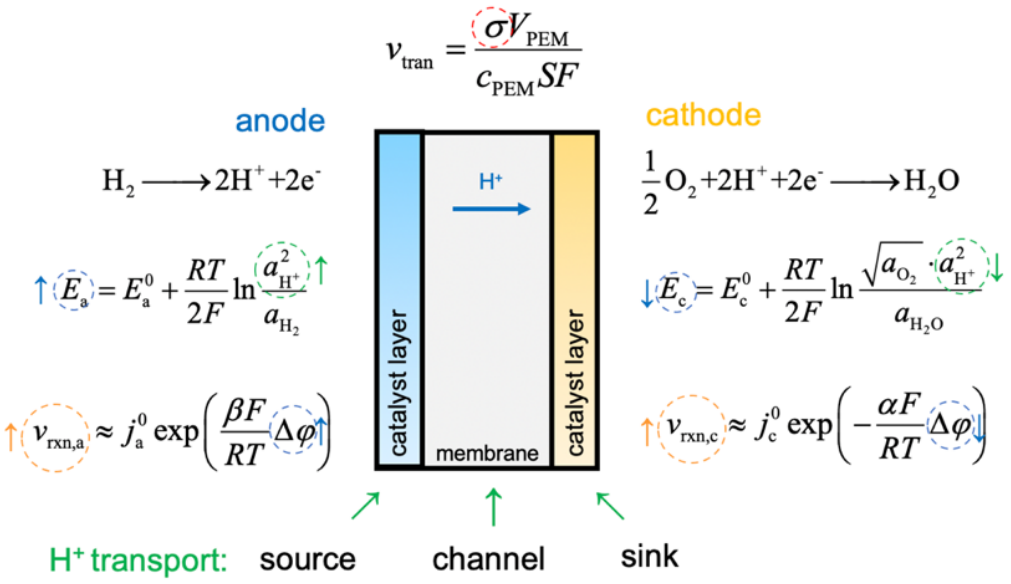

Figure 2-11 illustration of proton migration in the proton exchange membrane of a fuel cell.

When the applied current density of the fuel cell has a step increase, the proton conductivity [13] of the proton exchange membrane might undergo an undershoot followed by recovery. At the sudden decrease of proton conductivity of the membrane, and the transport of protons through the membrane gets delayed, resulting in the accumulation of protons at the anode and depletion at the cathode. Consider Nernst equation, the electrode potential gets increased at the anode side while decreased at the cathode size, reducing the overall cell potential. During the recovery, the proton conductivity of the membrane gradually resumes to a relatively high value, and helps facilitating proton transport, resulting in the decrease of proton concentration at the anode and increase at the cathode (still not equal to original level). Consider Nernst equation again, the electrode potential gets decreased at the anode side while increased at the cathode size, increasing the overall cell potential (still lower than original level given higher applied current density).

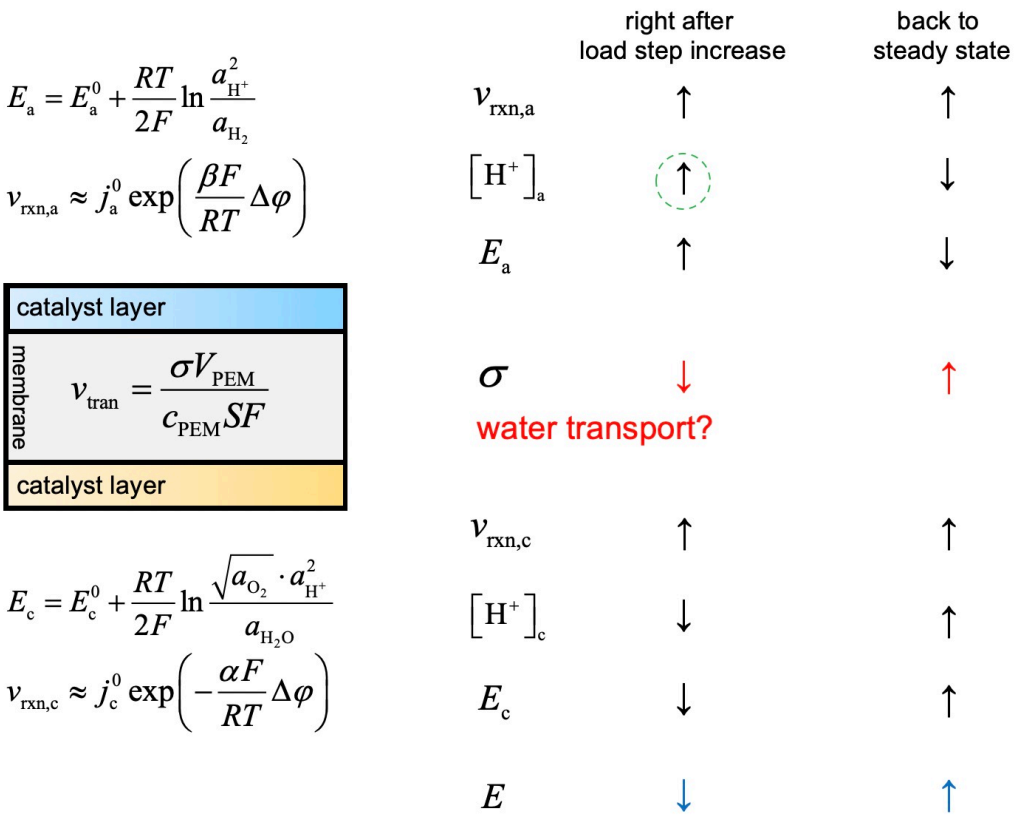

Figure 2-12 Property variation right after load step increase and back to steady state in a PEM fuel cell.

With the addition of a capacitor-like tungsten oxide layer at the anode, during the undershoot right after load change, the accumulation of protons at the anode could be mitigated, as WO_3 works as a buffer of protons and the concentration of protons does not increases too much. In this way, the increase of electrode potential at the anode and the decrease of the overall cell potential are inhibited.

Note that the transient response of proton conductivity in the membrane might be relevant to water transport [14] through the membrane.

2.3 Conclusion

In this section, the focus is explaining transient responses of proton exchange membrane fuel cells (with tungsten oxide addition to anode).

An equivalent circuit model is employed to characterize dynamic responses of PEMFCs under transient operations and the improved power performance achieved by a system design of integrating a WO_3 layer with anodes.

To explain what is going on within the fuel cell system and the contribution of the system design, a mathematical model simulating gas transport within the gas diffusion layer attributes voltage undershoot under transient operations to unbalance between the demand of gas at the catalyst layer and the supply at gas flow channel (through the gas diffusion layer).

Moreover, it is also observed that the addition of WO_3 layers increases the capacity of the double layer, buffers the change of reaction current density, mitigates the transient gas demand-supply unbalance, and thus improves power performance under transient operations.

2.4 References

[1] Shen, Gurong, et al. "Multi-functional anodes boost the transient power and durability of proton exchange membrane fuel cells." *Nature communications* 11.1 (2020): 1-10.

[2] Wang, Caisheng, M. Hashem Nehrir, and Steven R. Shaw. "Dynamic models and model validation for PEM fuel cells using electrical circuits." *IEEE transactions on energy conversion* 20.2 (2005): 442-451.

[3] Wang, Y., & Wang, C. Y. (2005). Transient analysis of polymer electrolyte fuel cells. *Electrochimica Acta*, *50*(6), 1307-1315.

[4] Rowe, A., & Li, X. (2001). Mathematical modeling of proton exchange membrane fuel cells. *Journal of power sources*, *102*(1-2), 82-96.

[5] Pasricha, S., & Shaw, S. R. (2006). A dynamic PEM fuel cell model. *IEEE Transactions on Energy Conversion*, *21*(2), 484-490.

[6] Zhao, D., Dou, M., Zhou, D., & Gao, F. (2016). Study of the modeling parameter effects on the polarization characteristics of the PEM fuel cell. *International Journal of Hydrogen Energy*, *41*(47), 22316-22327.

[7] Cindrella, L., Kannan, A. M., Lin, J. F., Saminathan, K., Ho, Y., Lin, C. W., & Wertz, J. (2009). Gas diffusion layer for proton exchange membrane fuel cells—A review. *Journal of Power Sources*, *194*(1), 146-160.

[8] Conway, B. E., & Pell, W. G. (2003). Double-layer and pseudocapacitance types of electrochemical capacitors and their applications to the development of hybrid devices. *Journal of Solid State Electrochemistry*, *7*(9), 637-644.

[9] Khan, M. J., and M. T. Iqbal. "Modelling and analysis of electro-chemical, thermal, and reactant flow dynamics for a PEM fuel cell system." *Fuel cells* 5.4 (2005): 463-475.

[10] Adzakpa, K. P., et al. "PEM fuel cells modeling and analysis through current and voltage transient behaviors." *IEEE Transactions on Energy Conversion* 23.2 (2008): 581-591.

[11] Meiler, M., Schmid, O., Schudy, M., & Hofer, E. P. (2008). Dynamic fuel cell stack model for real-time simulation based on system identification. *Journal of Power Sources*, *176*(2), 523-528.

[12] Ceraolo, M., Miulli, C., & Pozio, A. (2003). Modelling static and dynamic behaviour of proton exchange membrane fuel cells on the basis of electro-chemical description. *Journal of power sources*, *113*(1), 131-144.

[13] Lee, C. H., Park, H. B., Lee, Y. M., & Lee, R. D. (2005). Importance of proton conductivity measurement in polymer electrolyte membrane for fuel cell application. *Industrial & engineering chemistry research*, *44*(20), 7617-7626.

[14] Janssen, G. J. M., & Overvelde, M. L. J. (2001). Water transport in the proton-exchange-membrane fuel cell: measurements of the effective drag coefficient. *Journal of Power Sources*, *101*(1), 117-125.

Chapter 3 Rate/cycling Performance of LIBs with MOF

3.1 Introduction

In the section, we focus on exploring rate/cycling performances of lithium-ion battery cells with/without addition of metal-organic frameworks (MOF). Basic introduction to MOF, geometries with MOF addition and relevant transport properties are also discussed.

3.1.1 Calculation of Sand's time

Consider an electrochemical cell with two lithium/copper foils as electrodes separated by *dilute binary* electrolyte solution. [1] Define

$$D_{\text{app}} = \frac{z_c\mu_c D_c - z_a\mu_a D_a}{z_c\mu_c - z_a\mu_a}$$

Based on Nernst-Einstein relation, there are

$$D_{\text{app}} = \frac{2D_cD_a}{D_c+D_a},\ t_a = 1 - t_c = \frac{D_a}{D_c+D_a},\ D_{\text{app}} = 2D_ct_a = 2D_at_c,\ \frac{D_c}{D_a} = \frac{z_c\mu_c}{-z_a\mu_a}$$

Assume *double layers* are small enough to be ignored, the electrolyte concentration profile could be solved with the method of separation of variables:

$$\tilde{c} = 1 + \tilde{J}\left\{\frac{1}{2} - \tilde{x} - \frac{4}{\pi^2}\sum_{n=0}^{\infty}\frac{\exp[-\pi^2(2n-1)^2\tilde{t}]}{(2n-1)^2}\cos[\pi(2n-1)\tilde{x}]\right\}$$

where dimensionless variables/parameters are defined as

$$\tilde{c} = c/c_0,$$

$$\tilde{x} = x/L,$$

$$\tilde{t} = t/\left(\frac{L^2}{D_{\text{app}}}\right),$$

$$\tilde{J} = J/\left(\frac{2z_0c_0FD_{\text{app}}}{Lt_a}\right) = J/\left(\frac{4z_0c_0FD_c}{L}\right)$$

If $|\tilde{J}| \leq 2$, then as $\tilde{t} \to \infty$, then the *exponential* terms of the electrolyte concentration profile will vanish, leaving

$$\tilde{c} \to 1 + \tilde{J}\left(\frac{1}{2} - \tilde{x}\right)$$

If $|\tilde{J}|$ is large enough, then electrolyte concentration will become zero at an electrode-electrolyte interface *approximately* at Sand's time [2] after which dendrites starts to grow rapidly

$$t_{\text{Sand}} = \frac{\pi D_{\text{app}}(z_0c_0F)^2}{4(Jt_a)^2} = \frac{\pi D_c(z_0c_0F)^2}{2J^2t_a}$$

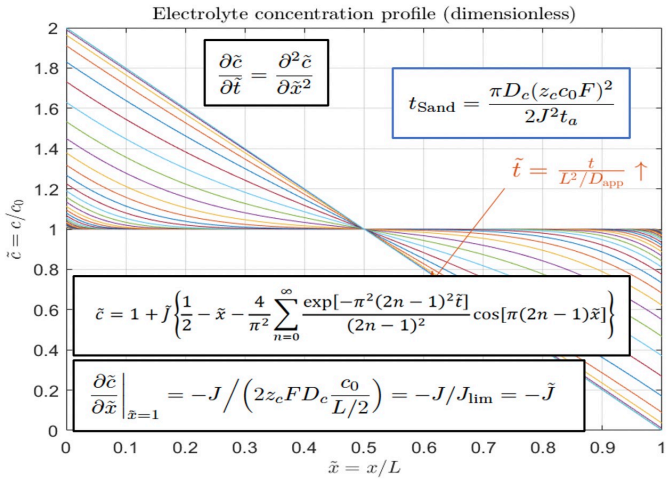

Figure 3-1 Summary of time evolution of electrolyte concentration.

If μ_a becomes smaller and μ_c remains unchanged, then D_a becomes smaller and D_c remains unchanged, then t_a becomes smaller and t_c becomes larger, then D_{app} becomes smaller. **[3]** In this way, the *negative* coefficients in exponential terms of $\tilde{c}$ becomes larger ($\tilde{J}$ remains unchanged) and t_{Sand} becomes larger. In other words, it takes longer time to either achieve stable

status (when $|\tilde{J}|$ is small) or deplete electrolyte at an electrode-electrolyte interface (when $|\tilde{J}|$ is large).

Table 3-1 List of variables/parameters.

Variable/Parameter	Unit	Meaning
z	1	Charge number
μ	$m^2 \cdot s^{-1} \cdot V^{-1}$	Electrochemical mobility
D	$m^2 \cdot s^{-1}$	Diffusion coefficient
t	1, or s	Ionic transference number, or time
c	$mol \cdot m^{-3}$	Electrolyte concentration
x	m	Coordinate
L	m	Distance between two electrodes
J	$C \cdot m^{-2} \cdot s^{-1}$	Applied current density

Table 3-2 List of subscripts.

Subscript	Meaning
a	Anion
c	Cation
$a$pp	Effective/apparent value
0	Initial value

As an introduction, this example about Sand's time [2] shows that ionic transference numbers could affect the development of concentration gradient of electrolyte solutions. A large Li+ transference number looks promising in inhibiting the fast development of electrolyte concentration gradient. It is natural to ask the following questions:

- How can ionic transference number be modified (improved) through material synthesis techniques? Moreover, what's the price? (Will other important properties be negatively affected?)

- In more complex (and close to real) systems, how does ionic transference numbers influence the development of electrolyte concentration gradients? Moreover, how is the significance?

- With inhibited electrolyte concentration gradients, what benefits could be expected in terms of performances for electrochemical devices?

3.1.2 MOF and inhibition of anion transport

As a promising class of nano-porous structure made of metal cornerstones and organic ligands, metal-organic frameworks (MOFs), have configurable structure and pore functionality. Thus, they can serve as scaffolds for channeling lithium ions while repelling anions.

There are many patterns of configured MOF additions in electrolytes/separators. Zhang et.al. [4] reported an electrolyte membrane with PVA network decorated by MOF particles. Shi et. al. [5] reported an electrolyte membrane with biomimetic channels for lithium ions made from MOF.

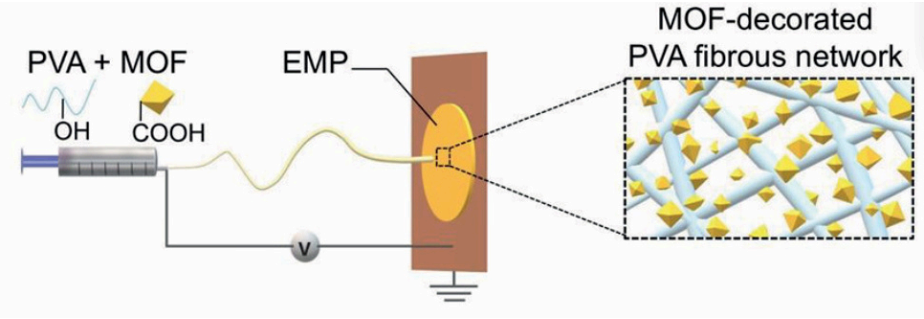

Figure 3-2 Scheme of MOF-decorate PVA network in a separator. [4]

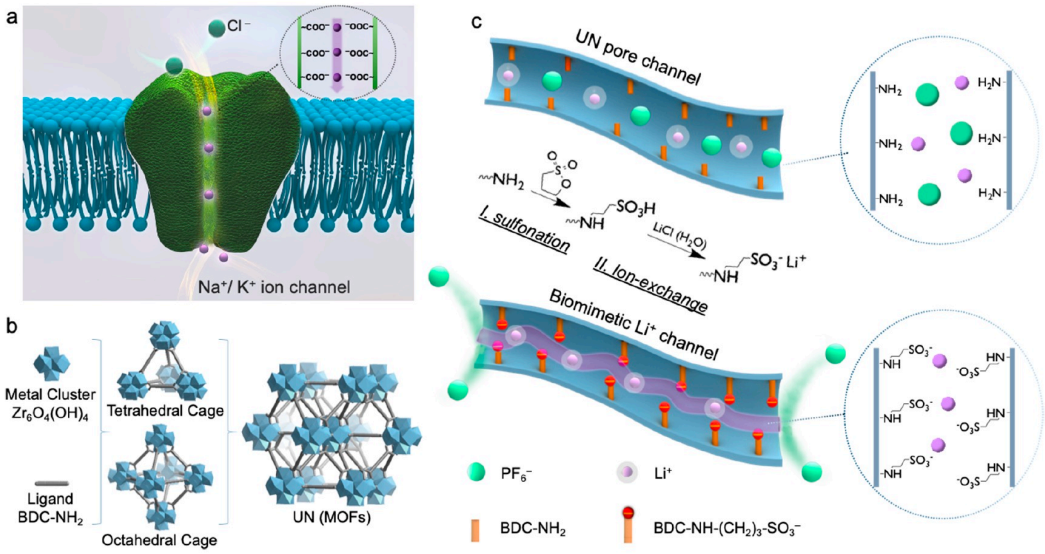

Figure 3-3 Scheme of Biomimetic Lithium-Ion Channels. [5]

3.2 Configuring geometries of MOF addition

A simple model with heterogeneous geometry of MOF distribution is used to discuss the transport of dilute electrolyte under applied electric field.

The basic layout is a rectangle pad (2D) immersed in electrolyte solutions, allowing the transport of dilute species including anions (usually Hexafluorophosphate, $PF6^-$) and cations (lithium ions, Li^+) in the solution.

As for boundary conditions, for electrostatics, the left end serves as an electric ground (0 V), while the right end is set 0.02 V potential. For transport of dilute species, the left end keeps 0 concentration of both species, while the right end keeps a fixed and equal concentration of both species (e.g., 1 mol/L). Additionally, electric isolation, no flux boundary conditions are needed for the remaining boundaries (e.g., up and down boundaries).

The model is simulated with COMSOL Multiphysics. When the calculation is finished, the stable distribution of total fluxes of cations and anions in the meshed pad are available and could be used to estimate ionic conductivity and transference number. Here is how they are estimated:

- The ratio of the integral of the total flux of cations to that of all ions is considered to be the average value of Li+ transference number;
- The integral of the total fluxes of all ions is considered to be proportional to the overall ionic conductivity of electrolyte solution under given material geometrical distributions.

Note that the current density in the electrolyte should be identical in any longitudinal cross section plane. In each plane, it is contributed proportionally by the fluxes of both cations and anions. It indicates that the ratio of current carried by cations to the overall current could vary in different cross sections during transport processes. Thus, to obtain the overall ratio of current carried by cations, it seems acceptable to aggregate all fluxes of cations and anions respectively, then their ratios to the sum stands for corresponding transference number.

Since the volume (area) of the simulated pad for transport of species applied external electric potential remains unchanged for various settings of material geometrical distributions, the integral of total fluxes of all species is proportional to the current density in the electrolyte solution. Moreover, since the applied external electric potential remains unchanged, the current density is proportional to the overall ionic conductivity of electrolyte solution under given material geometry. Therefore, the integral of the total fluxes of all species in the whole volume should be proportional to the overall ionic conductivity of electrolyte solution under given material geometrical distribution.

On the basis of the basic layout, different types of MOF particle add-ons are discussed with these issues: (1) pattern, (2) density and (3) location.

3.2.1 Geometrical pattern

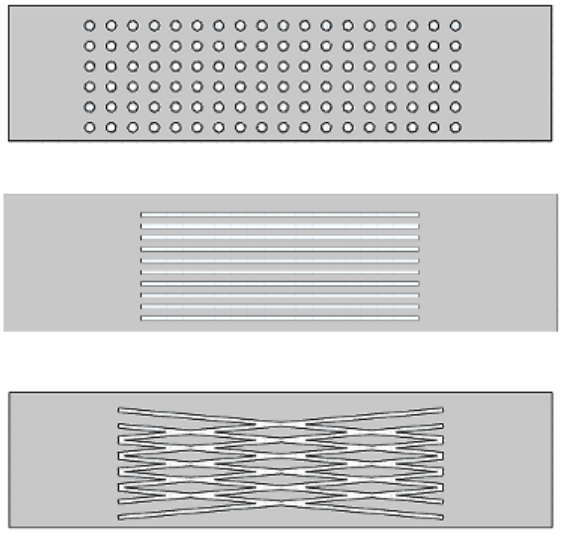

Figure 3-4 Patterns of MOF additions into a separator. (u) dots, (m) lines, (l) meshes.

As Figure 3-4 shows, there are 3 types of patterns of MOF additions being explored in this section:

- dots (particles disperse uniformly in space and do not contact with each other);
- lines (particles attached to structural lines, which do not intersect with each other);
- meshes (particles attached to structural lines, which interleave with each other and form a mesh).

Figure 3-5 shows simulation results. The colormaps indicates the ratio the total flux of cations to that of all ions (cation flux ratio): the warmer the color, the higher the ratio, the more total flux is contributed by cations locally.

In bulk regions, the cation flux ratio is close to the ratio of the diffusion coefficient of cations to the sum of the diffusion coefficients of both cations and anions. It is not surprised to see that in

regions occupied by MOF particles, the cation flux ratio is close to 1 as it is assumed that MOF particles are electrically isolate from cations.

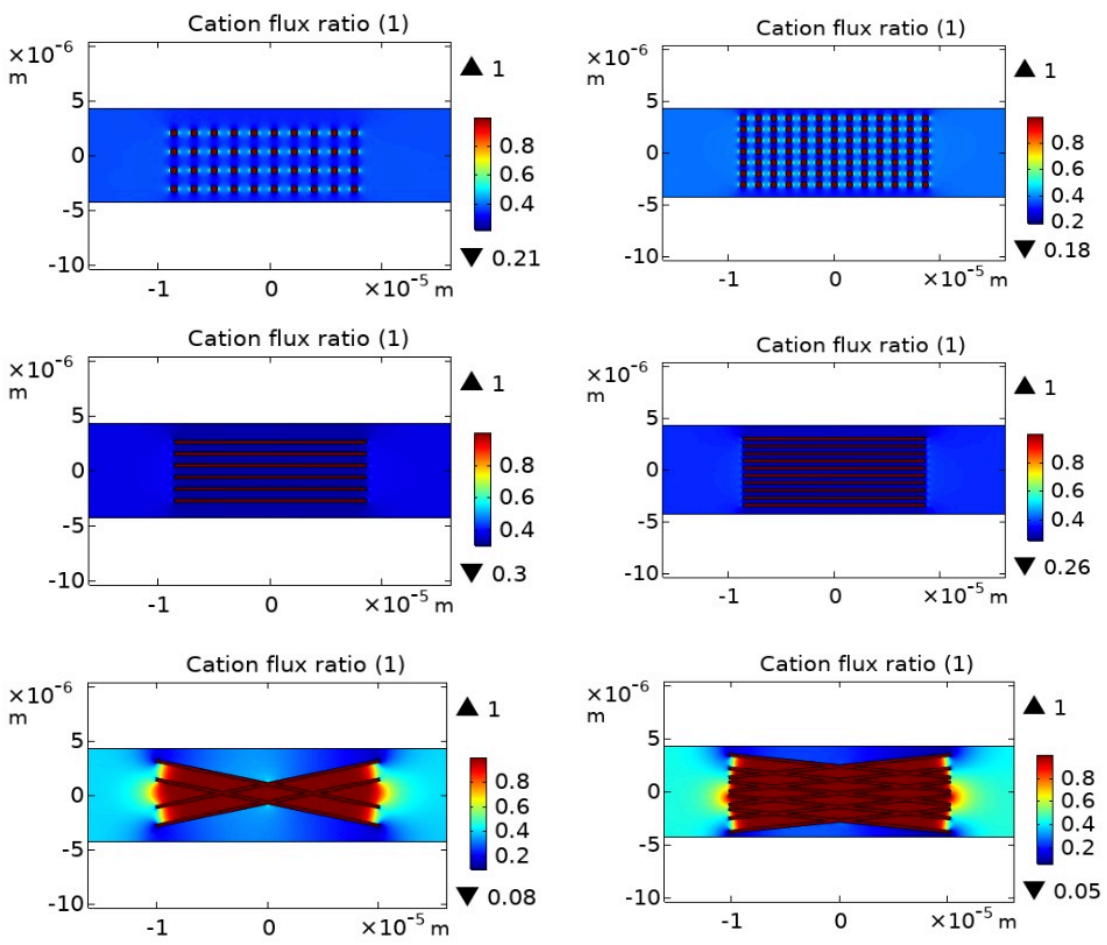

Figure 3-5 Distribution of cation flux ratio for different patterns of MOF additions. (u) dots, (m) lines, (l) meshes.

Interestingly, regions near MOF particles are kind of affected by these particles, and the resultant cation flux ratio takes an intermediate value between those of the bulk and MOF particles. More surprisingly, in the case of MOF attached to meshes, the inner regions surrounded by meshes seems to block the transport of anions, leaving a cation flux ratio close to 1.

Figure shows how the lithium ion transference number changes with the relative ionic conductivity of the electrolyte solution with configured material geometrical distributions. The

general tendency is lithium ion transference number increases as the relative ionic conductivity decreases. A possible explanation is that, due to the addition of MOF particles in configured material geometrical distributions, the total flux of anions in the overall cell is decreased, assume that the total flux of cations is unchanged (*or decreased with a smaller extend*), the integral of total fluxes of both ions is decreased, leading to an estimation of a decreased ionic conductivity; while the ratio of the integral of cation flux to that of all ions is increased, leading to an estimation of an increased lithium transference number.

From Figure 3-6, for patterns of dots and lines, with various amount of MOF additions, the variations of the ionic conductivity and lithium ion transference number are constrained in relatively small ranges, indicating that the transport of anions seems not being obviously influenced within the entire cell. In contrast, for the pattern of meshes, the two properties under discussion shows relatively large variations with different amount of additions, indicating that the transport of anions could be greatly affected cell-wisely. This difference might come from different affected regions: dots and lines only effects regions very close to themselves but have almost no influence on other regions; meshes can affect surrounded regions as well as close regions.

As a comment, this is a model in 2-dimensional space, while real batteries are objects in 3-dimensional space. The patterns discussed in 2d space might have not corresponding ones in real 3d space. For example, meshes in 2d space can completely block internal areas, while meshes in 3d space hardly block internal volumes. Thus, discussions here can just be a reference for some general observations but cannot be applied directly in physical practices.

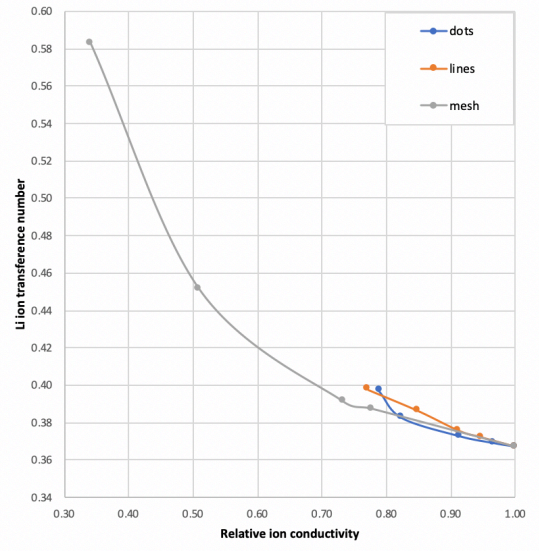

Figure 3-6 Ionic conductivity and lithium ion transference number for different patterns of MOF additions.

3.2.2 Spatial density

In this section, the density of particle addition and its effects are discussed. An alternative 2D layout is applied for discussions on the location of MOF additions.

For simplicity, only the pattern of dots is included. In order to be more realistic, 3D cases is also discussed in addition to 2D cases.

- 2D cases: dense, denser, most dense: hexagonal packing (like a honeycomb)

- 3D cases: dense, denser, most dense: face-centered cubic (fcc, or cubic closed packed)

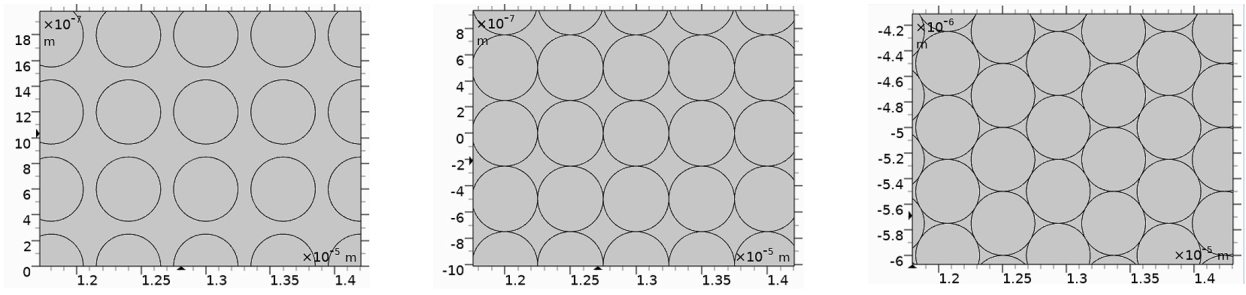

Figure 3-7 Different densities of MOF additions (dots pattern, 2D).

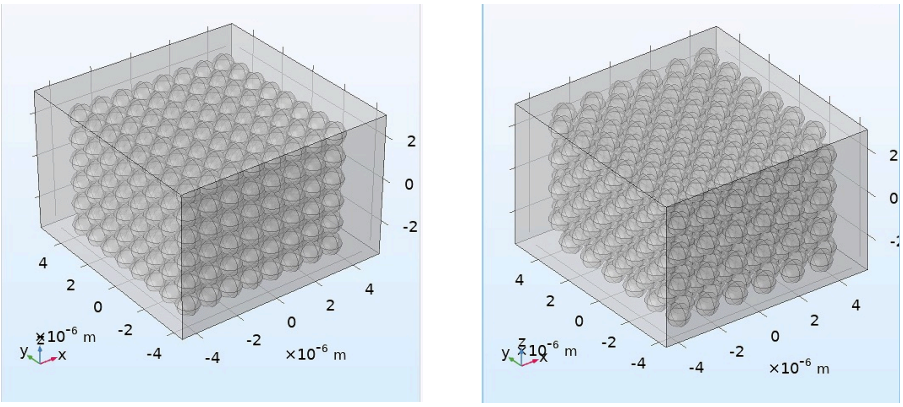

Figure 3-8 Different densities of MOF additions (dots pattern, 3D).

Figure 3-9 briefly summarizes the influences of dot density and addition locations on ionic conductivity and lithium ion transference number in the case of 2D geometries. Denote the reference case with 100% relative ion conductivity and 0.33 lithium ion transference number. Intuitively, the denser the addition of MOF particles, the more changes on the ionic conductivity and the lithium transference number.

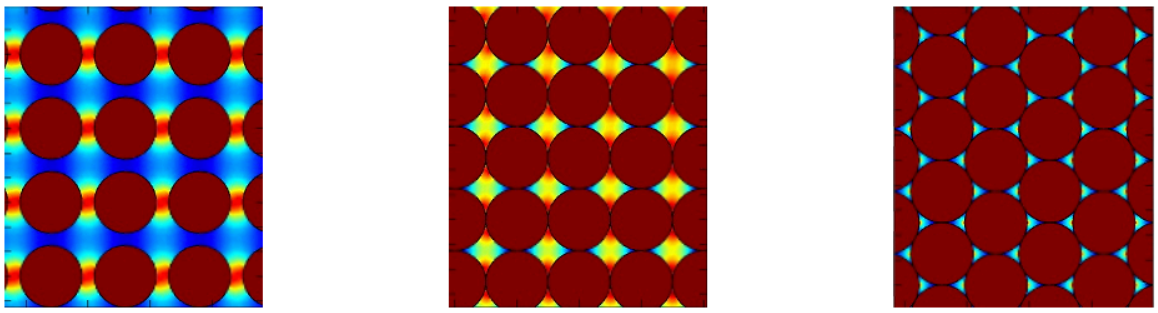

Figure 3-9 Distribution of cation flux ratio for different densities of MOF additions (dots pattern, 2D).

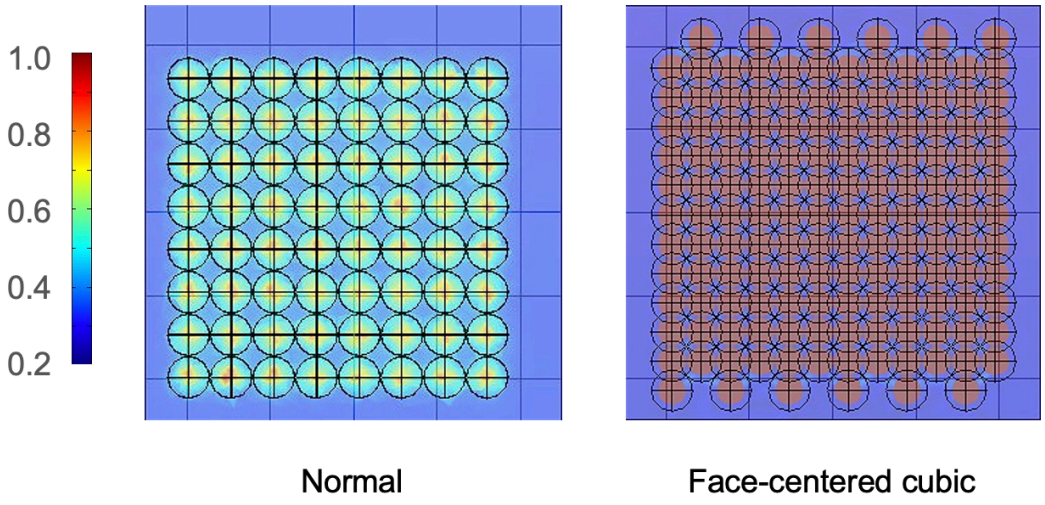

Figure 3-10 Distribution of cation flux ratio for different densities of MOF additions (dots pattern, 3D).

Figure 3-11 shows an ionic conductivity-lithium ion transference number plot for different densities of MOF additions (dots pattern, 2D scenario). However, even though the particles placed head by head according to the most dense packing, the resulting estimated lithium transference number is still below the value measured by physical experiments. Possible reasons might be:

- volume ratios of different materials are not exactly estimated, which might result in under estimation on the effects of particle addition to the cell;
- boundary conditions are different from physical experiments. Here Dirichlet boundary conditions about electrolyte concentration are set at electrodes; while in experiments Neumann boundary conditions about cation flux (electrochemical reaction) are set at electrodes.

3.2.3 Location within a cell

In this section, an alternative 2D layout is applied for discussions on the location of MOF additions. In the middle of the layout, there are insulating pillars (white) to mimic real separators

in electrochemical cells. These pillars, insulating for ion transport, reduce the liquid-wise volume ratio for electrolyte solution. There are 3 options to add MOF particles:

- between the separator and the anode,

- between the separator and the cathode,

- all the above (both gaps).

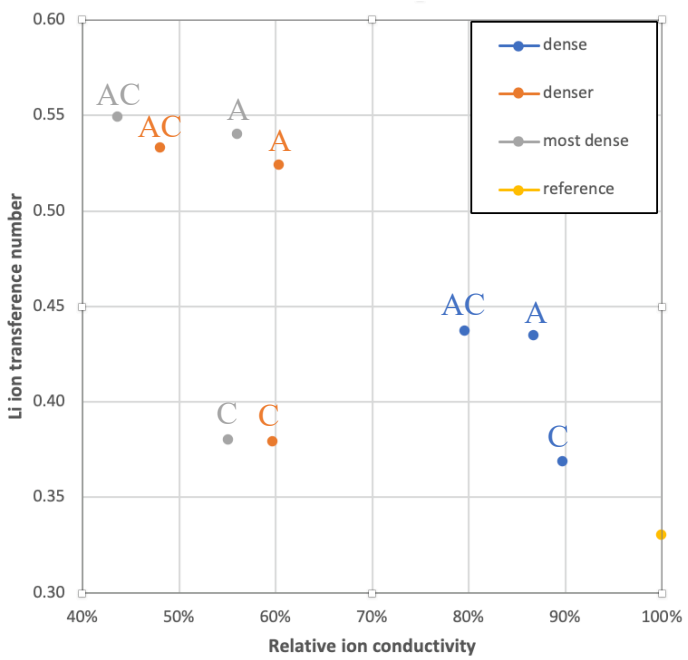

Figure 3-11 Ionic conductivity and lithium ion transference number for different densities of MOF additions (dots pattern, 2D). Positions of additions: (A): anode/separator, (C): cathode/separator, (AC): both anode/separator and cathode/separator.

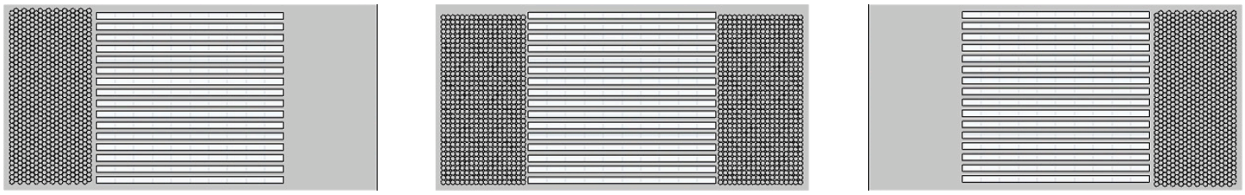

Figure 3-12 Different positions of MOF additions in a cell. (left) anode/separator, (middle) both anode/separator and cathode/separator, (right) cathode/separator.

As discussed before, addition of MOF particles helps increase the lithium ion transference number while decreases the ionic conductivity of the electrolyte solution in the configured material geometry. All 3 options of adding locations are consistent with this observation. Furthermore, the way of adding particles between the separator and the cathode has relatively small influence on changing the ionic conductivity and transference number, while adding particles to both gaps between the separator and the electrodes has relatively large influence on change these two physical properties of the cell. And the influence of adding particles between the separator and the anode has “mediocre” influences: the reduction of ionic conductivity is similar to the case of addition between the separator and the cathode (relatively small), while the enhancement of lithium ion transference number is similar the case of addition to both gaps (relatively large). Thus, it looks like the combination “the best of both worlds”: on one hand, lithium ion transference number is improved to reduce concentration polarization, while the harm to ionic conductivity is not very large so that ohmic polarization might not increase too much.

In physical experiments, the actual addition of MOF particles is placed between the separator and the anode. From the results of above simulations, it might partially explain the rationality of this operation besides issues like manufactory difficulties and economic costs.

3.3 Rate performance

In the section, we discuss the rate performances of different lithium-ion battery cells with or without addition of MOF with the means of mathematical simulations. Thus, models applied for simulations are introduced, followed by results and discussion.

3.3.1 Modeling

We first introduce the classic Doyle-Fuller-Newman (DFN) pseudo two-dimension (P2D) model and then single particle model (SPM). Before moving forward with simulation results for rate performance, some simple cases (e.g., mass transfer within a single separator, discharge termination due to electrolyte depletion) are discussed.

3.3.1.1 Doyle-Fuller-Newman P2D model

Here we apply pseudo two-dimension model (developed by Doyle, Fuller, Newman and co-workers) with COMSOL for discussing rate performances (based on parameters from physical experiments). [6] Two types of half cells of lithium ion batteries are discussed here: one is LFP (cathode)/Li (anode), the other is Li (cathode)/graphite (anode). Both of them are assembled as coin cells and tested under constant applied densities.

In model setup, a coin cell of lithium ion battery consists of the positive electrode (cathode), the separator, the negative electrode (anode) and current collectors. In this model, we consider an isothermal scenario without discussing energy balance. Note that the anode here is a lithium foil (can be seen as a 2D electrode surface), while the cathode here is a porous electrode with coexisting solid and liquid phases.

The material balance of electrolyte in the liquid phase is described as (e1) for the (positive) electrode and (e1') for the separator, respectively. At both ends of the cell, there is no mass flux (b1); at the electrode/separator interface, the concentration of the electrolyte and its mass flux are both continuous (b1', b1'').

The material balance of Lithium ions in a particle of active material in the solid phase is governed by Fick's second law with spherical coordinates as (e2). At the center of the particle, there is no mass flux (b2); on the surface of the particle, the mass flux is equal to the pore wall flux for electrode reactions (b2'). Since the anode here is an electrode surface instead of a porous electrode, the equation of particle intercalation is not applicable (e2), but the pore wall flux for electrode reactions still applies.

The charge balance in the liquid phase governed by Ohm's law is described as (e3) for the (positive) electrode and (e3') for the separator, respectively. At both ends of the cell, there is no charge flux; at the electrode/separator interface, the electrolyte potential and its charge flux are both continuous (b3', b3'').

The charge balance in the solid phase governed by Ohm's law is described as (e4). At the electrode/current collector interface, the charge flux is equal to the applied current density (b4); at the electrode/separator interface, the charge flux is 0 (b4'); at the current collector/negative electrode interface, the solid potential is set to be 0 (b4'').

Moreover, the pore wall flux, equal to the consuming/producing rate of Li ions due to the electrochemical reaction at the solid/electrolyte interface, is given by Butler-Volmer equation (e5). And the over potential of electrochemical reactions at the solid electrolyte interface is given by (e6) as a function of the solid potential, the electrolyte potential and the thermodynamic equilibrium potential of active material.

For active materials of electrodes [11], how open circuit voltage (OCV) changes with state of charge (SOC) is displayed in Figure. As a general tendency, as SOC changes from 0 to a small value, there is a steep drop of OCV. Then, as SOC transit to a large value, OCV stays stable with

little drop (plateau). Finally, as SOC becomes close to 1, there is another steep drop of OCV. Cathode materials have a higher plateau OCV than those of anode materials.

The ionic conductivity of electrolyte solution [12] is a function of electrolyte concentration and temperature. Figure shows how ionic conductivity changes with electrolyte concentration (under a constant temperature 298 K). At electrolyte concentration ~1000 mol/m^3, the ionic conductivity achieves its peak value. As the concentration becomes larger or smaller, the ionic conductivity decreases.

Moreover, in terms of diffusion coefficient of lithium ions (denoted as D) as a function of electrolyte (e.g., $LiPF_6$) concentration for different temperatures, Figure 3-14 shows a general tendency [13] that the diffusion coefficient decreases as the electrolyte concentration increases, while increases as the temperature increases.

Additionally, with some fitting approaches, the following formula [7] provides a way to estimate empirically the effective diffusion coefficient,

$$\boldsymbol{D}_{\mathbf{eff},i} = \epsilon_i^{\mathrm{brugg_i}} \times 10^{-4} \times 10^{-4.43 - \frac{54}{T(x,t)-229-5\times10^{-3}c_e(x,t)} - 0.22\times10^{-3}c_e(x,t)}$$

where D_{eff} is effective diffusion coefficient taking into account porosity and tortuosity, ε is porosity, brugg is Bruggeman coefficient, c_e is electrolyte concentration, T is temperature.

As for the rate constant for electrochemical reactions (denoted as k), it is also a function of temperature. Take the reaction at a negative electrode with graphite as active material for example. Figure 3-15 shows a fitting of the plots of ln (k) vs 1/T, which obey Arrhenius law [14] with high (linear) regression coefficients for different types of battery cells, where K is rate constant for the electrochemical reaction at the electrode, T is temperature.

Table 3-3 DFN P2D model governing equations and boundary conditions. [7]

Governing equations	Boundary conditions
Positive electrode, $i \in \{p, n\}$	
$\epsilon_i \frac{\partial c_e(x,t)}{\partial t} = \frac{\partial}{\partial x}\left[\boldsymbol{D}_{\mathbf{eff},i} \frac{\partial c_e(x,t)}{\partial x}\right] + a_i(1-t_+)j(x,t)$ (e1)	$-D_{\mathbf{eff},i} \frac{\partial c_e(x,t)}{\partial x}\Big\|_{x=0,\ L_n+L_p} = 0$ (b1)
	$c_e(x,t)\Big\|_{x=L_n^-} = c_e(x,t)\Big\|_{x=L_s^+}$ (b1')
$\frac{\partial c_{s,i}(x,r,t)}{\partial t} = D_{s,i} \frac{1}{r^2} \frac{\partial}{\partial r}\left(r^2 \frac{\partial c_{s,i}(x,r,t)}{\partial r}\right)$ (e2)	$-D_{s,i} \frac{\partial c_{s,i}(x,r,t)}{\partial r}\Big\|_{r=0} = 0$ (b2)
	$-D_{s,i} \frac{\partial c_{s,i}(x,r,t)}{\partial r}\Big\|_{r=R_{s,i}} = j(x,t)$ (b2')
$a_i F j(x,t) = -\frac{\partial}{\partial x}[\boldsymbol{\kappa}_{\mathbf{eff},i} \frac{\partial \Phi_e(x,t)}{\partial x}] + \frac{\partial}{\partial x}[\boldsymbol{\kappa}_{\mathbf{eff},i} \Upsilon T(x,t) \frac{\partial \ln c_e(x,t)}{\partial x}]$ (e3)	$-\boldsymbol{\kappa}_{\mathbf{eff},i} \frac{\partial \Phi_e(x,t)}{\partial x}\Big\|_{x=0,\ L_n+L_p} = 0$ (b3)
	$\Phi_e(x,t)\Big\|_{x=L_n^-} = \Phi_e(x,t)\Big\|_{x=L_s^+}$ (b3')
$\frac{\partial}{\partial x}[\sigma_{\mathbf{eff},i} \frac{\partial \Phi_s(x,t)}{\partial x}] = a_i F j(x,t)$ (e4)	$-\sigma_{\mathbf{eff},i} \frac{\partial \Phi_s(x,t)}{\partial x}\Big\|_{x=L_n+L_p} = I_{app}(t)$ (b4)
	$-\sigma_{\mathbf{eff},i} \frac{\partial \Phi_s(x,t)}{\partial x}\Big\|_{x=L_n} = 0$ (b4')
	$\Phi_s(x,t)\Big\|_{x=0} = 0$ (b4")
$j(x,t) = 2k_{\mathbf{eff},i}\sqrt{c_e(x,t)(c_{s,i}^{\max} - c_s^*(x,t))c_s^*(x,t)} \sinh[\frac{0.5R}{FT(x,t)}\eta_i(x,t)]$ (e5)	
$\eta_i(x,t) = \Phi_s(x,t) - \Phi_e(x,t) - \mathbf{U}_i$ (e6)	
Separator, $i = s$	
$\epsilon_i \frac{\partial c_e(x,t)}{\partial t} = \frac{\partial}{\partial x}\left[\boldsymbol{D}_{\mathbf{eff},i} \frac{\partial c_e(x,t)}{\partial x}\right]$ (e1')	$-D_{\mathbf{eff},s} \frac{\partial c_e(x,t)}{\partial x}\Big\|_{x=L_n^-} = -D_{\mathbf{eff},p} \frac{\partial c_e(x,t)}{\partial x}\Big\|_{x=L_s^+}$ (b1")
$0 = -\frac{\partial}{\partial x}[\boldsymbol{\kappa}_{\mathbf{eff},i} \frac{\partial \Phi_e(x,t)}{\partial x}] + \frac{\partial}{\partial x}[\boldsymbol{\kappa}_{\mathbf{eff},i} T(x,t) \Upsilon \frac{\partial \ln c_e(x,t)}{\partial x}]$ (e3')	$-\boldsymbol{\kappa}_{\mathbf{eff},s} \frac{\partial \Phi_e(x,t)}{\partial x}\Big\|_{x=L_n^-} = -\boldsymbol{\kappa}_{\mathbf{eff},p} \frac{\partial \Phi_e(x,t)}{\partial x}\Big\|_{x=L_p^+}$ (b3")

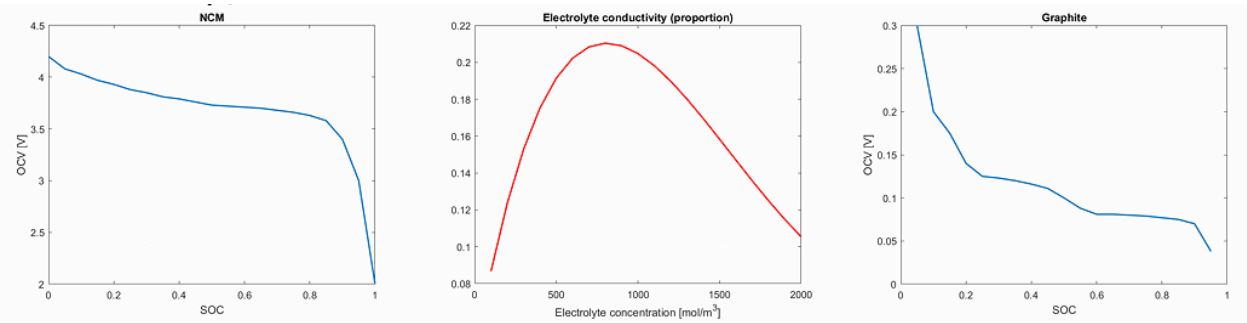

Figure 3-13 Some physical properties of some common electrode and electrolyte materials. [8][9][10]

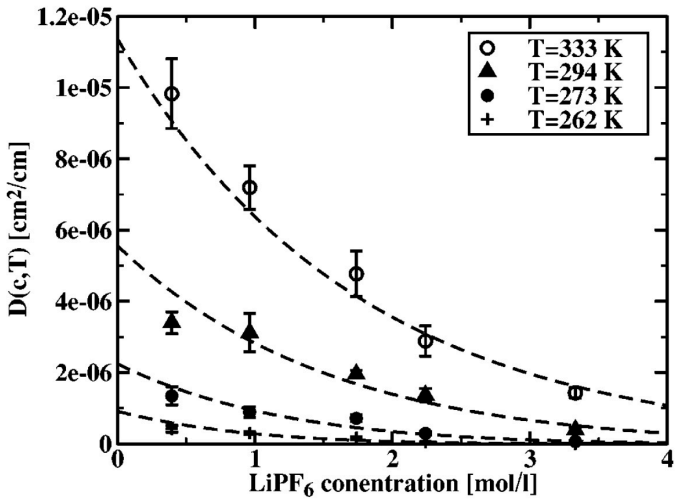

Figure 3-14 Variation of li ion diffusion coefficient with different electrolyte concentration and temperature. [13]

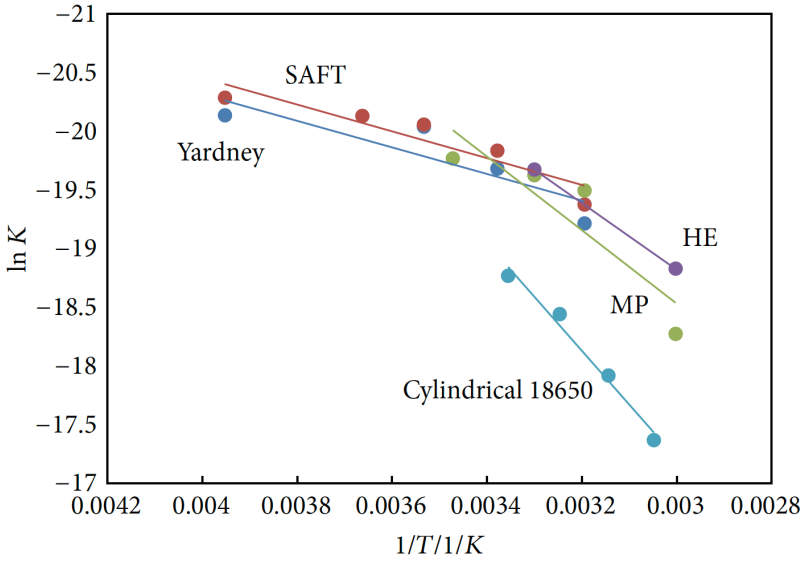

Figure 3-15 Variation of electrochemical reaction rate constant with temperature for different battery cell types. [14]

3.3.1.2 SPM model

To derive single particle model, the following assumptions [11] are proposed:

1. The Lithium concentration in solid phase is constant in space, uniformly in time.

2. The exchange current density can be approximated by its averaged value, which is independent of space.

3. The total amount of lithium in the electrolyte and that in the solid phase are conserved. Note that 1 and 3 make it possible to express the fluxes proportional to current.

4. The anodic charge transfer coefficient is equal to the cathodic charge transfer coefficient.

In SPM model, the output voltage of a battery cell can be approximated by the following equation [11]

$$\begin{aligned} V(t) = & \frac{\mathrm{RT}}{\alpha F}\sinh^{-1}\left(\frac{-I(t)}{2a^{+}L^{+}\bar{i}_0^{+}(t)}\right) \\ & -\frac{\mathrm{RT}}{\alpha F}\sinh^{-1}\left(\frac{I(t)}{2a^{-}L^{-}\bar{i}_0^{-}(t)}\right) \\ & +U^{+}\left(\bar{c}_{\mathrm{ss}}^{+}(t)\right)-U^{-}\left(\bar{c}_{\mathrm{ss}}^{-}(t)\right)-\left(\frac{R_f^{+}}{a^{+}L^{+}}+\frac{R_f^{-}}{a^{-}L^{-}}\right)I(t) \\ & +\frac{L^{+}+2L^{\mathrm{sep}}+L^{-}}{2\overline{\kappa}}I(t) \\ & +k_{\mathrm{conc}}(t)[\ln c_e(0^{+},t)-\ln c_e(0^{-},t)] \end{aligned}$$

As indicated by the approximation for output voltage of an electrochemical cell, processes at solid-electrolyte interface, in solid face and in electrolyte phase are all included. The section mainly focuses on processes in electrolyte phase, which are relevant to ionic fluxes and diffusional migrations. The voltage drop contributed by ionic fluxes is inverse proportional to the average ionic conductivity of electrolyte solution, while the voltage drop led by diffusional migration is proportional to the natural logarithm of the quotients of electrolyte concentrations at the two ends of the electrochemical cell.

3.3.1.3 Discussion

At first, consider an imaginary electrochemical cell with only a separator:

- consider infinitely fast electrochemical reactions at the solid-electrolyte interface;

- assume the fluxes is constant with respect to location;

- the main focus is processes occurring in the electrolyte.

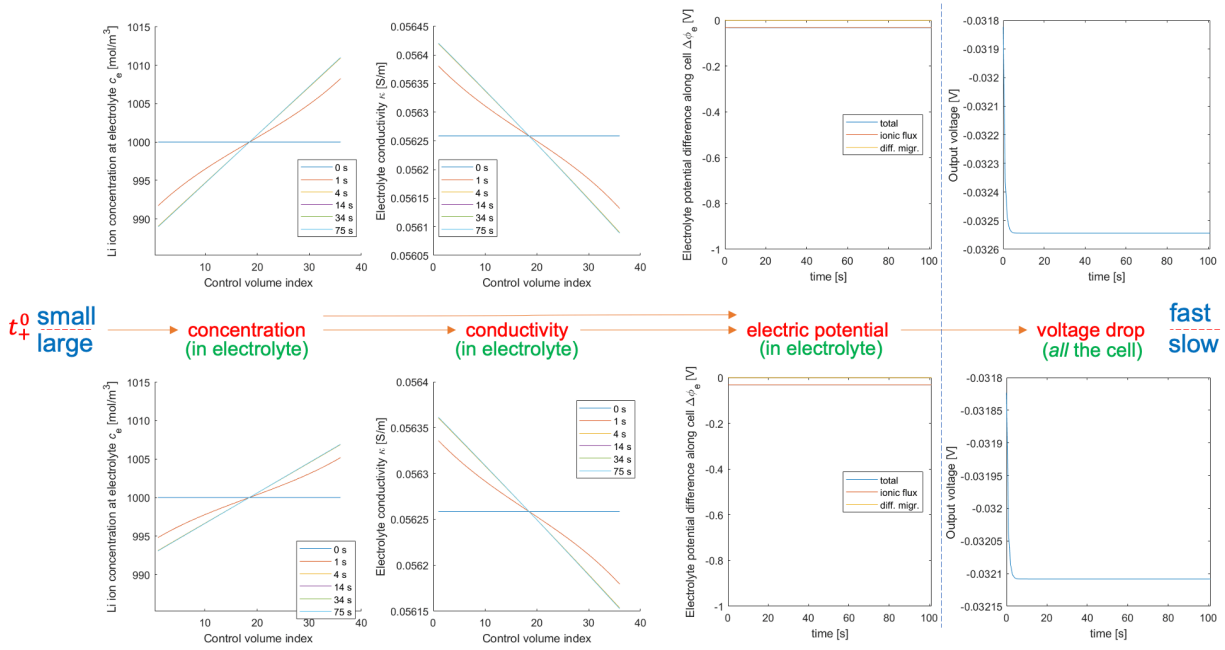

Figure 3-16 Temporal evolution of properties when a separator is discharged. (up) small lithium ion transference number, (low) large lithium ion transference number.

As a chain of reasoning, the value of lithium ion transference number can affect the concentration distribution of ions in the electrolyte solution, which affects ionic conductivity of the electrolyte in different spatial locations. For electric potential associated with processes in the electrolyte, electrolyte concentration gradient affects the term for diffusional migration, while the change in electrolyte ionic conductivity affects the term relevant to ionic fluxes. However, from

simulation results, the variation of lithium transference number has little influence on the change of electric potential and output voltage drop. The reason seems to be there is no large concentration gradient across the separator even at stable states.

For the simple case of applying current on a separator, there is some discussion on how lithium ion transference number as well as properties of a separator (e.g., length and porosity) affect the time for the separator to reach a stable state (transition time) and the value of voltage drop relevant to diffusional migration (diffusional migration voltage drop).

As general, the higher the lithium ion transference number, the shorter the transient time and the smaller the diffusional migration voltage drop. It is intuitive that with a high lithium ion transference number, a higher portion of lithium ions will be transferred from the negative electrode side to the positive electrode side, which achieves a balance with the driving force to build up electrolyte concentration gradient (e.g., electrochemical reactions consuming/producing species in electrolyte solution) faster and thus qualify the magnitude of the ultimate built-up concentration gradient. in this way, the diffusional migration voltage drop is also reduced because of smaller electrolyte concentration gradient.

As the porosity for liquid in a separator increases, the transition time decreases, and the magnitude of diffusional migration voltage drop also decreases. It seems reasonable to account to effective medium approximations for this change: with higher separator porosity, there is higher effective ionic diffusion coefficient / conductivity for electrolyte transported with the separator, which fastens the transport of electrolyte species to fight again the building up of electrolyte concentration gradient. Thus, similar to having a high lithium ion transference number, the transition for reaching stable states is shortened and the diffusional migration voltage drop is reduced.

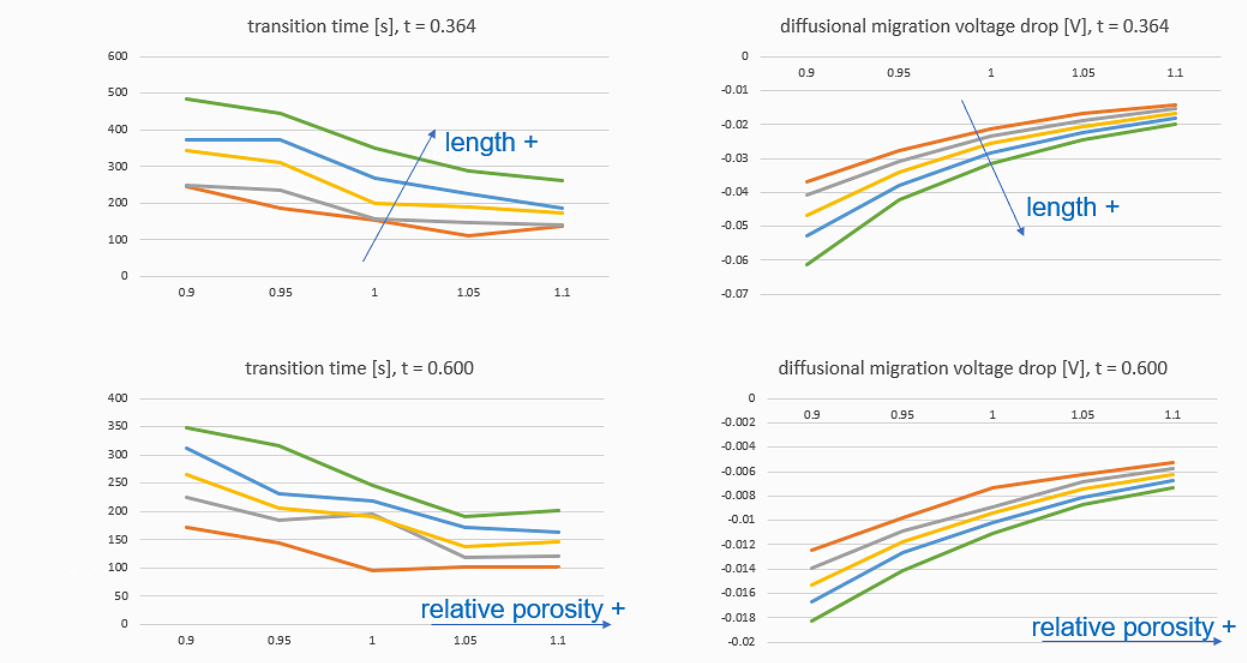

Figure 3-17 Influences of lithium ion transference number, separator length and porosity on transition time and diffusional migration voltage drop for the case of discharging a separator.

As the length of the separator increases, the transition time increases, and the magnitude of diffusional migration voltage drop also increases. A possible explanation is, the cost for counterbalancing the electrolyte concentration gradient becomes higher as there is longer way and takes more time for electrolyte species to be transported through the separator.

In a nutshell, a high lithium ion transference number and a high separator porosity are both beneficial for reducing transition time and diffusional migration voltage drop. However, a long separator length brings in large transition time and diffusional migration voltage drop.

If we imagine a large concentration gradient of electrolyte solution along the cell, then the average ionic conductivity of electrolyte is decreased (assume that the initial electrolyte concentration is close to the concentration corresponding to highest ionic conductivity; according to the "bell" shape of the ionic conductivity – electrolyte concentration plot, the more deviation from this concentration, the more decrease of the ionic conductivity.) On the other hand, it seems

obvious that the difference between the electrolyte concentrations at both ends of the electrochemical cell becomes larger, so does the logarithm of their quotients. In this way, both ionic fluxes and diffusional migration make larger contribution to the change of output voltage. Note that during charge stage, the contributions of ionic fluxes and diffusional migration are both positive, making increase of the output voltage. In contrast, during discharge stage, their contributions are both negative, making decrease of the output voltage. Thus, large concentration gradient of electrolyte solution could negatively impact both charge and discharge performances of an electrolyte cell.

Furthermore, from Figure 3-18, it seems that the magnitude of the contribution from ionic diffusional migration is more significant than that from ionic fluxes. Also, the variation for ionic diffusional migration is also more obvious to observe. However, mathematical derivation is needed for deeper insights on their relations. And it might be closely relevant to physiochemical properties of materials of the overall cell.

In order to show the effect of varying the value of lithium ion transference number, electrodes are introduced at both ends of the separator to invoke consumption/generation of lithium ions and bring in electrolyte concentration gradients.

As discussed, with higher lithium ion transference number, (1) the gradient of lithium ion concentration in electrolyte solution along the cell becomes smaller, and (2) the change of output voltage also becomes slower. The equation of electric potential of electrolyte phase is helpful for understanding their correlations: the smaller the gradient of electrolyte concentration along the cell, the less the electric potential of electrolyte phase varies, which inhibits the change of overall output voltage.

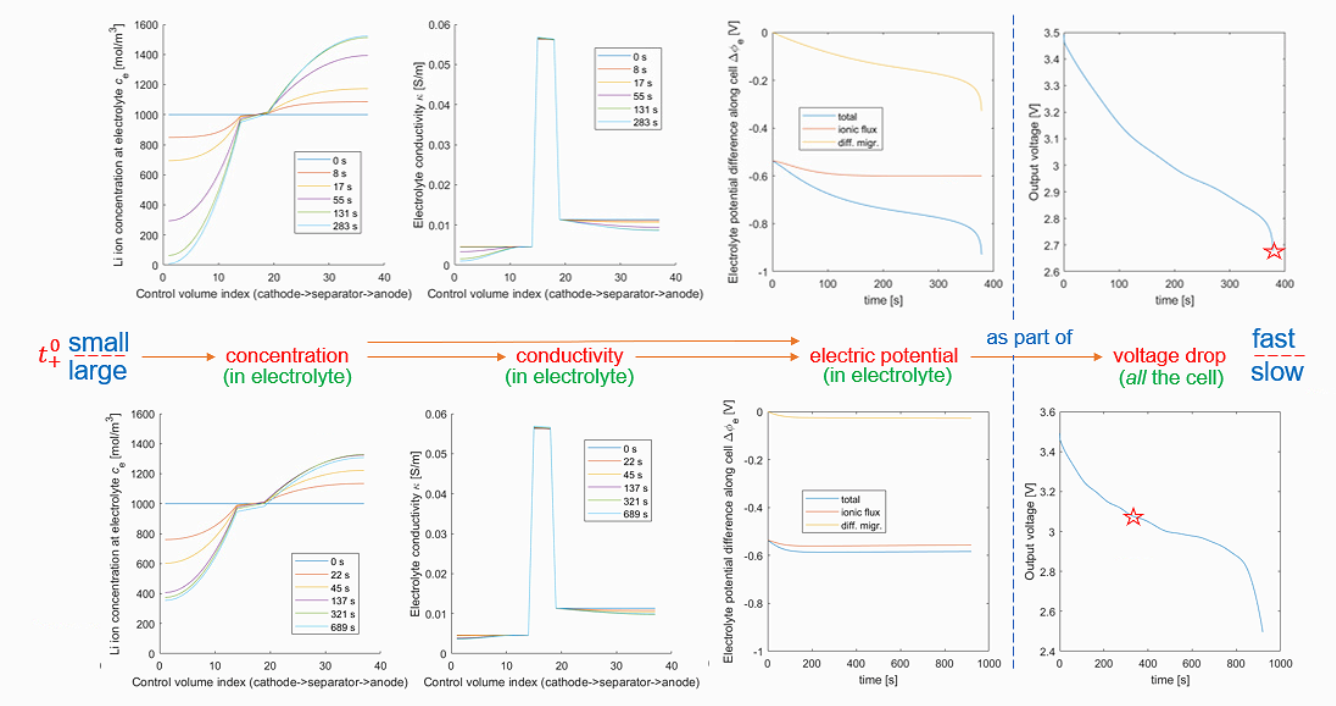

Figure 3-18 Temporal evolutions of properties when a full-cell is discharged. (up) small lithium ion transference number, (low) large lithium ion transference number.

As Figure 3-18 shows, thanks to high lithium ion transference number, there is smaller electrolyte concentration gradient along the cell as charging proceeds. Thus, as time goes by, the difference of electrolyte potential does not increase too much, and the change of output voltage is slowed down.

Moreover, due to optimization on code, more sample points could be investigated for exploring the relations among thickness of electrodes, discharge rate and capacity utilization.

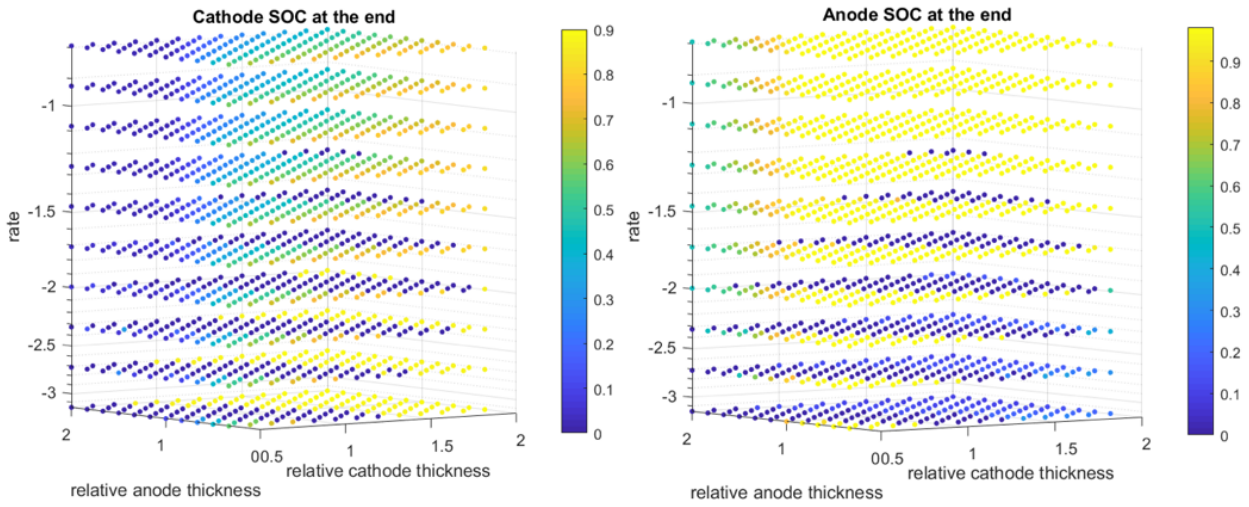

Figure 3-19 Cathode (left) and anode (right) state of charge at the end of constant-rate discharging for cell configurations with different electrode thickness under different discharging rates.

From Figure 3-19 it seems that, for cathode, generally speaking, thin cathode and small rate are good for the decrease of its SOC at the end of discharging. Similarly, thin anode and small rate are helpful for achieving high SOC of anode. These observations meet the 2d-plot in previous email.

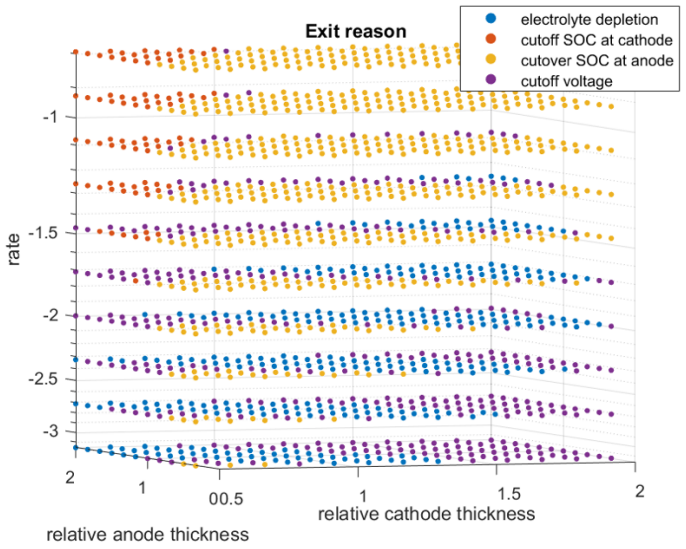

Figure 3-20 Exit reasons for cell configurations with different electrode thickness under different discharging rates.

And we also have a look at the reason for exiting discharge process. As Figure 3-20 shows, for small rates, the cell usually exits discharging stages because one of the electrodes reaches cutover (cutoff) SOC. In contrast, for large rates, the cell quits as results of low voltage and (or) electrolyte depletion. These results seem reasonable since at small rates the overpotential is small so the electrodes have enough time to allow electrochemical reactions occur sufficiently.

3.3.2 Results and Discussion

3.3.2.1 LFP/Li Half-Cell

Initially, the distribution of electrolyte species, lithium ions and anions such as hexafluorophosphate are distributed uniformly across the entire cell.

During discharging processes, lithium ions are consumed at the cathode while generated at the anode, forming a sink at the cathode and a source at the anode for lithium ions in electrolyte solution. The resulting electrolyte (lithium ion) concentration gradient of across the cell can serve as a driving force of the transport of lithium ions, while contributes to the change of electrolyte potential and thus cell output voltage at the same time. If the value of lithium transference number is high, then a large portion of lithium ions in the electrolyte solution are transported from the source at the anode to the sink at the cathode, greatly inhibiting the development of electrolyte concentration gradient. In this way, as discharging proceeds, the concentration gradient stabilizes at a relatively small magnitude, casting relatively small influence on the change of electrolyte potential and the decrease of cell output voltage. In contrast, if the lithium ion transference number is low, then the magnitude of established electrolyte concentration gradient will be relatively large, contributing to huge change of electrolyte potential and decrease of cell output voltage.

For charging processes, it is the anode that consume lithium ions and the cathode that generate lithium ions. However, the analysis is similar. Having a high lithium transference number inhibits the development of electrolyte concentration gradient by facilitating the transport of lithium ions through the cell, and thus brings small change of electrolyte potential and slow increase of cell output voltage.

Note that there is an underlying assumption that the concentration of cations and anions are equal in most regions of the cell (except for regions within the range of Debye length from electrodes).

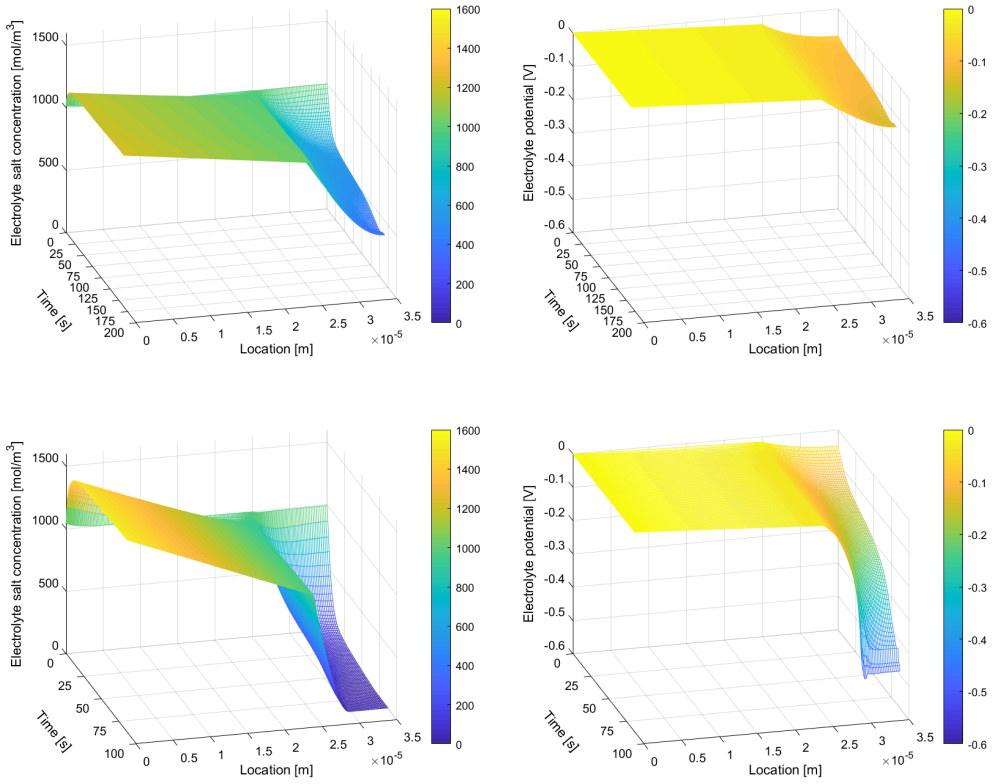

Figure 3-21 Temporal evolution for electrolyte salt concentration (left) and electrolyte potential (right) for experimental (up) and reference (low) groups of LFP/Li half-cells under 20 C constant-rate discharging.

Figure 3-21 compares temporal evolutions of the electrolyte concentration and the electrolyte potential of the experimental group with those of the reference group as LFP/Li cells under 20 C constant-rate discharging.

In the experiment group, thanks to high lithium ion transference number, the lowest electrolyte concentration at the cathode is about 0.4 M, while the highest electrolyte concentration at the anode is about 1.1 M, with an estimated electrolyte concentration gradient of 2e5 M/m. In contrast, in the reference group, due to low lithium ion transference number, the lowest electrolyte concentration at the cathode is about 0 M, while the highest electrolyte concentration at the anode is about 1.4 M, with an estimated electrolyte concentration gradient of 5e5 M/m.

At the first moment of discharging, the electrolyte potential at the cathode is about -0.10 V and -0.05 V for the experimental group and the reference group, respectively. Note that at the beginning there is lower electrolyte potential at the cathode for the experimental group. This is mainly because the electrolyte ionic conductivity of the experimental group is lower than that of the reference group. The ohmic polarization determined by electrolyte ionic conductivity occurs immediately at the beginning of discharging (or charging). As discharging proceeds, the electrolyte potential at the cathode size decreases. The lowest value for the experimental group is about -0.15 V, while the lowest value for the reference group is about -0.45 V. If the contribution of electrolyte ionic conductivity is excluded, then an approximate contribution made by electrolyte concentration gradient is -0.05 V and -0.40 V for the experimental group and the reference group, respectively.

The duration of the discharging process is about 200 and 100 seconds for the experimental group and the reference group, respectively. For the former, the termination of discharging is mainly

because the SOC of cathode material reaches the assigned threshold; for the latter, the termination is mainly because the output voltage reaches the assigned threshold.

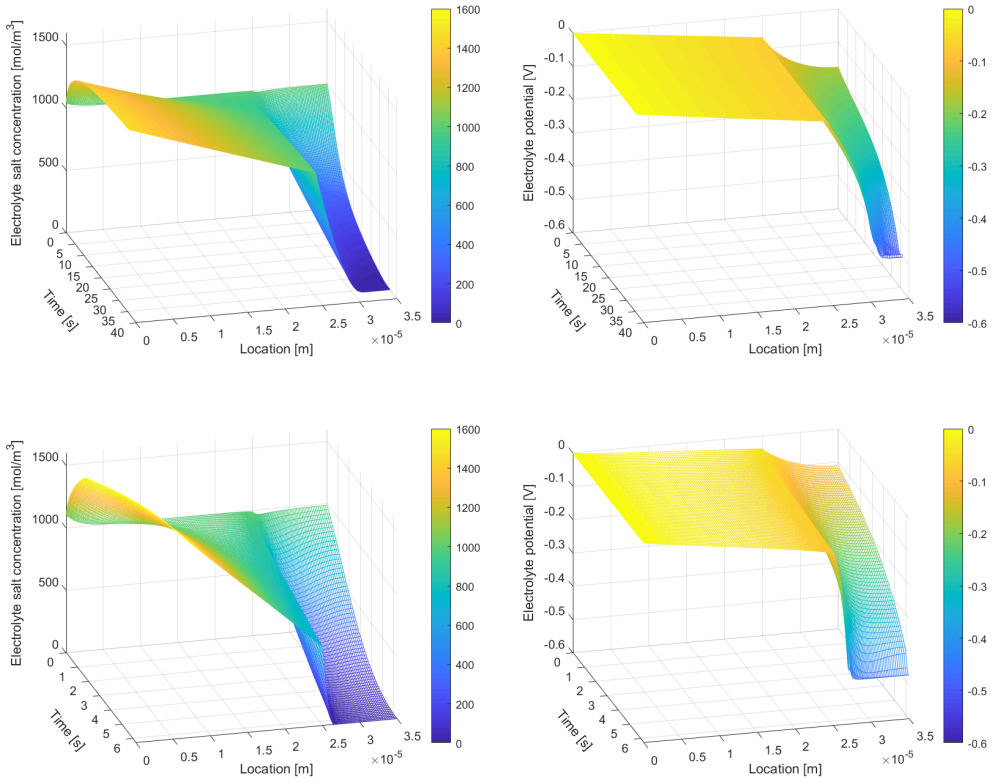

Figure 3-22 Temporal evolution for electrolyte salt concentration (left) and electrolyte potential (right) for experimental (up) and reference (low) groups of LFP/Li half-cells under 50 C constant-rate discharging.

Figure 3-22 compares temporal evolutions of the electrolyte concentration and the electrolyte potential of the experimental group with those of the reference group as LFP/Li cells under 50 C constant-rate discharging.

In both groups, the lowest electrolyte concentration at the cathode is about 0 M, and the estimated electrolyte concentration gradient is about 5e5 M/m. Because of different lithium transference number, it takes different time for each group to deplete electrolyte at the cathode: about 37 seconds for the experimental group and about 6 seconds for the reference group.

At the first moment of discharging, the electrolyte potential at the cathode is about -0.18 V and -0.11 V for the experimental group and the reference group, respectively. There is still lower electrolyte potential at the cathode for the experimental group because of relatively lower electrolyte ionic conductivity. Later on, as the cell keeps discharging, the electrolyte potential at the cathode size decreases. The lowest value for the experimental group is about -0.50 V, while the lowest value for the reference group is about -0.48 V. If the contribution of electrolyte ionic conductivity is excluded, then an approximate contribution made by electrolyte concentration gradient is -0.32 V and -0.37 V for the experimental group and the reference group, respectively. Although there is no huge difference between these two values, the difference brought by varying lithium ion transference number could be reflected by time: to reach a very low electrolyte potential at the cathode, it took about 37 seconds for the experimental group and about 6 seconds for the reference group.

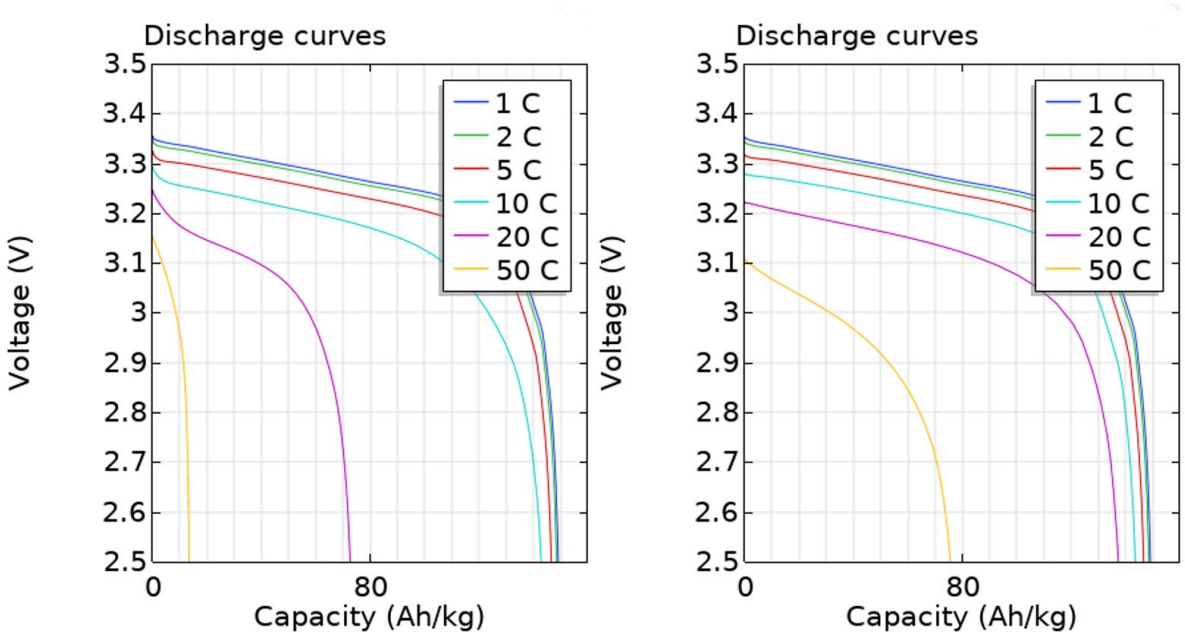

Figure 3-23 Discharge rate performances (capacity) for reference (left) and experimental (right) group of LFP/Li half-cells.

The durations for the discharging process are short for both groups. The major limiting issue should be electrolyte depletion and large change of electrolyte potential.

Figure 3-23 shows comparisons on discharge rate performances for the reference cell and the experimental cell. Note that the electrochemical cells adopt a structure with Li foil as anode and LFP as cathode material. The potential of Li is set as reference (0V), and the potential of LFP decreases as discharge proceeds.

As a general tendency, the output specific capacity of a cell decreases as discharge rate increases. For larger rates, the decrease "rate" of output capacity also becomes more severe. Given relatively small rates (1 ~ 5 C), the differences between the reference group and the experimental group are not obvious. However, at larger rates (10 ~ 50 C), the capacity drops of the reference group and those of the experimental group show a huge gap, indicating the relevant advantage of the experimental group in terms of output capacity at high discharge rates.

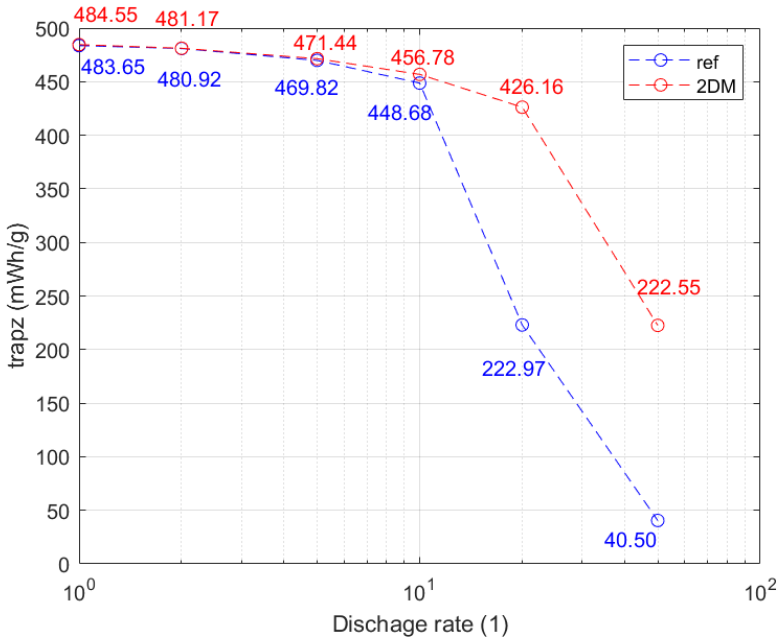

Figure 3-24 Discharge rate performances (energy) for reference and experimental groups of LFP/Li half-cells.

Figure 3-24 shows comparisons on specific output energy for the reference cell and the experimental cell (2DM). The data points are obtained by doing numerical integration over output voltage-discharge capacity plot of these electrochemical cells.

As a general tendency, the output specific energy of a cell decreases as discharge rate increases. For larger rates, the decrease "rate" of output energy also becomes larger. Given relatively small rates (1 ~ 10 C), the differences between the reference group and the experimental group are not obvious. However, at larger rates (> 10 C), the energy drops of the reference group and those of the experimental group show a huge gap, indicating the relevant advantage of the experimental group in terms of output energy at high discharge rates. However, discharging rates higher than 10 C should be uncommon in real life. From this viewpoint, this plot should have more theoretical meaning than practical usefulness.

3.3.2.2 Li/Graphite Half-Cell

Figure 3-25 compares temporal evolutions of the electrolyte concentration and the electrolyte potential of the experimental group with those of the reference group as Li/graphite cells under 1 C constant-rate discharging.

In the experiment group, thanks to high lithium ion transference number, the lowest electrolyte concentration at the cathode is about 0.6 M, while the highest electrolyte concentration at the anode is about 1.1 M, with an estimated electrolyte concentration gradient of 5.9e3 M/m. In contrast, in the reference group, due to low lithium ion transference number, the lowest electrolyte concentration at the cathode is about 0.4 M, while the highest electrolyte concentration at the anode is about 1.4 M, with an estimated electrolyte concentration gradient of 1.2e4 M/m.

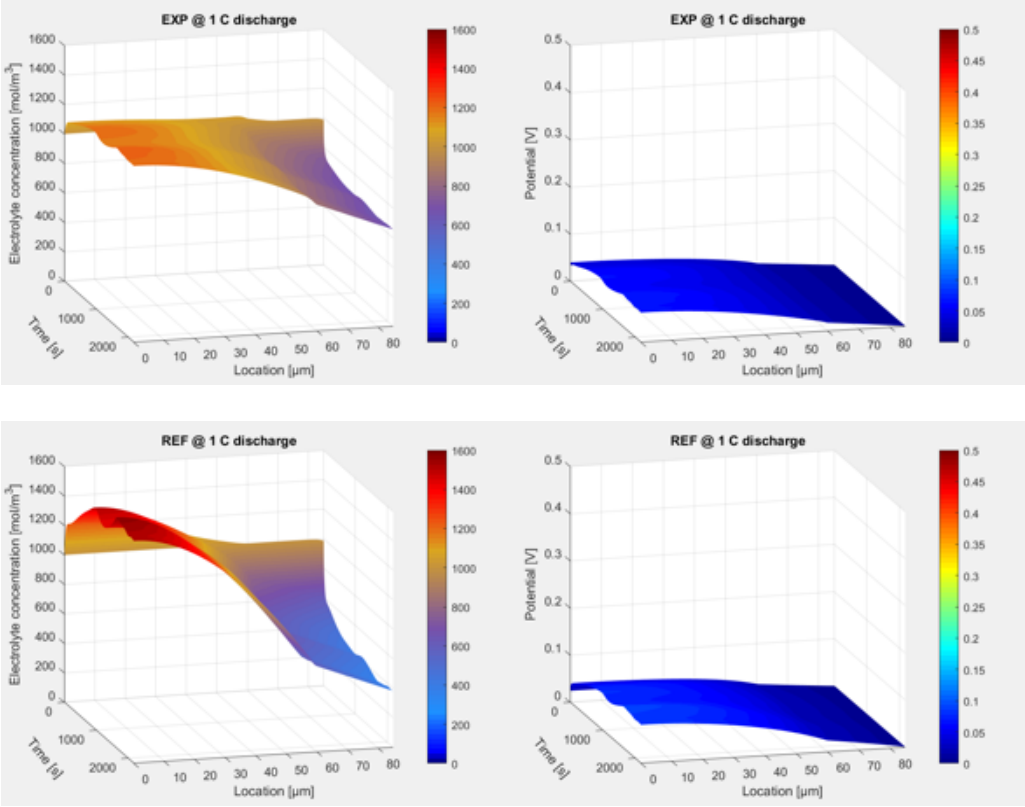

Figure 3-25 Temporal evolution for electrolyte salt concentration (left) and electrolyte potential (right) for experimental (up) and reference (low) groups of Li/graphite half-cells under 1 C constant-rate discharging.

At the first moment of discharging, the electrolyte potential at the anode is about 0.04 V and 0.03 V for the experimental group and the reference group, respectively. Note that at the beginning there is higher electrolyte potential at the anode for the experimental group due to lower electrolyte ionic conductivity. The main reason is that the experimental group has an electrolyte ionic concentration lower than the reference group. As the discharging stage proceeds, the electrolyte potential at the anode size increases. The highest value for the experimental group is about 0.08 V, while the lowest value for the reference group is about 0.09 V. If the contribution of electrolyte ionic conductivity is excluded, then an approximate contribution made by electrolyte concentration gradient is 0.04 V and 0.05 V for the experimental group and the reference group, respectively.

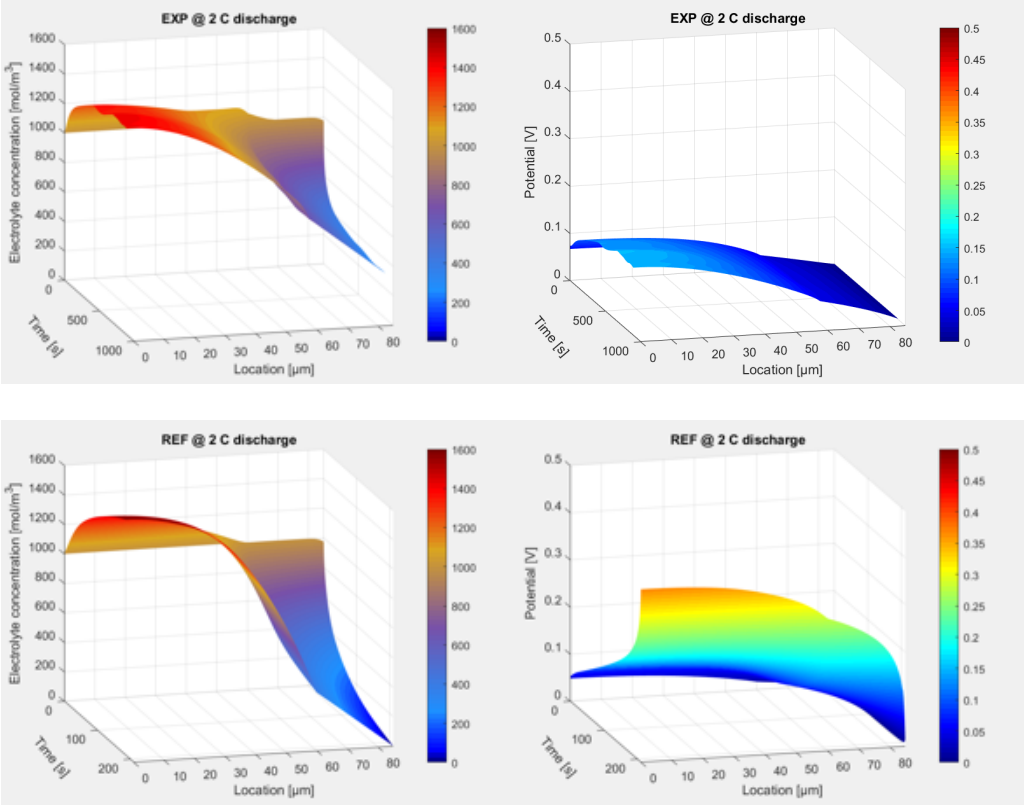

Figure 3-26 Temporal evolution for electrolyte salt concentration (left) and electrolyte potential (right) for experimental (up) and reference (low) groups of Li/graphite half-cells under 2 C constant-rate discharging.

The durations of the discharging process are about 2000 seconds for both the experimental group and the reference group, respectively. the termination of charging is mainly because the anode material reaches the assigned threshold of SOC. Although there is some difference between the electrolyte potentials of the two cell groups, it is not a limiting factor for energy utilization given a relatively small discharging rate.

Figure 3-26 compares temporal evolutions of the electrolyte concentration and the electrolyte potential of the experimental group with those of the reference group as LFP/Li cells under 2 C constant-rate discharging.

In the experiment group, thanks to high lithium ion transference number, the lowest electrolyte concentration at the cathode is about 0.3 M, while the highest electrolyte concentration at the anode is about 1.4 M, with an estimated electrolyte concentration gradient of 1.3e4 M/m. In contrast, in the reference group, due to low lithium ion transference number, the lowest electrolyte concentration at the cathode is about 0 M, while the highest electrolyte concentration at the anode is about 1.6 M, with an estimated electrolyte concentration gradient of 1.8e4 M/m. At the first moment of discharging, the electrolyte potential at the anode is about 0.08 V and 0.05 V for the experimental group and the reference group, respectively. The higher electrolyte potential at the anode for the experimental group could be viewed as a direct result of lower electrolyte ionic conductivity compared to the reference group. As discharging continues, the electrolyte potential at the anode size increases. The highest value for the experimental group is about 0.18 V, while the lowest value for the reference group is about 0.36 V. If the contribution of electrolyte ionic conductivity is excluded, then an approximate contribution made by electrolyte concentration gradient is 0.10 V and 0.31 V for the experimental group and the reference group, respectively.

The duration of the discharging process is about 1000 and 200 seconds for the experimental group and the reference group, respectively. For the experimental group, it is mainly the result of the SOC of anode material reaches the predefined threshold; for the reference group, it mainly results from the output voltage reaching the assigned cutoff value.

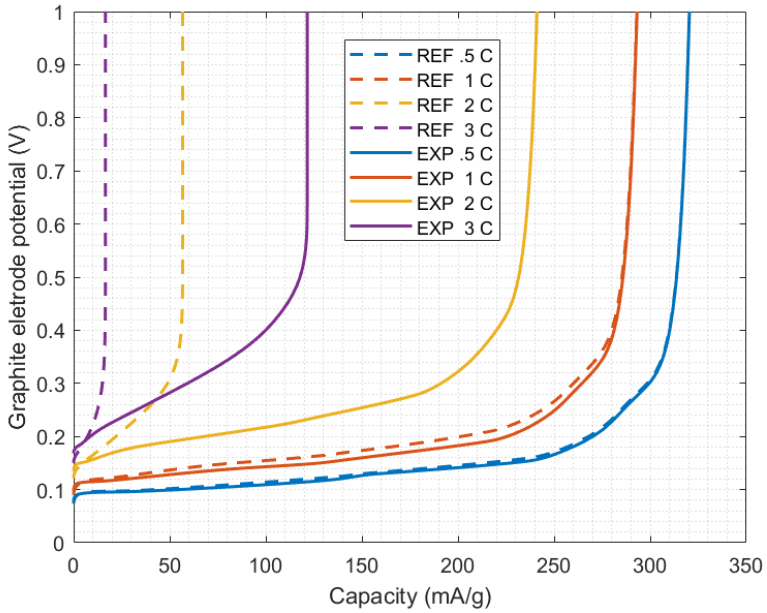

Figure 3-27 Discharge rate performances (capacity) for reference and experimental groups of Li/graphite half-cells.

Figure 3-27 shows comparisons on discharge rate performances for the reference cell and the experimental cell (2DM). Note that the electrochemical cells adopt a structure with Li foil as cathode and graphite as anode material, and the potential of graphite increases as discharge proceeds.

As a general tendency, the output specific capacity of a cell decreases as discharge rate increases. For larger rates, the decrease "rate" of output capacity also becomes more severe. Given relatively small rates (0.5 ~ 1 C), the differences between the reference group and the experimental group are not obvious. However, at larger rates (2 ~ 3 C), the capacity drops of the reference group and those of the experimental group show a huge gap, indicating the relevant advantage of the experimental group in terms of output capacity at high discharge rates.

3.4 Cycling performance

3.4.1 Modeling with SEI formation

At the negative electrode (using graphite as active material), there is a parasitic lithium/solvent reduction reaction, which decreases the amount of cyclable lithium and increases the SEI layer resistance in the battery cell. The kinetics of this reaction is described by the following equations [12]

$$i_{\text{loc,SEI}} = -(1+HK)\frac{i_{\text{loc,1C,ref}}J}{\exp\left(\frac{\alpha\eta_{\text{SEI}}F}{RT}\right)+\frac{q_{\text{SEI}}fJ}{i_{\text{loc,1C,ref}}}}$$

The formation of SEI layer in the negative electrode is described by:

$$\frac{\partial c_{\text{SEI}}}{\partial t} = -\frac{\upsilon_{\text{SEI}} i_{\text{loc,SEI}}}{nF}$$

$$q_{\text{SEI}} = \frac{F c_{\text{SEI}}}{A_{\upsilon}}$$

The thickness and resistance of SEI layer is described by:

$$\delta_{\text{film}} = \frac{c_{\text{SEI}} M_{\text{P}}}{A_{\upsilon}\rho_{\text{P}}} + \delta_{\text{film,0}}$$

The overpotential for the parasitic reaction is described by:

$$\Delta\phi_{\text{film}} = i_{\text{loc,SEI}} R_{\text{film}} = i_{\text{loc,SEI}} \frac{\delta_{\text{film}}}{\kappa}$$

$$\eta_{\text{SEI}} = \phi_{\text{s}} - \phi_{\text{l}} - \Delta\phi_{\text{film}} - E_{\text{eq,SEI}}$$

Table 3-4 List of variables/parameters. [15]

Symbol	Unit	Meaning
$i_{\mathrm{loc,SEI}}$	$\mathrm{A/m^2}$	Local current density
$i_{\mathrm{loc,1C,ref}}$	$\mathrm{A/m^2}$	Local current density with respect to 1C discharge
HK	1	Dimensionless graphite expansion factor function
J	1	Dimensionless exchanging current density for the parasitic reaction
f	1/s	Lumped nondimensional parameter
α	1	Transfer coefficient of the parasitic reaction
η_{SEI}	V	Overpotential for the parasitic reaction
c_{SEI}	$\mathrm{mol/m^3}$	Local SEI concentration
q_{SEI}	$\mathrm{C/m^2}$	Local accumulated charge due to SEI formation
υ_{SEI}	1	Stoichiometric coefficient of the SEI species in the parasitic reaction
A_{υ}	1/m	Surface area of the negative electrode
δ_{film}	m	Thickness of the SEI layer
$\delta_{\mathrm{film,0}}$	m	Initial thickness of the SEI layer
M_{P}	kg/mol	molar weight of the product of the parasitic reaction
ρ_{P}	$\mathrm{kg/m^3}$	density of the product of the parasitic reaction
R_{film}	$\Omega \cdot \mathrm{m^2}$	Resistance of the SEI layer
κ	S/m	Conductivity of the SEI layer

There are many factors affecting the value of current density of SEI reactions: transfer coefficient, frequency parameter, (non-dimensional) exchange current, and (non-dimensional) relative expansion factor. The former two are positively correlated to the current density of SEI reactions, while the latter two are negatively correlated to the current density.

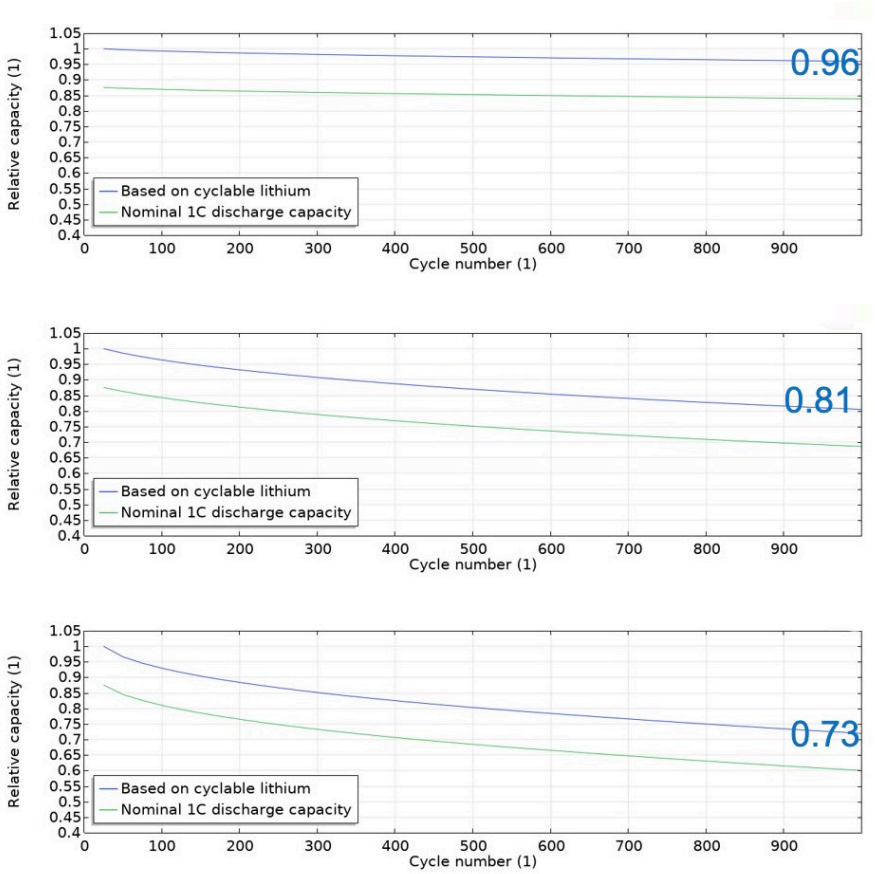

Figure 3-28 Illustration of the effect of expansion factor on cycling capacity. [16]

3.4.2 Results and Discussion

3.4.2.1 Static tests

A charge-discharge cycling test is simulated for both a reference group and an experimental group. Both groups are full electrochemical cells with graphite as anode material. The rates of charging and discharging are constant and identical.

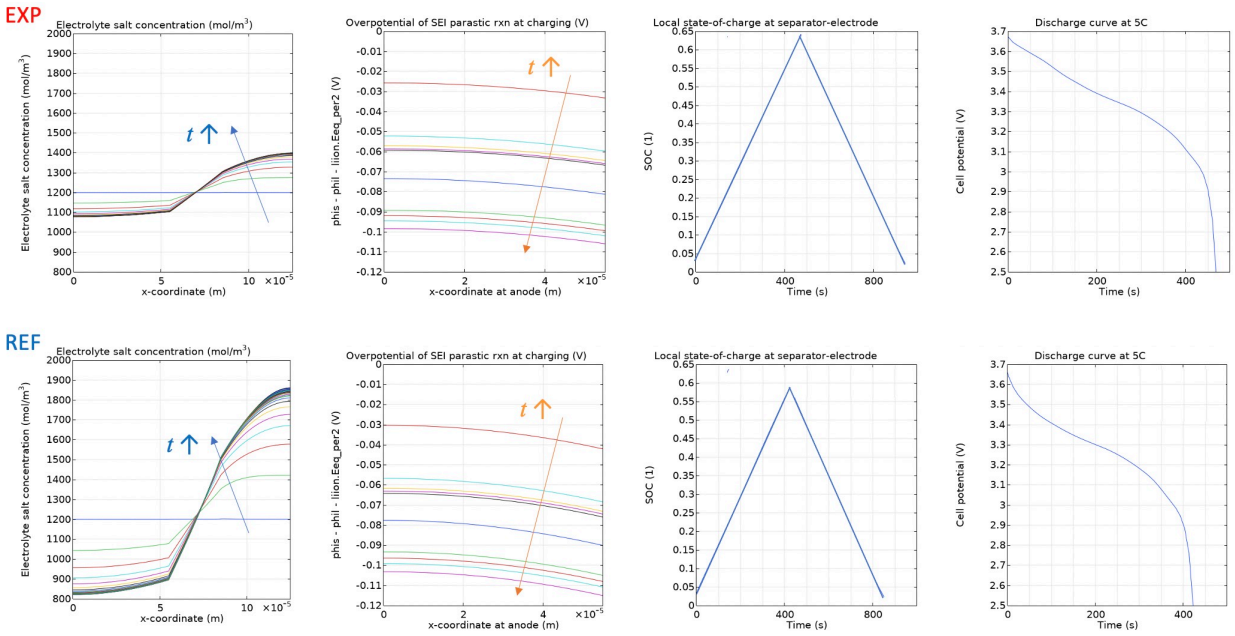

Figure 3-29 Temporal evolution for electrolyte salt concentration (left), overpotential of SEI parasitic reactions at charging (middle-left), material SOC at anode-separator interface (middle-right) and cell output voltage (right) for reference (up) and experimental (low) groups of NMC/graphite full-cells under charge/discharge cycling test.

Figure 3-29 compares the changes of several important properties during charge-discharge cycles for the reference group and the experimental group.

- the distribution of electrolyte in the solution affects the electrolyte potential,

- the electrolyte potential at the anode affects the magnitude of overpotential of SEI parasitic reaction, the duration of this reaction and the overall amount of lithium consumed by this reaction;

- the amount of lithium consumed by SEI parasitic reactions also reflects the amount of cyclable lithium, as they sum up to the overall amount of lithium in the cell, which should be conserved;

- the amount of cyclable lithium limits the range of SOC variation;

- the range of SOC variation affects the charge/discharge time.

Here is a brief explanation on how improving lithium ion transference number helps improve cycling performance of a full electrochemical cell with graphite anode:

With higher lithium transference number, the electrolyte concentration gradient across the cell during charging (not discharging) stages becomes smaller, resulting relatively slower increase of electrolyte potential and decrease of overpotential for SEI parasitic reactions, although the reaction time of the parasitic reaction should become longer (as the overall charging time is elongated due to smaller electrolyte concentration gradient), the overall lithium consumed by the parasitic reaction is still decreased compared to the reference group. In this way, more cyclable lithium is preserved, and the maximum SOC reached at the end of charging stages is higher, allowing relatively longer discharging time after cycles.

3.4.2.2 Dynamic stress tests

A dynamic stress test is conducted on the full electrochemical cell to explore its cycling performance under dynamic loading. The charging stage is the same to previous testing, while the discharging stage adopts a dynamic rate instead of a constant one.

Figure 3-30 shows the periodic dynamic loading applied to the cell (within a period of 360 seconds): Note that there are charging segments in this dynamic process. However, as the overall effect is discharging, the stage is still called as dynamic discharging stage.

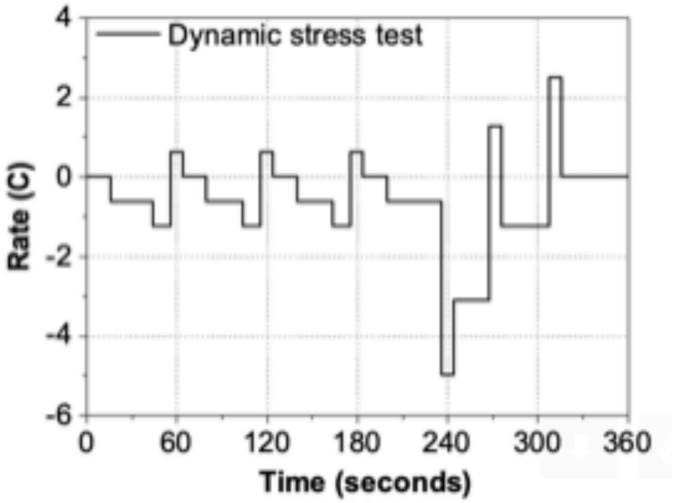

Figure 3-30 Periodic dynamic loading for dynamic stress tests. [17]

Figure 3-31 shows the temporal evolution of the output voltage for both cell groups during the first charging-discharging cycle:

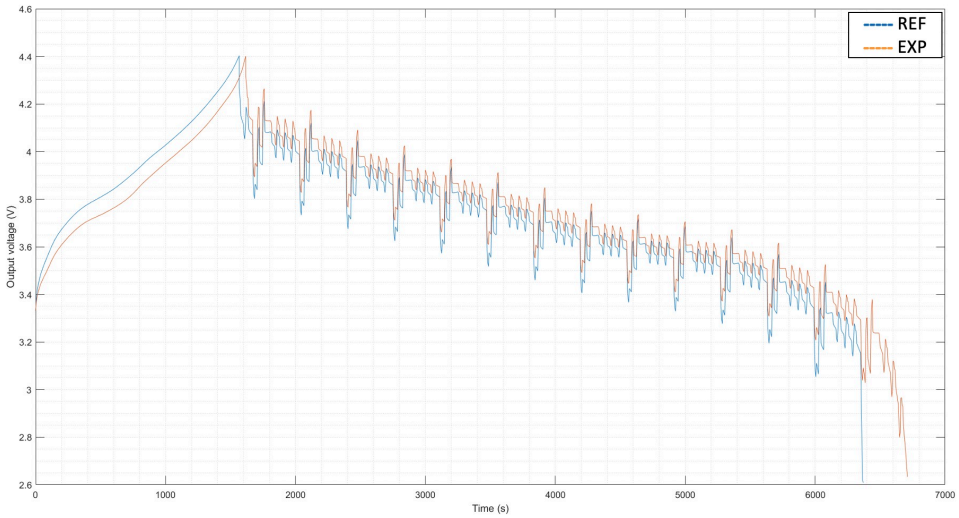

Figure 3-31 Temporal evolution of cell output voltage of reference (blue) and experimental (red) group during the first charge/discharge cycle of a dynamic stress test.

During the charging stage with a constant rate, the output voltages of both cells increase as time goes by. It is not surprised to see that, for the experimental group with higher lithium ion transference number, its voltage grows relatively slowly and it charging time is longer.

During the discharging stage with a dynamic rate, there is a general tendency that the output voltages of both cells decrease as time pass as the overall applied loading is negative current for discharging. It is similar to the case of discharging under constant rates: for the experimental group, its output voltage changes more slowly compared to the reference group, and thus takes a longer time to reach the cutoff voltage.

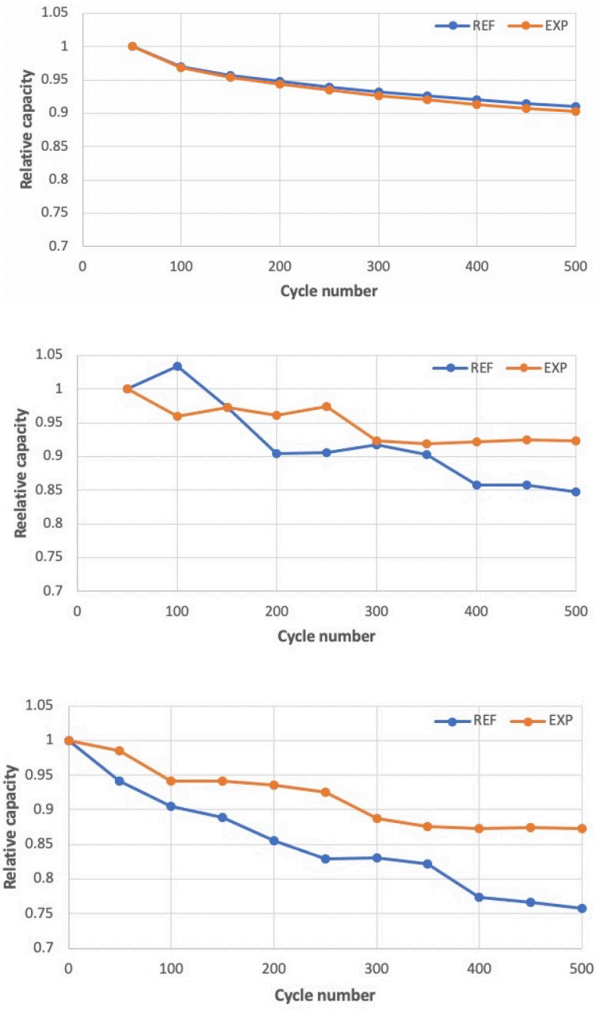

Figure 3-32 Variation of remaining capacities under DST based on cyclable lithium (blue), discharge time (green) and charge time (red) for experimental (left) and reference (right) group.

It is worth noting that at sudden changes of loading, there are overshooting (undershooting) followed by relatively smooth changes of output voltages. The magnitude of voltage

overshooting in the reference group is larger than that in the voltage group, indicating that it is relevant to the fast change of the ion distribution in the electrolyte solution of cells. When the output voltage is close to the cutoff threshold, it seems more “dangerous” for the reference group to reach the end of the current dynamic discharging stage, as a step change from charging loading (positive current) to discharging loading (negative current) brings a much huger undershoot of voltage. Once the voltage is below the cutoff threshold, the dynamic discharging stage is terminated, even though the supposed follow-up “more stable” change of voltage will be based on a value higher than the cut-off threshold.

Figure 3-32 shows relative capacity-cycle number plot for both reference and experimental group. There are different methods to estimate remaining capacity of a lithium ion battery: cyclable lithium-based and time-based.

It is interesting to see that there are not obvious differences in terms of capacity based on cyclable lithium between the reference group and the experimental group. To be honest, the reference group even maintains a higher capacity after 500 cycles, which is counter intuitive. A possible explanation is that, with higher lithium ion transference number, although smaller concentration gradient in electrolyte solution contributes to smaller overpotential of SEI parasitic reaction consuming cyclable lithium, the elongated time of this parasitic reaction as well as charging status of the anode (in both the constant-rate charging stage and the charging segments of the dynamic discharging stage) reverses its effect in reducing the consumption of cyclable lithium. On the other hand, it indicated that the temporal evolution of SOC variations of the graphite anode should be very similar for both groups.

However, there are some differences in terms of time-based capacities. Although SOC variations are similar, not all of this potential will be fully exploited given the polarization introduced by

many issues including the concentration gradient of electrolyte solution. Thanks to higher lithium transference number, the experimental group has a smaller electrolyte concentration gradient and thus is capable to enjoy more time before reaching cutover voltage (for charging) or cutoff voltage (for discharging). Thus, the experimental group has higher time-based capacities compared to the reference group.

Furthermore, there is more obvious difference between two group when the discharge capacity is the focus. The discharging stage is dynamic, while the charging stage is of constant rates. As discussed before, under dynamic loading, it is relatively easy for the reference group to reach the cutoff voltage since it exhibits large voltage undershoot possibly brought by large internal electrolyte concentration gradient. As a result, the discharging time is shortened compared to constant-rate cases.

From this simulation, it seems that for dynamic stress test, the reference group and the experimental group, shares similar pattern of cyclable lithium evolution, but have different time-based charge/discharge capacities. According to experimental results, there should *be* differences on the amount of cyclable lithium after cycles of tests for cells with various lithium transference numbers. Indeed, this is a limitation of the model and the associated simulation. More research is needed to help resolve this issue. Possible tracks might include:

- adjusting the modeling of SEI parasitic reactions;
- introducing side processes at the cathode side;
- introducing specific modeling for SEI processes under dynamic change of loading (which might be different from that under constant-rate charging).

3.5 Conclusion

In this section, the main focus is explaining rate/cycling performances of lithium-ion batteries (with metal-organic frameworks addition to electrolyte).

Firstly, to show how lithium ion transference number might be improved via rational design of MOF additions, heterogeneous geometries (pattern/density/location) to the separator/electrolytes are discussed.

Secondly, to explore how lithium ion transference number affects rate performances of lithium ion batteries, a mathematical model is studied for half-cells to indicate the links among lithium ion transference number, electrolyte salt concentration gradient, concentration polarization and utilizable capacity.

Thirdly, to explore how lithium ion transference number affects cycling performances of lithium ion batteries, mechanisms of solid-electrolyte interphase layer formation is introduced to the mathematical model for a full-cell, which discusses the overpotential of parasitic SEI reactions and loss of cyclable lithium under stable and dynamic cycling tests.

3.6 References

[1] Bai, P., Li, J., Brushett, F. R., & Bazant, M. Z. (2016). Transition of lithium growth mechanisms in liquid electrolytes. *Energy & Environmental Science*, *9*(10), 3221-3229.

[2] Sand, H. J. (1901). III. On the concentration at the electrodes in a solution, with special reference to the liberation of hydrogen by electrolysis of a mixture of copper sulphate and sulphuric acid. *The London, Edinburgh, and Dublin Philosophical Magazine and Journal of Science*, *1*(1), 45-79.

[3] Van Soestbergen, M., Biesheuvel, P. M., & Bazant, M. Z. (2010). Diffuse-charge effects on the transient response of electrochemical cells. *Physical Review E*, *81*(2), 021503.

[4] Zhang, Chen, et al. "Anion-Sorbent Composite Separators for High-Rate Lithium-Ion Batteries." *Advanced Materials* 31.21 (2019): 1808338.

[5] Shi, Wenyue, et al. "Electrolyte Membranes with Biomimetic Lithium-Ion Channels." *Nano Letters* 20.7 (2020): 5435-5442.

[6] Cai, Long, and Ralph E. White. "Mathematical Modeling of a Lithium Ion Battery." *Proceedings of the COMSOL Conference*. 2009.

[7] Torchio, Marcello, et al. "Lionsimba: a matlab framework based on a finite volume model suitable for li-ion battery design, simulation, and control." *Journal of The Electrochemical Society* 163.7 (2016): A1192-A1205.

[8] [Valøen, Lars Ole, and Jan N. Reimers. "Transport properties of LiPF6-based Li-ion battery electrolytes." *Journal of The Electrochemical Society* 152.5 (2005): A882-A891.

[9] Northrop, Paul WC, et al. "Coordinate transformation, orthogonal collocation, model reformulation and simulation of electrochemical-thermal behavior of lithium-ion battery stacks." *Journal of The Electrochemical Society* 158.12 (2011): A1461-A1477.

[10] Xu, Meng, and Xia Wang. "Electrode Thickness Correlated Parameters Estimation for a Li-Ion NMC Battery Electrochemical Model." *ECS Transactions* 77.11 (2017): 491-507.

[11] Moura, Scott J., et al. "Battery state estimation for a single particle model with electrolyte dynamics." *IEEE Transactions on Control Systems Technology* 25.2 (2016): 453-468.

[12] Ekström, Henrik, and Göran Lindbergh. "A model for predicting capacity fade due to SEI formation in a commercial graphite/LiFePO4 cell." *Journal of The Electrochemical Society* 162.6 (2015): A1003.

[13] Valøen, Lars Ole, and Jan N. Reimers. "Transport properties of LiPF6-based Li-ion battery electrolytes." *Journal of The Electrochemical Society* 152.5 (2005): A882.

[14] Ramesh, Srivatsan, K. Venkata Ratnam, and Balaji Krishnamurthy. "An empirical rate constant based model to study capacity fading in lithium ion batteries." *International Journal of Electrochemistry* 2015 (2015).

[15] 1D Lithium-Ion Battery Model for the Capacity Fade Tutorial. Comsol Application Gallery.https://www.comsol.com/model/download/631511/models.bfc.capacity_fade.pdf.

[16] Nie, Ping, et al. "Graphene caging silicon particles for high-performance lithium-ion batteries." *Small* 14.25 (2018): 1800635.

[17] DST profile. Dai, Haifeng, et al. "State of charge estimation for lithium-ion pouch batteries based on stress measurement." *Energy* 129 (2017): 16-27.

[18] 1D Isothermal Lithium-Ion Battery Tutorial. Comsol Application Gallery. https://www.comsol.com/model/1d-isothermal-lithium-ion-battery-686.

3.7 Appendix

3.7.1 Parameters for LFP/Li half-cell simulation

Table 3-5 List of arameters for LFP/Li half-cell rate performance sumuliation. [18]

Parameter	Value [Unit]	Meaning
i_1C	2.25[A/m^2]	1C discharge current
t_plus	0.38	Li-ion transference number (in non-separator region)
sigma_f	1	Scaling factor for electrolyte ionic conductivity (in non-separator region)
t_plus_SEP	0.38	Li-ion transference number (in separator region)
sigma_f_SEP	0.36	Scaling factor for electrolyte ionic conductivity (in separator region)
cl_0	1000[mol/m^3]	Initial electrolyte salt concentration
c_ref	1000[mol/m^3]	Reference electrolyte salt concentration for ionic conductivity interpolation
L_sep	40e-6[m]	Length of separator
L_pos	14e-6[m]	Length of positive electrode
T	298[K]	Temperature
rp_pos	8e-6[m]	Particle radius positive electrode
epsl_pos	0.63	Electrolyte phase volume fraction, positive electrode
epss_filler_pos	0.073	Conductive filler phase volume fraction, positive electrode
epss_pos	1-epsl_pos-epss_filler_pos	Electrode phase volume fraction, positive electrode
cs0_pos	3900[mol/m^3]	Initial concentration positive active electrode material
k_pos	4.8e-10[m/s]	Reaction rate coefficient positive electrode
brugg	3.3	Bruggeman coefficient

i_{1c} (i_1C) = $m_{loading} \cdot rate_{1C}$ = 1.5 mg/cm^2 * 150 mA/g = 2.25 A/m^2.

L_{pos} (L_pos) = $m_{loading}$ / ($\rho_{pos} \cdot \varepsilon_{pos}$) = 1.5 mg/cm^2 / (3600 kg/m^3 * 0.3) = 14 μm.

3.7.2 Parameters for Li/graphite half-cell simulation

Table 3-6 List of parameters for Li/graphite helf-cell rate performance sumlution. [18]

Symbol	Value	Meaning
i_1C	3[A/m^2]	1C discharge current
C	2	Discharge rate
t_plus	0.29	Li-ion transference number (in non-separator region)
sigma_f	1.5	Scaling factor for electrolyte ionic conductivity (in non-separator region)
t_plus_SEP	0.363	Li-ion transference number (in separator region)
sigma_f_SEP	1	Scaling factor for electrolyte ionic conductivity (in separator region)
L_neg	10e-6[m]	Length of negative electrode
L_sep	25e-6[m]	Length of separator
cl_0	1000[mol/m^3]	Initial electrolyte salt concentration
c_ref	1000[mol/m^3]	Reference electrolyte salt concentration
T	298[K]	Temperature
rp_neg	12.5e-6[m]	Particle radius negative electrode
epsl_neg	0.3	Electrolyte phase volume fraction, negative electrode
epss_filler_neg	0.14	Conductive filler phase volume fraction, negative electrode
epss_neg	1-epsl_pos-epss_filler_pos	solid phase volume fraction, negative electrode
cs0_neg	26000[mol/m^3]	Initial concentration negative active electrode material
k_neg	4.4e-10[m/s]	Reaction rate coefficient negative electrode
brugg	3.3	Bruggeman coefficient

3.7.3 Parameters for NMC/graphite full-cell sumlution

Table 3-7 List of parameters for NMC/graphite full-cell cycling performance sumlution. [15]

Symbol	Value	Meaning
epsl_pos	0.313	Electrolyte phase volume fraction positive electrode
epsl_neg	0.318	Electrolyte phase volume fraction negative electrode
epsl_sep	0.37	Electrolyte phase volume fraction separator
k_neg	2e-11[m/s]	Reaction rate coefficient negative electrode
k_pos	5e-10[m/s]	Reaction rate coefficient positive electrode
cl_0	1000[mol/m^3]	Initial electrolyte salt concentration
i_1C	29.93[A]	1C discharge current
L_neg	67e-6[m]	Length of negative electrode
L_sep	20e-6[m]	Length of separator
L_pos	60e-6[m]	Length of positive electrode
T	45[degC]	Cell temperature
E_max	4.4[V]	Maximum cell voltage
E_min	2.5[V]	Minimum cell voltage
kappa_film	5e-6[S/m]	SEI layer conductivity
M_sei	0.16[kg/mol]	Molar mass of product of side reaction
rho_sei	1.6e3[kg/m^3]	Density of product of side reaction
dfilm_0	1[nm]	Initial SEI layer thickness
alpha	0.67	Ageing parameter
J	8.40E-04	Ageing parameter
f	2.0e2[1/s]	Ageing parameter
H	6.7	Ageing parameter
i1C_loc	0.96943[A/m^2]	Ageing parameter
t_plus	0.3(ref)/0.8(exp)	Lithium ion transference number
Eeq_SEI	0.1[V]	Equilibrium potential of SEI formation reaction

Chapter 4 Prediction of Battery Cycle Life with LSTM RNN

4.1 Introduction

Lithium-ion batteries are widely used in electric devices because of their high energy densities, low cost and long lifetime [1]. As an important functionality of management systems of batteries, remaining useful life prediction gives probable failure time in advance for diagnostics and prognostics and aids manufacturing and operation of battery cells and systems. Meanwhile, it is also a challenging task since capacity degradation of batteries is a complex and nonlinear process influenced by internal physics and operating conditions.

There are many excellent research works for prediction of remaining useful life of batteries, where model-based methods and data-driven methods are two major branches. Model-based methods builds up mathematical models or semi-empirical models to capture the relations among internal processes, operation conditions and battery capacity degradation. First principles-based aging models are developed in [2][3][4], where relations between kinetics of SEI layer formation, reduction of electrolyte volume fraction and loss of cyclable lithium are explored. Particle filter [5] is a widely used fundamental algorithm combining with other theories and techniques for further improvement such as Dempster Shafer theory [6] and Akaike information criterion [7]. However, model-based methods are still restricted by lack of accurate aging models and particle degeneracy problem.

Data-driven methods, compared to model-based methods, do not require a mathematical or semi-empirical model but depend on experimental data of battery cycling. It is of essential significance to extract to relevant features from available data for life prediction. Severson and coworkers [8] explore a new feature about variations of discharge capacities as functions of cycles and voltages, which has a high correlation coefficient with cycle life. Combined with classical linear regression method, it gives promising results of cycle life prediction before obvious capacity degradation by only using data of first 100 cycles. The feature discussed in [8] only considers the difference between cycle 100 and cycle 10. It is interesting to see whether there will be any improvement on model prediction results (e.g, use even fewer cycles to achieve higher accuracy) by incorporating more cycles (cycle 20, cycle 30 and so on). In this way, the discharge capacities of various voltages under different cycles could be depicted as a sequence: a time step is a cycle, and the discharge capacities (of various voltages) for this cycle are features of this time step. Thus, the problem of interest is to use a sequence of battery discharge capacities (as functions of voltage and cycle) to predict the corresponding cycle life.

To learn from sequential data of capacity degradation, a suitable model plays an important role. recurrent neural networks (RNN) could be a probable option since there is an internal state capable to represent information of capacity degradation, which has been discussed by [9], [10]. Furthermore, long short-term memory (LSTM) RNN, with a solution to the problem of "gradient vanishing", is a powerful technique for learning long-term dependencies (how capacities degradation gets developed thorough cycles). Zhang and coworkers [11] present an application of LSTM RNN for battery remaining useful life predictions, which outperforms the results of

support vector machine (SVM) and traditional RNNs.

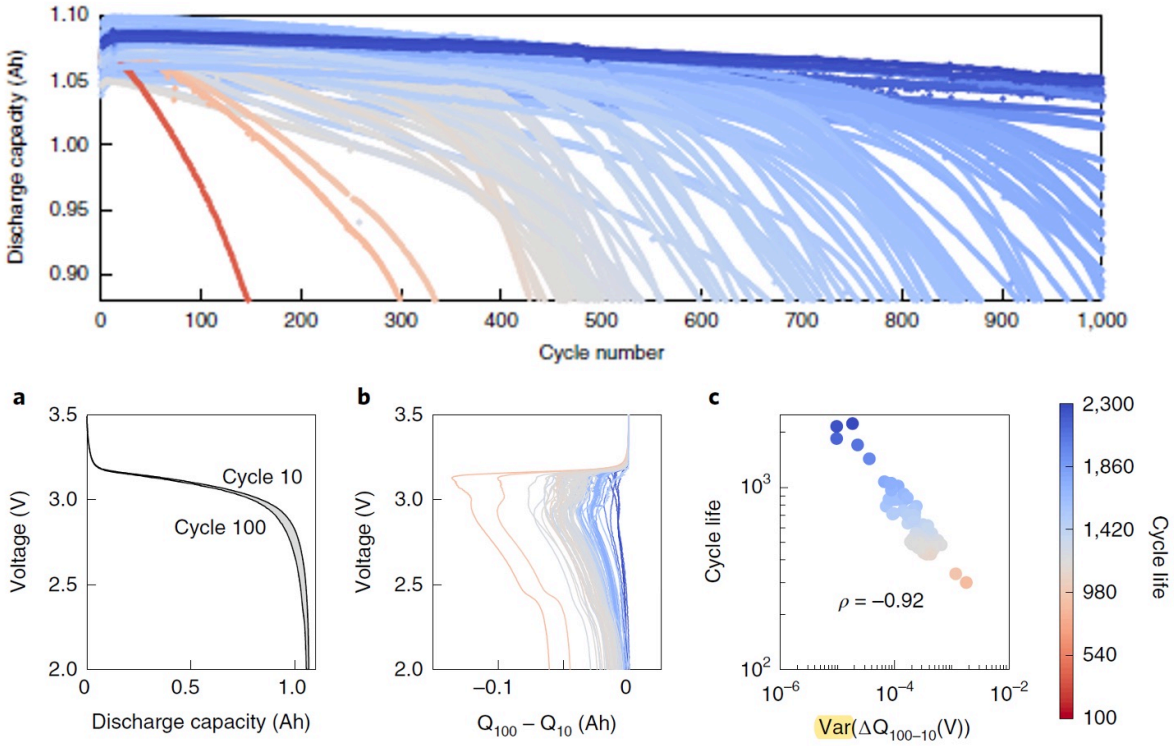

Figure 4-1 Visulation of the data set provided by literature. [8]

This work tries to combine some significant characteristics of these excellent research works by feeding the sequential data of discharge capacities at various voltages and cycles to a LSTM RNN model, which exhibits the promise of achieving following improvements:

capture latent information from discharge capacity vs voltage curves of early cycles;

predict cycle lives of acceptable accuracy with fewer required input cycles (less than 100);

reduce the need to manually extract task-specific features.

4.2 Battery Data Set

The data set used in this work is provided by [8]. As the largest public battery dataset, it contains 124 identical commercial lithium iron phosphate/graphite cells (manufactured by A123 Systems) cycled under 72 different fast-charging and identical discharging conditions. The split of training set and test set is consistent with the original paper: 41 sample in the training set, 43 samples in the primary test set, and 40 samples in the secondary test set.

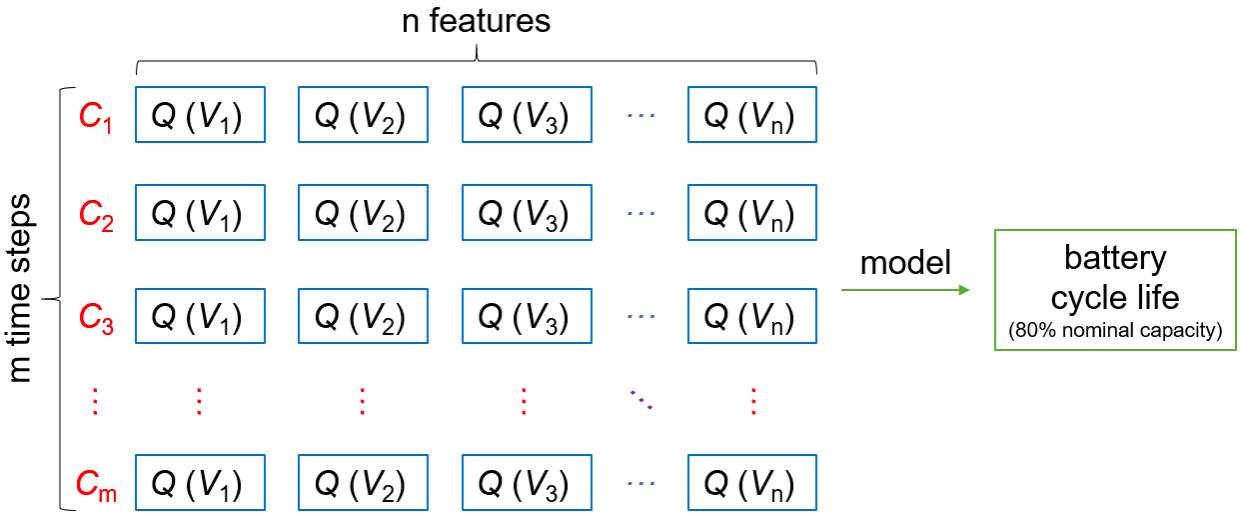

Figure 4-2 LSTM RNN model input (left) and output (right): For input, Q is discharge capacity, which is a function of voltage V and cycle number C. A series of Cs (monotonic increasing, not necessarily consecutive) are viewed as time steps, and Qs (of Vs) given a specific C are viewed as features of this time step. For output, under cycling of assigned charging and discharging, the cycle at which a battery cell remains 80% of its nominal capacity is defined as its cycle life for the given cycling condition.

As Figure 4-2 shows, the input of the LSTM RNN model is a sequence of discharge capacities at different voltages. For each sample of battery cell, data from a starting cycle (e.g., cycle 11) to a terminal cycle (e.g., cycle 100) are used as time steps. In each time step, discharge capacities at voltages within a range of [3.5 V, 2.0 V] (with 0.01 V as step size) are chosen as features.

At discharge stages of various cycles, the discharge capacity under a specific voltage also varies due to capacity degradation. Intuitively, as Figure 4-3 shows, within a range of cycles, battery cells showing longer cycle lives have more “uniform” discharge capacity vs voltage curves while those with shorter cycle lives have more “dispersed” discharge capacity vs voltage curves. In addition to normalizing data of discharge capacities for the ease of neural network learning, in order to make the differences of discharge capacities among difference cycles more obvious, we use the discharge capacities at cycle 10 as base values and subtract them from those at other cycles.)

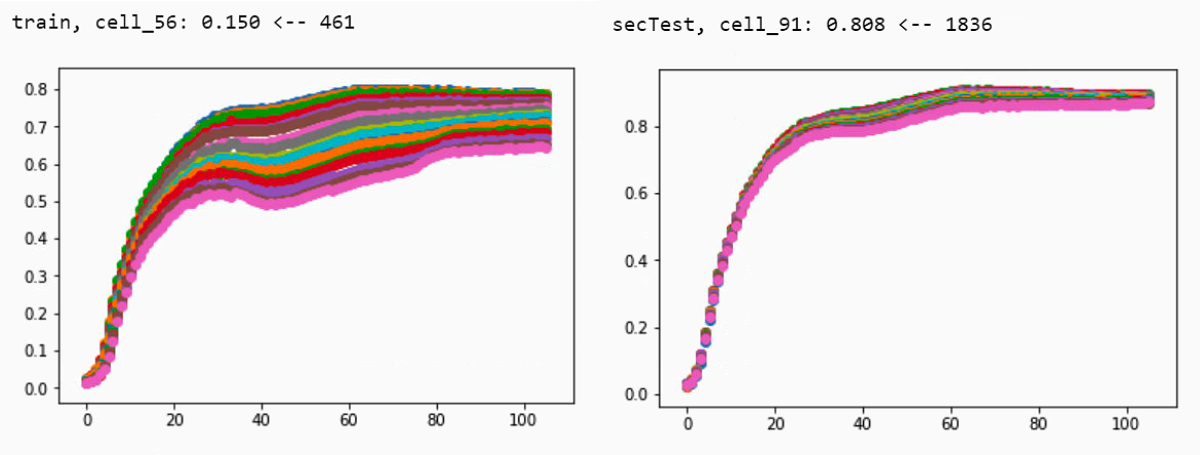

(a) A low-lifetime cell (b) A high-lifetime cell

Figure 4-3 Examples of discharge capacity vs voltage curves for battery cells with different lifetimes: A curve stands for a cycle (the higher, the earlier cycle); x-axis is normalized voltage, y-axis is normalized discharge capacity.

4.3 LSTM RNN MODEL

4.3.1 Architecture

As Figure 4-4 shows, in our LSTM RNN model built by Keras with TensorFlow backend [12], an input layer is fed into an CuDNNLSTM layer with 64 - 128 neurons, then fed into another

CuDNNLSTM layer with 128 - 256 neurons, next fed into a densely-connected layer of 32 neurons with a “relu” (Rectified Linear Unit) activation function, and finally fed into a densely-connected layer of 1 neuron with a linear activation function (since the task here is prediction instead of classification). It is worth mentioning that CuDNNLSTM layers are employed here instead of normal LSTM layers for faster model training, prediction and prediction [13].

A general issue in machine learning application is to avoid overfitting. Since there are small data set and large number of model parameters, it is easy for the model to become overfitted. Dropout technique [14] is employed to prevent overfitting, and the retained probability of hidden layers of was set to 0.2.

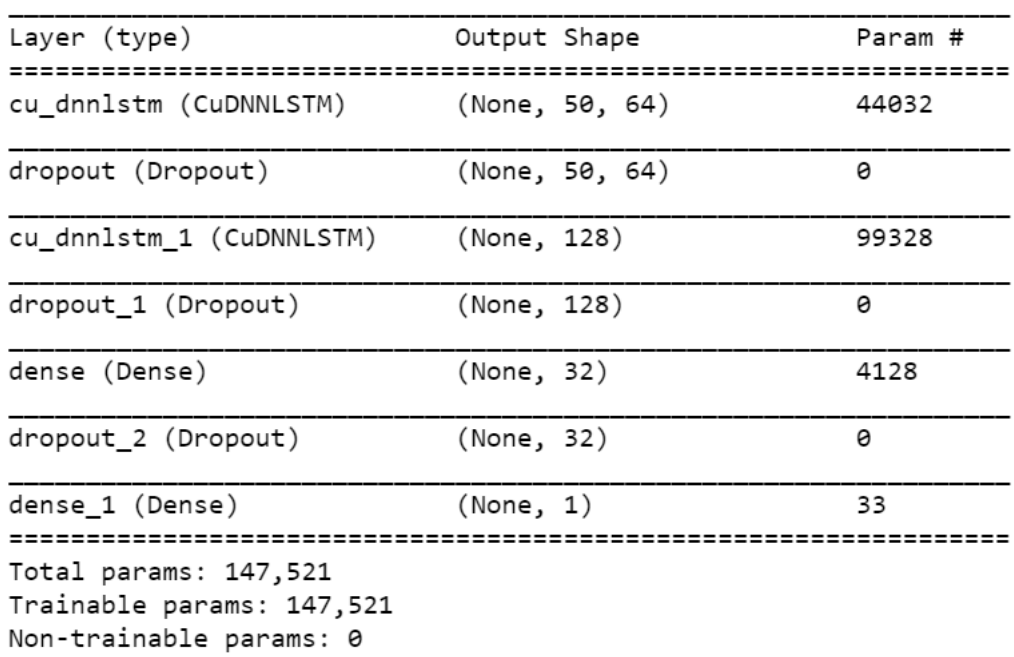

Layer (type)	Output Shape	Param #
cu_dnnlstm (CuDNNLSTM)	(None, 50, 64)	44032
dropout (Dropout)	(None, 50, 64)	0
cu_dnnlstm_1 (CuDNNLSTM)	(None, 128)	99328
dropout_1 (Dropout)	(None, 128)	0
dense (Dense)	(None, 32)	4128
dropout_2 (Dropout)	(None, 32)	0
dense_1 (Dense)	(None, 1)	33

Total params: 147,521
Trainable params: 147,521
Non-trainable params: 0

Figure 4-4 LSTM RNN model summary: CuDNNLSTM layer (default tanh, w/ Dropout) -> CuDNNLSTM layer (default tanh, w/ Dropout) -> Dense layer (relu, w/ Dropout) -> Dense layer (linear).

4.3.2 Training

In our neural network model, the loss function is mean squared error (MSE). It is defined as

$$\text{MSE} = \frac{1}{N}\sum_{i=1}^{N}\left(\hat{S}_i - S_i\right)^2$$

where N is the example number of test set, S is the set of predicted cycles lives and $\hat{S}$ is the set of actual cycle lives.

Table 4-1 Set up of the LSTM RNN model for battery RUL prediction.

Item	Choice
ML Framework	Keras w/ TensorFlow backend
Hardware	HP Z420 Intel Xeon E-1650 v2 Nvidia GTX 1080 Ti
Loss function	Mean square error
Optimizer	Adam optimizer
Method	Mini-batch gradient descent

Adam optimizer [15] is used to train the model (learning rate is 1e-3, and decay rate is 1e-6). For gradient descent, the batch size is set to 128, and number of epochs is 400 - 1000.

The training was implemented on a HP Z420 workstation with an Intel Xeon E5-1650 v2 processor (up to 3.50 GHz) and a graphic card of Nvidia GTX 1080 Ti (11 GB memory).

In order to balance low-lifetime samples with high-lifetime ones and prevent overfitting of the training set, a strategy of data augmentation is applied to generate “fake” samples by“shifting”

genuine samples. For example, given data of battery cell, a genuine sample takes cycle 11 - cycle 60 as model input and its cycle life (denoted as cl) as model output, and then a fake sample can use cycle 16 - cycle 65 as model input and (cl - 5) as model output, which is obtained "shifts" the genuine sample by 5 cycles. The step of "shifting" is 3 cycles, if applied.

4.4 Results and Discussion

Figure 4-5, Table 4-2 and Table 4-3 evaluates our model (taking inputs with different terminal cycles from 40 to 100) on 2 kinds of evaluation metrics, compared with classical models developed in [8]. The applied evaluation metrics consists of root mean squared error (RMSE) and mean absolute percentage error (MAPE) for our LSTM RNN model. RMSE is defined as the square root of MSE, and MAPE is defined as

$$\text{MAPE} = \frac{1}{N}\sum_{i=1}^{N}\left(\hat{S}_i - S_i\right)^2/\hat{S}_i \times 100\%$$

where N, S and $\hat{S}$ have same meanings to previous formula. For referenced models, "variance" model utilizes only 1 feature having high correlation coefficient with cycle lives and achieves good prediction results. The feature is

$$\log \text{var}\left(Q_{100}(V) - Q_{10}(V)\right)$$

where Q is discharge capacity, V is voltage, 100 and 10 are cycle numbers. Moreover, "discharge" model adds more features extracted from current density and voltage during discharging stages in the first 100 cycles, and it presents even better ability to predict cycle lives. In our LSTM RNN model, for both test sets and both evaluation metrics, there seems to be a general tendency that the errors become relatively flat after cycle 60 - 80. For the primary test set, our model shows good results (between 2referenced models) by using data of first 60 cycles

(terminal cycle is 60), and it gets similar results to “discharge” model when using data of first 80 cycles. It seems that, for the primary data set, our model is capable to give good predicted cycle lives using data of fewer than 100 cycles.

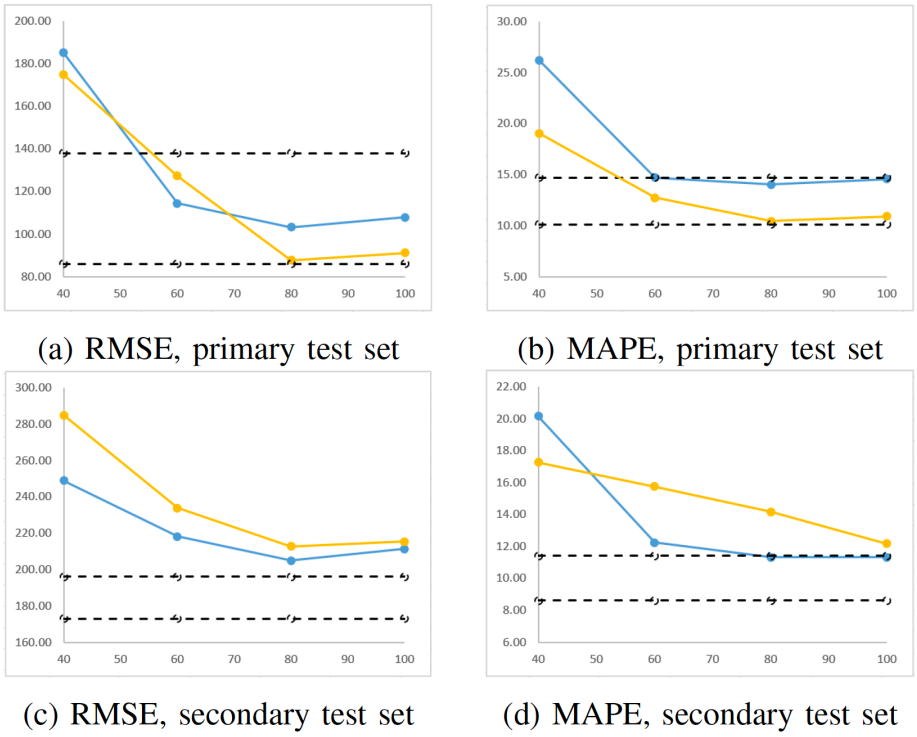

(a) RMSE, primary test set (b) MAPE, primary test set

(c) RMSE, secondary test set (d) MAPE, secondary test set

Figure 4-5 Model results: x-axis is terminal cycle, RMSE is root mean square error, and MAPE is mean average percentage error; black dotted lines are referenced results from [8]: upper line stands for “variance” model, and lower line stands for “discharge” model; colored lines are results of our LSTM RNN model (dots are average values over 10 parallel experiments): yellow line takes non-augmented data for training, blue line takes augmented data.

For the secondary test set, however, things become interesting. Using same training set consisting of 41 samples, our model does not give satisfactory prediction results, which are even not close to those of “variance” model. A possible explanation is that, the secondary test set contains some “latent” features quite different from the training set. Due to the small amount of available samples and large number of trainable parameters in our model, the trained parameters overfits the training set and cannot generate well to the secondary test set.

Table 4-2 Model Result Comparison on RMSE (Cycle).

Model	Train	PriTest	SecTest
“Variance” (@ 100) [8]	103	138 (138)	196
“Discharge” (@ 100) [8]	76	91 (86)	173
LSTM RNN (@ 60)	51.1 ±0.1	127.3 ±1.4	223.8 ±0.5
LSTM RNN (@ 80)	47.9 ±2.1	87.7 ±6.0	212.8 ±2.2
LSTM RNN (@ 100)	42.3 ±1.0	91.2 ±3.8	215.3 ±3.5
LSTM RNN (@ 60, aug)	63.4 ±5.0	114.3 ±3.5	218.2 ±4.0
LSTM RNN (@ 80, aug)	63.3 ±2.8	103.1 ±2.7	204.9 ±2.7
LSTM RNN (@ 100, aug)	56.3 ±6.3	107.9 ±5.3	211.3 ±5.6

Note: “@” is followed by terminal cycle of input data, and ”aug” means augmented data are used during model training. Same note to the other table.

Table 4-3 Model Result Comparison on MAPE (%).

Model	Train	PriTest	SecTest
“Variance” (@ 100) [8]	14.1	14.7 (13.2)	11.4
“Discharge” (@ 100) [8]	9.8	13.0 (10.1)	8.6
LSTM RNN (@ 60)	6.2 ±0.1	12.7 ±0.4	15.8 ±0.1
LSTM RNN (@ 80)	6.2 ±0.3	10.4 ±0.4	14.2 ±0.7
LSTM RNN (@ 100)	5.6 ±0.2	10.9 ±0.7	12.2 ±0.2
LSTM RNN (@ 60, aug)	7.9 ±1.0	14.7 ±0.9	12.2 ±0.2
LSTM RNN (@ 80, aug)	8.7 ±0.6	14.0 ±0.5	11.3 ±0.6
LSTM RNN (@ 100, aug)	7.1 ±1.0	14.6 ±1.2	11.3 ±0.4

A preliminary trial of data augmentation is applied to reduce the phenomena of overfitting. Since there is less high-lifetime samples (having cycle life greater than 775, which is just a causal trial) in the training set than in the secondary test set, the trick to augment data (mentioned in Section III) is applied to high-lifetime samples but not low-lifetime ones. Our model trained with augmented training set shows improved prediction results on the secondary test set: it approaches “variance” model by only using the first 80 cycles of data, but there is still a gap to “discharge”

model. Unexpectedly, our model trained with augmented data gives worse results on the primary data set, which may results from the “enlarged” dissimilarity between the training set and the primary test set after augmenting the training set.

Admittedly, our model has far more complex structure and consumes more computation resources for training than classical models presented by [8]. However, it has the potential to learn from complex sequential data of battery cycling so that it might require fewer number of input cycles to make predictions of similar accuracy compared to classical models, where those “saved” cycles could mean a lot in industrial research and development. Moreover, unlike “discharge” model, out model does not intake additional “task-specific” features such as skewness and kurtosis of cycling data of discharge capacity vs voltage curves. Although our model currently cannot give as excellent results as classical models on the secondary test set, with more available data and advanced overfitting-preventing techniques, its ability to generalize can be further improved.

4.5 Conclusion

In this work, an LSTM RNN model is developed for early prediction of battery cycle lives. The input data is cycle sequences of capacities within discharge voltage windows, which is inspired by the feature highly correlated with cycle lives presented by [8]. By taking first 60 - 80 cycles of data, our model achieves satisfactory RMSE and MAPE on the primary test set. With data augmentation during training, the model also shows acceptable prediction results on the secondary test set by using fewer cycles of data. In general, this work explores a LSTM RNN model taking a new input form of sequential data, which is promising in reducing the required number of early cycles for predicting cycle lives.

4.6 References

[1] Schmuch, Richard, et al. ”Performance and cost of materials for lithiumbased rechargeable automotive batteries.” Nature Energy 3.4 (2018): 267.

[2] Ramadass, P., et al. ”Development of first principles capacity fade model for Li-ion cells.” Journal of the Electrochemical Society 151.2 (2004): A196-A203.

[3] Ning, Gang, Ralph E. White, and Branko N. Popov. ”A generalized cycle life model of rechargeable Li-ion batteries.” Electrochimica acta 51.10 (2006): 2012-2022.

[4] Ekstrm, Henrik, and Gran Lindbergh. ”A model for predicting capacity fade due to SEI formation in a commercial graphite/LiFePO4 cell.” Journal of The Electrochemical Society 162.6 (2015): A1003-A1007.

[5] Su, Xiaohong, et al. ”Interacting multiple model particle filter for prognostics of lithium-ion batteries.” Microelectronics Reliability 70 (2017): 59-69.

[6] He, Wei, et al. ”Prognostics of lithium-ion batteries based on Dempster- Shafer theory and the Bayesian Monte Carlo method.” Journal of Power Sources 196.23 (2011): 10314-10321.

[7] Xing, Yinjiao, et al. ”An ensemble model for predicting the remaining useful performance of lithium-ion batteries.” Microelectronics Reliability 53.6 (2013): 811-820.

[8] Severson, Kristen A., et al. “Data-driven prediction of battery cycle life before capacity degradation.” Nature Energy 4.5 (2019): 383.

[9] Liu, Jie, et al. An adaptive recurrent neural network for remaining useful life prediction of lithium-ion batteries. NATIONAL AERONAUTICS AND SPACE ADMINISTRATION MOFFETT FIELD CA AMES RESEARCH CENTER, 2010.

[10] Rezvani, Mohammad, Seungchul Lee, and Jay Lee. A comparative analysis of techniques for electric vehicle battery prognostics and health management (PHM). No. 2011-01-2247. SAE Technical Paper, 2011.

[11] Zhang, Yongzhi, et al. “Long short-term memory recurrent neural network for remaining useful life prediction of lithium-ion batteries.” IEEE Transactions on Vehicular Technology 67.7 (2018): 5695-5705.

[12] Brownlee, Jason. Deep learning with python: Develop deep learning models on theano and tensorflow using keras. Machine Learning Mastery, 2016.

[13] Braun, Stefan. “LSTM benchmarks for deep learning frameworks.” arXiv preprint arXiv:1806.01818 (2018).

[14] Srivastava, Nitish, et al. “Dropout: a simple way to prevent neural networks from overfitting.” The journal of machine learning research 15.1 (2014): 1929-1958.

[15] Kingma, D. P., and J. L. Ba. “Adam: A method for stochastic optimization. arXiv 2014.” arXiv preprint arXiv:1412.6980 (2014).

Chapter 5 Summary and Perspectives

In this dissertation, design and simulation for addressing bottlenecking performance challenges of popular and promising energy storage systems. The following topics are included:

- dynamic response under load change of proton exchange membrane fuel cells,
- high rate discharging behavior of lithium-ion batteries,
- remaining useful lives under cycling of lithium-ion batteries.

Alternatively, the following table provides more information:

Table 5-1 Brief summary of dissertation contents.

	PEM fuel cell	Li-ion battery
have done	1. established an equivalent circuit with proper units to simulate dynamic response of the cell voltage under load change; 2. discussed how the competition between gas demand and supply in GDL affects the dynamic response of the cell voltage, and how the addition of WO_3 mitigates the overshoot indirectly; 3. included the effect of WO_3 addition at the anode.	1. built up an equation model incorporating internal charge, species and mass transport processes of the cell according to the porous electrode theory; 2. included the effect of MOF addition at the electrolyte; 3. incorporated irreversible processes in the cell for proper cycling simulation; 4. analyzed cycling data with data-driven methods for RUL early prediction.
to be done	1. exploring the influence of water transport on dynamic response of the cell; 2. developing a mathematical model of the whole cell including mass, charge and heat transport.	1. considering gas generation and recombination at the electrode (and possible new reactions with MOF); 2. developing a higher-dimensional non-isothermal model (and gas effect in temperature variation) and solving it with finite volume method.

In a nutshell, this dissertation applies models for proton exchange membrane fuel cell and lithium-ion battery with different techniques to simulate internal processes occurring in a component/the entire system, and explains the reason why adopted design strategies mitigate certain types of performance bottlenecks or utilizes big data to learning from time series and make predictions on remaining useful lives. With these works, some inspirations might be provided for understanding methods to enhance transient and/or high-rate performances of electrochemical energy storage systems.

However, it is worth mentioning that simulations are just simulations, which might be orthogonal to laboratory experiments and only unveil a little part of the truth of the objects being researched. This limitation comes from many factors, such as system error of model establishment and insufficient data volume. Thus, it is necessary to validate output of simulations with real experimental data and theoretical calculations.

From another perspective, various models are explored including equivalent circuits, mathematical models (based on transport phenomena and electrochemistry) and artificial neural networks. All of them have specific application scenarios and specific requirements. It is important to explore and select an appropriate model approach according to problem statements and available data sets. Also, it might be interesting to integrate multiple simulation approaches to achieve “the best of both worlds”. For example, mathematical models might provide insights to extract important features (relevant to internal processes of electrochemical energy storage systems) as input for machine learning approaches for improvement in training cost and prediction accuracy.